AD-A193 497 LOW TEMPERATURE FILM GROWTH OF THE OXIDES OF ZINC ALUMINUM AND VANADIUM (..(U) WISCONSIN UNIV MILWAUKEE LAB OF SURFACE STUDIES C R AITA FEB 88 ARO-21334.19-MS 1/2

UNCLASSIFIED DAAG29-84-K-0126 F/G 7/4 NL

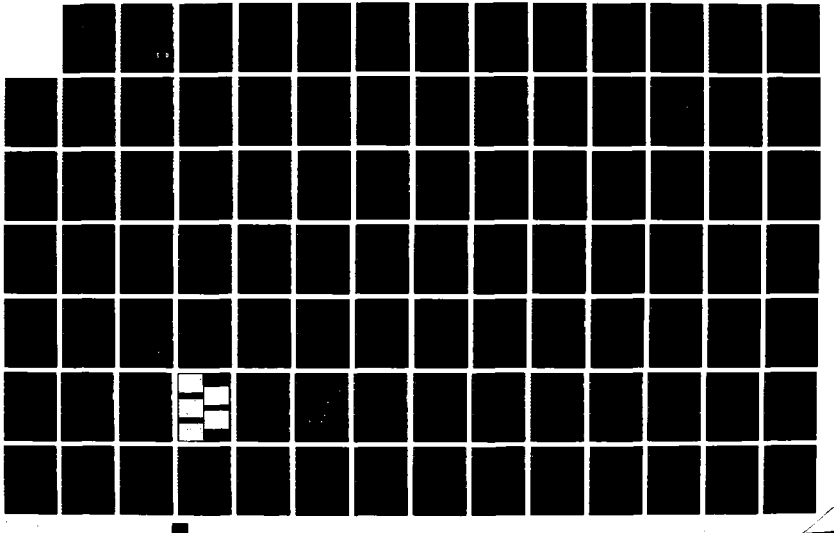

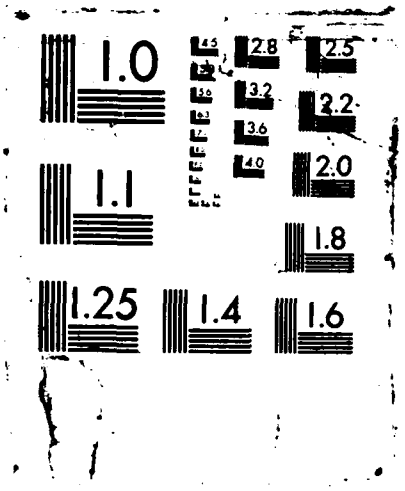
1.0
1.1
1.25
1.4
1.6
1.8
2.0
2.2
2.5
2.8
3.2
3.6
4.0
4.5

(2)

LOW TEMPERATURE FILM GROWTH OF THE OXIDES OF ZINC, ALUMINUM, AND VANADIUM (AND RELATED SYSTEMS, OXIDES OF GOLD AND GERMANIUM, NITRIDES OF ALUMINUM AND TUNGSTEN) BY REACTIVE SPUTTER DEPOSITION

FINAL REPORT

CAROLYN RUBIN AITA

DAAG29-84-K-0126

FEBRUARY 1988

MATERIALS DEPARTMENT AND THE LABORATORY FOR SURFACE STUDIES
UNIVERSITY OF WISCONSIN-MILWAUKEE
P.O. BOX 784
MILWAUKEE, WISCONSIN 53201

UNCLASSIFIED

SECURITY CLASSIFICATION OF THIS PAGE (When Data Entered)

REPORT DOCUMENTATION PAGE		READ INSTRUCTIONS BEFORE COMPLETING FORM
1. REPORT NUMBER: ARO 21334.19-MS	2. GOVT ACCESSION NO.: N/A	3. RECIPIENT'S CATALOG NUMBER: N/A
4. TITLE (and Subtitle): Low temperature film growth of the oxides of zinc, aluminum, and vanadium (and related systems, oxides of gold and germanium, nitrides of aluminum and tungsten).		5. TYPE OF REPORT & PERIOD COVERED: Final Report: 7/1/84-12/31/87
		6. PERFORMING ORG. REPORT NUMBER
7. AUTHOR(s): Prof. Carolyn Rubin Aita		8. CONTRACT OR GRANT NUMBER(s): DAAG29-84-K-0126
9. PERFORMING ORGANIZATION NAME AND ADDRESS: Materials Department&Laboratory for Surface Studies, University of Wisconsin-Milwaukee / P.O. Box 784, Milwaukee, Wisconsin 53201		10. PROGRAM ELEMENT, PROJECT, TASK AREA & WORK UNIT NUMBERS
11. CONTROLLING OFFICE NAME AND ADDRESS: U. S. Army Research Office, Post Office Box 12211, Research Triangle Park, NC 27709		12. REPORT DATE: February 1988 13. NUMBER OF PAGES: 140 pages
14. MONITORING AGENCY NAME & ADDRESS(if different from Controlling Office)		15. SECURITY CLASS. (of this report): Unclassified 15a. DECLASSIFICATION/DOWNGRADING SCHEDULE

16. DISTRIBUTION STATEMENT (of this Report)

Approved for public release; distribution unlimited.

17. DISTRIBUTION STATEMENT (of the abstract entered in Block 20, if different from Report)

NA

18. SUPPLEMENTARY NOTES

The view, opinions, and/or findings contained in this report are those of the author(s) and should not be construed as an official Department of the Army position, policy, or decision, unless so designated by other documentation.

19. KEY WORDS (Continue on reverse side if necessary and identify by block number)

sputter deposition, glow discharges, glow discharge diagnostics, optical emission, mass spectrometry, aluminum oxide, vanadium pentoxide, gold oxide, tungsten nitride, aluminum nitride, germanium dioxide,

20. Abstract:

The research involved investigation of process parameter-growth environment-film property relationships for various binary oxide and nitride films grown on unheated substrates by reactive sputter deposition using an elemental target. In situ optical emission spectroscopy and glow discharge mass spectrometry were used to determine gas phase species in the plasma volume. A battery of techniques were used to characterize (post-deposition) film crystallography, chemistry, microstructure, electrical resistivity, and optical behavior. We sought to identify the active gas phase species responsible for a particular type of film growth and the location of the controlling reaction(s), that is, at the target surface, in the plasma volume, at the substrate.

DD FORM 1 JAN 73 1473 EDITION OF 1 NOV 65 IS OBSOLETE

UNCLASSIFIED

SECURITY CLASSIFICATION OF THIS PAGE (When Data Entered)

FOREWORD

The general theme of the research supported under US ARO Grant No. DAAG29-84-K-0126 was the investigation of process parameter-growth environment-film property relationships for sputter deposited binary oxide and nitride films grown by reactive sputter deposition on unheated substrates.

The original proposal was entitled "Low temperature film growth of the oxides of zinc, aluminum , and vanadium by reactive sputter deposition",and was submitted for funding consideration in September 1983. The work which was ultimately funded and begun in July 1984 was broader in scope in terms of discharge characterization and diagnostics than originally proposed. The work actually carried out was even broader in terms of the investigation of four new materials systems, Al-N, W-N, Au-O, and Ge-O, in addition to the original three, Al-O, Zn-O, and V-O. Nitrides, as well as oxides, were included. The precise reasons why a particular materials system was chosen to add are given in the Progess Reports, written at six-month intervals throughout the duration of the research.

In accordance with the suggested format, the Final Report is structured as follows. Section I contains a statement of the problem addressed. Section II contains a description of the research highlights. For experimental details or for information about materials systems not covered in Sec. II, the reader is urged to consult the publications supported under this grant, which are listed in Sec. III. Several of these publications are contained in the Appendices. The participating scientific personnel and degrees awarded are listed in Sec. IV.

The principal investigator acknowledges her contract monitor, Dr. R.R. Reeber, for many helpful suggestions in terms of the direction of the research. She acknowledges her colleagues: Prof. M.G. Lagally for making available the Auger-ESCA Laboratory at UW-Madison; Prof. B.E. Brown for use of the x-ray diffraction facilities at the Center for Great Lakes Studies and in the Department of Geological Sciences, UW-Milwaukee; Prof. M.E. Marhic for use of the infrared spectroscopy facility in the Technological Institute, Northwestern University; Prof. R.A. Weeks for electron spin resonance measurements at Vanderbilt University and for aid with understanding defects in tetrahedrally bonded bulk oxide glasses; and Prof. G.S. Baker, Materials Department, UW-Milwaukee, for fruitful discussions, proof-reading of manuscripts, and his generous support and encouragement.

Carolyn Rubin Aita

Milwaukee, Wisconsin

February 1988

TABLE OF CONTENTS

I. STATEMENT OF THE PROBLEM STUDIED

The research we undertook was the investigation of process parmeter-growth environment-film property relationships for various binary oxide and nitride films grown near room temperature by reactive sputter deposition using an elemental target.

The thrust of the experimental program was three-fold and included:

1) Film deposition

2) In situ sputtering discharge characterization

3) Film characterization

We combined the results from these areas to determine process parameter-growth environment-film property relationships for a particular materials system. We then sought to compare behavior in different materials systems in order to determine general trends.

In the course of the study, we worked with seven materials systems: Al-O, V-O, Zn-O, Al-N, W-N, Au-O, and Ge-O. These systems were chosen for two reasons. 1) They contain technologically interesting materials. Understanding how to reproducibly synthesize these materials is of practical importance. 2) Each system was considered to be representative of a class and was used as a model to extend and generalize processing-growth environment-property relationships.

The chemistry, crystallography, and microstructure of a metal[1] oxide or nitride film grown by reactive sputter deposition depends upon the relative flux of metal, metal oxide/nitride, and and oxygen/nitrogen species which arrive at the substrate, are

adsorbed, and are ultimately incorporated into stable nuclei which coalesce to form a continuous film. In terms of events that occur in the glow discharge or at the electrodes, the factors which control film chemistry/crystallography/microstructure are:

1) Processes occurring at the target which affect the balance between the rate of removal of metal atoms and the rate of formation and removal of metal oxide/nitride molecules.

2) Plasma volume processes: collisional and radiative processes which lead to either the oxidation/nitridation of sputtered metal atoms, or to the dissociation of sputtered metal oxide/nitride molecules.

3) Processes at the substrate which affect the adsorption, surface diffusion, bulk diffusion, and desorption of metal, oxygen/nitrogen, and metal oxide/nitride species.

We sought to identify the active gas phase species responsible for a particular type of film growth and the location of the controlling reaction(s) in which the species is engaged (that is, at the target, in the plasma volume, at the substrate).

Two process parameters were studied extensively: nominal gas composition and cathode voltage. Changes in these parameters affected large changes in discharge chemistry, discharge power, and deposition rate, as will be discussed in relation to specific materials systems in Sec. II.

Neutral and ionic species in the plasma volume were studied using optical emission spectroscopy[2] and glow discharge mass spectrometry (Appendix A). A battery of analytical techniques

were used to characterize film crystallography, chemistry, microstructure, optical behavior, and electrical resistivity.

We next present a summary of the most important results. Experimental details relating to the synthesis of a particular material or to a particular plasma reaction are contained in the Appendices.

II. SUMMARY OF MOST IMPORTANT RESULTS

1. Phase transitions in the Al-N system: Construction of a ternary gas composition diagram (N_2-Ne-Ar).

An Al target was sputtered using N_2-bearing discharges containing Ne, Ar, and Ne+Ar mixtures. Films were deposited on on Supersil fused SiO_2 and <111>-cut Si substrates. Their properties were studied, post-deposition, using x-ray diffraction, Rutherford backscattering spectroscopy, resistivity measurements, and transmission spectrophotometry. From the results, a three-gas composition diagram was constructed onto which Al-N phases were mapped (Appendix B).

AlN has a wurtzite-type hexagonal close-packed lattice structure. We found that phase transitions in the sputter deposited Al-N system were as follows: <111>-texture Al[3] -> <111>-texture Al(N) -> microcrystalline AlN cermet -> microcrystalline AlN -> multiorientation AlN_x -> single basal orientation AlN. For the same nominal discharge N_2 content, the use of Ne rather than Ar as the rare gas component of the discharge supressed the formation of the Al, AlN -cermet, and microcrystalline AlN_x structures, and enlarged the region of rare gas/reactive gas composition over which basal orientation AlN was formed.

In situ optical emission from N_2^+ and Al^o species in the plasma was used to relate the transition from Al->AlN films to an increase in the relative flux of N_2^+/Al^o in the plasma volume, as detailed in Appendix B. The increase in N_2^+ in the plasma volume in N_2-Ne discharges compared to N_2-Ar or pure N_2 discharges (p.B16, Fig. 2) results from the Penning ionization

ground state N_2^o by a Ne atom in a low-lying metastable energy state, Ne^m. Penning ionization of N_2^o by Ar^m is energetically impossible.[4] Al cannot chemisorb N_2^o,[5] whereas N_2^+ dissociates upon impact with a surface (target or growth interface), releasing N species which react with Al.[6]

AlN is formed at and sputtered from the target surface in coincidence with its formation at the substrate. This can be seen by a comparison of growth rate and Al^o optical emission in the N_2-Ar system.[7] Figure 1, p.B15 shows that the transition from Al -> AlN films was completed when the discharge contained 20% N_2. At that point, the deposition rate had dropped to 45% of its value in pure Ar but the Al^o optical emission intensity had dropped much lower, to 17%. Clearly, Al-bearing species in addition to atomic Al were being sputtered from the target surface.

2. Corrosion behavior of Al, AlN$_{x<1}$-cermet, and AlN-coated mild steel.

We utilized the ternary gas composition diagram described in Sec. II.1 to deposit a set of Al-N films with a wide range of chemistry, crystallography, and microstructure on 1008 steel substrates. The films ranged from large-grained, porous, metallic Al to two cermet structures to fine-grained, non-porous AlN. Corrosion rates of the steel+coating composite were measured in an O_2-free 0.2M KCl electrolyte under conditions of cathodic polarization. Details of the experimental procedure, materials characterization, and the results of the corrosion experiment are given in Appendix C.

To summarize here, the results show that a 1μm-thick AlN coating lowers the corrosion rate of steel by over an order of magnitude. The corrosion rate increases with increasing Al content in the coating, and ultimately exceeds that of both bare steel and bulk Al.

Two models are presented to explain the results. A non-porous, non-reactive electrode model is used to describe the corrosion behavior of AlN-coated steel, with the overall corrosion reaction:

$$Fe^{o} + 2H^{+} \rightarrow Fe^{+2} + H_2^{o} \qquad (1)$$

At the other extreme, a porous, reactive electrode model is used to describe the behavior of Al-coated steel. In addition to the

Eq. (1), four other corrosion reactions are proposed to occur, based on a galvanic reaction between Al and Fe. These reactions are described on pp. C7-8.

3. X-ray photoelectron loss spectroscopy of two aluminas and aluminum nitride.

X-ray photoelectron loss spectroscopy (XPLS) is an application of x-ray photoelectron spectroscopy (XPS) which involves determining the energy separation, ΔE, between a core photoelectron peak and its principal loss peak.

Three materials were studied here, described in Appendix D:
1) Basal orientation AlN sputter deposited on <111>-cut Si.
2) Amorphous (a-) Al_2O_3 sputter deposited on <111>-cut Si.
3) Bulk single crystal basal orientation α-Al_2O_3.
It is not possible to distinguish these materials on the basis of the chemical (Siegbahn) shift in the binding energy of the Al2p and Al2s electrons alone, or to even precisely measure the binding energy, since charging shifts are on the order of several eV.

XPLS results show that these materials can be distinguished by differences in ΔE, independent of sample charging (p.D6, Figs.5&6). Furthermore, a comparison of ΔE for the two aluminas as a function of depth from the surface (p.D6, Figs.3&4) shows that both forms have the same value of ΔE at the surface, but a-Al_2O_3 has a lower value than α-Al_2O_3 below the surface. It has been proposed[8] that ΔE increases with increasing ionicity of the same cation. An etching study[9] on a-Al_2O_3 showed that Al at the surface was in 6-fold coordination with O, as in α-Al_2O_3, and that its coordination number decreased on the interior of the film, decreasing its ionicity.

There is agreement between ΔE obtained by XPLS and

calculations based on a free electron gas model assuming a plasmon origin of the loss spectra (p.D7 Table II). However, more theoretical work must be done to show that this agreement is not coincidental.

4. Optical behavior of sputter deposited vanadium pentoxide: Relationship to vanadyl oxygen vacancies.

Vanadium pentoxide has a sheet-like structure, consisting of alternating layers of V+O atoms and O atoms alone (vanadyl O layer), as discussed in Appendices E and F. In a preliminary study,[10] we showed that V_2O_5 can be grown by reactive sputter deposition on unheated <111>-cut Si, <0001>-cut α-Al_2O_3, Supersil fused SiO_2, and laboratory glass slides. Without exception, the films grew with layers aligned parallel to the substrate plane, that is, with the b-axis or <010> crystallographic direction perpendicular to the substrate.

The local environment around a V atom in a perfect V_2O_5 lattice is shown in Fig. 1a, p.F1, where b_o is the ideal interlayer spacing. Films were deposited in which deviation from the ideal, measured by $\Delta b=(b-b_o)/b_o$, ranged from -0.23% to +1.14% (Appendix G). Based on growth rate data and optical emission from excited atomic V in the discharge,[10] we concluded that an oxide layer had formed at the target surface once the O_2 content of the discharge reached a critical value, after which the target no longer acted as a getter for O_2. The value of b was related to the state of target oxidation. Films in which $b<b_o$ were deposited from a target whose surface was not fully oxidized. After target surface oxidation was complete, the interplanar layer spacing rose rapidly to $b>b_o$. Films in which $b=b_o$ were produced in a discharge which contained the critical O_2 content for target surface oxidation. A deviation of b from b_o was associated with defects in the vanadyl O layer.

For the case of $b<b_o$, the defects were vanadyl O vacancies, as shown in Fig. 1c, p.F1. It was shown in a theoretical study[11] that in the case of an isolated defect, excess charge is localized near the V site adjacent to the vanadyl O vacancy, giving the ion a V^{+4} nature. Yet, the structural order of the material remains unchanged. At the other extreme, it was observed in bulk reduced V_2O_5, that when enough vanadyl O atoms were missing, the two adjacent V+O layers collapse and a V_6O_{13} stacking fault is formed.[12]

In this study, we observed a change in V-O coordination as a change in position and shape of the fundamental optical aborption edge. For less extreme cases of $b<b_o$, the position of the fundamental optical absorption edge was consistent with that reported for single crystal V_2O_5, as discussed in Appendix E. However, the absorption edge had a low energy tail which became more pronounced as Δb became more negative, i.e. when more vanadyl O vacancies were present. For small negative Δb, the tail consisted of two discrete absorption bands related to states within the energy band gap which were not continuous with either valence or conduction band edge. Electronic transitions possibly responsible for these discrete bands are 1) $3d^1 \rightarrow 3d^1$ transitions of the V^{+4} ion in the complex containing the vanadyl O vacancy,[13] or 2) transitions between a $3d^1$ level of the V^{+4} ion and an empty V 3d state at the bottom of the V_2O_5 conduction band which has been locally perturbed to lower energy.[11,14]

5. Phase transitions in W-nitride films sputter deposited using $Ar-N_2$, $Ne-N_2$, and N_2 discharges.

A W target was sputtered in N_2-bearing discharges containing Ar or Ne. Films were deposited on <111>-cut Si and laboratory glass slides. Their properties were studied using x-ray diffraction and resistivity measurements. Details of the experimental procedure are given in Appendix H. The phases present in the films were determined by consideration of crystallography and electrical behavior.

Published information about the W-N system is limited. Neither the compositional range of the equilibrium phases, fcc W_2N and hexagonal WN, nor the metastable phases which are formed are well understood. Much of the thin film work on sputter deposited W-nitrides was carried out by Nicolet and co-workers (Appendix H, Refs. 1-3) who were interested in barrier layer behavior. In the present study, we are interested determining the effect of carrier gas type on nitridation.

The results show that films deposited in pure rare gas discharges are two-phase, consisting of bcc α-W, the equilibrium phase, and fcc β-W, a metastable phase. The following sequence of phase transitions were observed as N_2 was added to an Ar discharge: low resistivity microcrystalline structure, a-W(N) -> W_2N -> high resistivity microcrystalline structure, $X.W-nitride$. The use of Ne instead of Ar accelerated the formation of the higher N content phases and supressed the formation of a-W(N). The major diffraction peaks are shown in

Fig. 3, p.H15. Crystallographic parameters are given in Table II, p.H11.

Neither fcc β-W(N) (containing $\geq$18-<33 atom% N) nor fcc W_2N was found in the films. The two microcrystalline structures, a-W(N) and X.W-nitride, have also been observed by Affolter et al,[15] but cannot be associated with the equilibrium phases of W-nitride. A series of six hexagonal layered W-nitride phases ranging in composition from W_2N to WN_2 were reported over twenty-five years ago.[16] These phases, prepared by nitriding thin W films in NH_3, are interesting for the following reasons. 1) They represent a change in lattice parameter perpendicular to the basal plane (c-axis) with almost no change in lattice parameter within the basal plane (a-axis). 2) Their bonding spans a metallic -> covalent transition. 3) They are non-Häag phases spanning a wide range of stoichiometry and cannot be predicted from conventional principles for determining the crystal structure of interstitial compounds.[17] 4) They are similar in structure to the layered equilibrium phases of transition-metal borides.[18] Because of their large c/a ratio, the diffraction pattern of these phases consist of closely-spaced, perhaps unresolvable, peaks in the vicinity of 2θ=35-40°, corresponding to reflections from $\{10\bar{1}.l\}$ planes with l=0-3. This type of pattern is observed in the diffraction scans of both a-W(N) and X.W-nitride.

6. Sputter deposition of Au-oxide.

The effect of oxygen on the growth of Au films has been of continuing interest for over twenty years (Appendix I, Refs. 1-4), with an eye towards understanding improved film adhesion when O_2 is added to an Ar sputtering discharge. It was suggested that an Au-oxide formed at the substrate which aided bonding, and that the oxidation process was assisted by active oxygen species in the discharge, in particular O_2^+.

Previous studies of Ar-O_2 and Ne-O_2 discharges are included in Appendix J. In Ar-O_2, it was found that the number of O_2^+ ions was proportional to the nominal O_2 content of the discharge. This was not the case with Ne-O_2, where the Penning process at low discharge O_2 content created a large population of O_2^+, detected with both optical emission spectroscopy and glow discharge mass spectrometry. The effect of a large O_2^+ ion population at low discharge O_2 content was studied with respect to sputter deposited Pt-oxide.[19-21]

Here, we investigated the crystallography (Table I) and resistivity (Fig. 1) of films deposited from a Au target in Ar-O_2 and Ne-O_2 discharges.[22] The crystallographic changes which occurred as O_2 was initially added to the rare gas discharge are similar in the Au-O and Pt-O systems. Evidence of Au-O bond formation was obtained from the chemical shift of Au *4f* electron binding energy. Three oxidation states, Au^o, Au^{+1}, and Au^{+3}, were identified.[23] The ratio of the number of Au species in +1 and +3 states to Au metal is shown in Fig. 2 as a function

of discharge O_2 content. A comparison of Figs. 1 and 2 clearly shows the relationship between Au^{+3} species and a large increase in resistivity. As expected, the use of Ne as the rare gas component of the discharge, rather than Ar, enhances the oxidation of Au at low discharge O_2 content.

Table I: Crystallographic parameters for Au and Au-oxide films films grown on <111>-cut Si and glass slides.

Gas Content	Au plane Si/glass	Rel. Int. Si/Glass	2θ, deg. Si/Glass (a	FWHM, deg. Si/Glass (b
Ar	111/111	100/100	38.3/38.2	0.4/0.5
Ar-5%O_2	111/111	100/100	38.2/38.2	0.3/0.3
	200/200	4/6	44.4/44.3	0.7/0.6
	220/220	3/5	64.6/64.5	0.6/0.9
	311/311	3/5	77.5/77.2	0.8/0.9
Ar-10%O_2	111/111	100/100	38.3/38.2	0.3/0.4
	200/200	14/20	44.4/44.3	0.7/0.7
	220/220	14/15	64.6/64.6	0.6/0.5
	311/311	7/12	77.6/77/5	0.9/0.6
Ar-25%O_2	111/111	100/100	38.2/38.2	0.7/0.7
	200/200	21/20	44.4/44.3	1.1/1.0
	220/220	20/17	64.7/64.6	0.8/1.0
	311/311	14/12	77.6/77.6	1.0/1.2
Ar-50%O_2 (c	111/111	100/100	38.2/38.2	2.0/2.1
Ar-75%O_2 (c	111/111	100/100	38.2/38.3	1.7/1.7
100%O_2 (c	111/111	100/100	38.3/38.2	1.4/1.6
Ne	111/111	100/100	38.3/38.1	0.5/0.5
Ne-5%O_2	111/111	100/100	38.2/38.1	0.8/0.8
	200/200	12/11	44.4 44.0	1.1/1.4
	220/220	11/12	64.5/64.3	1.3/1.3
	311/ -	7/ -	77.3/ -	1.2/ -
Ne-10%O_2	111/111	100/100	38.3/38.1	0.7/0.8
	200/200	12/16	44.2/44.0	1.2/1.5
	220/220	11/14	64.5/64.3	1.2/1.3
	311/311	7/7	77.2/77.2	1.3/1.6
Ne-25%O_2 (c	111/ -	100/ -	38.4/ -	2.4/ -
Ne-50%O_2 (c	111/ -	100/ -	38.3/ -	2.1/ -
Ne-75%O_2 (c	111/111	100/100	38.4/38.3	1.7/1.1

a) 2θ for bulk Au reflections: (111), 38.2°; (200), 44.5°; (220), 64.7°; (311), 77.7° for Cu kα radiation (λ=1.5418Å).
b) Broadening due to instrument effects=0.2°.
c) Very weak peaks, metallic Au is only one component of this cermet material. A dash (-) indicates no diffraction peak.

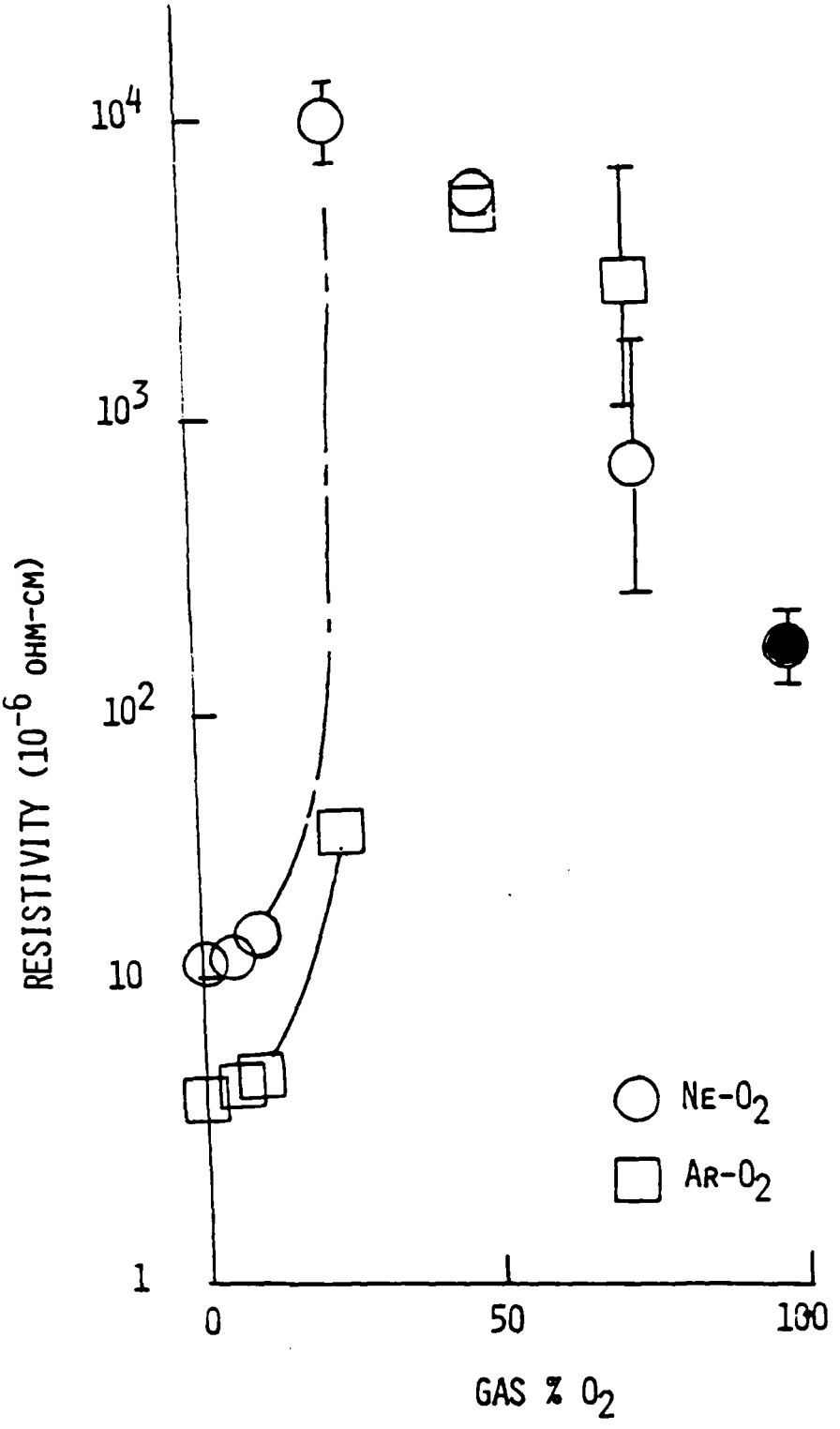

FIG. II.6.1: THE RESISTIVITY OF AU AND AU-OXIDE FILMS GROWN ON <111>- CUT SI BY SPUTTERING A AU TARGET IN NE-O_2 AND AR-O_2 DISCHARGES (REF. 22).

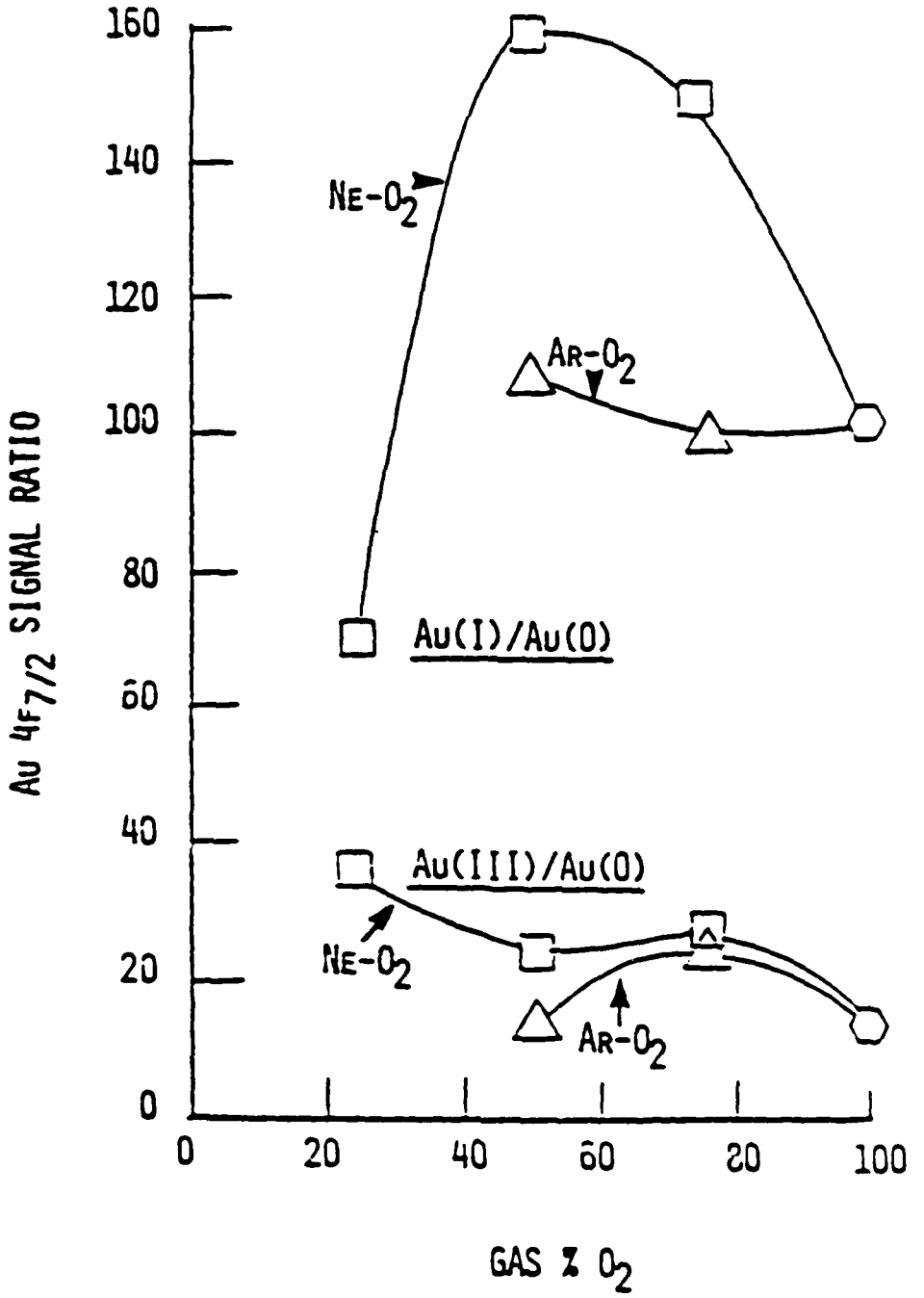

FIG. II.6.2: THE RATIO OF THE NUMBER OF Au SPECIES IN +1 AND +3 OXIDATION STATES TO Au METAL AS A FUNCTION OF DISCHARGE O_2 CONTENT (REF. 23).

7. Process-induced disorder in sputter deposited glassy germania.

Glassy germania (nominally GeO_2) was studied here as a model system for a tetrahedral-bonded thin film oxide glass. The results of a study of the effect of Ar-O_2 discharge composition on the near ultraviolet-visible-near infrared optical behavior of GeO_x ($1.85 \leq x \leq 2.30$) is included in Appendix K. In the case of films which are nominally germania ($GeO_{2.0-2.3}$), there was an increase in disorder in Ge-O_4 bonding as Ar was introduced into the discharge without a change in overall chemistry. The disorder is manifest by[24] 1) a decrease in the optical energy band gap, 2) an increase in optical absorption in the visible spectrum, 3) an increase in the frequency of the infrared-active Ge-O-Ge stretch mode, indicating a lower film density, and 4) an increase in the width of the infrared-active Ge-O-Ge stretch band, indicating a larger spread in bond strength from tetrahedron to tetrahedron. The mechanism by which Ar disrupts Ge-O_4 bonding, as well as the nature of the defects created, will be a subject of future research.

References

1. Although Ge is not a metal, it is included in the following discussion.
2. J.E. Greene, J. Vac. Sci. Technol. 15, 1718 (1978).
3. Crystallographic orientation of the film is given throughout this report relative to the substrate plane.
4. F.M. Penning, Z. Phys. 46, 225 (1925); 57, 723 (1929).
5. G. Ehrlich, Proc. Eighth International Summer Institute in Surface Science (R. Vanselow, editor, CRC Press, Boca Raton, Florida, 1987).
6. H.F. Winters, D.E. Horne, and E.E. Donaldson, J. Chem. Phys. 41, 2733 (1966); H.F. Winters and Eric Kay, J. Appl. Phys. 38, 3928 (1967); H.F. Winters, J. Chem. Phys. 44, 1472 (1969): H.F. Winters and D.E. Horne, Surf. Sci. 24, 587 (1971).
7. C.R. Aita and C.J. Gawlak, J. Vac. Sci. Technol. A 1, 403 (1983); J. R. Siettmann, MS Thesis, University of Wisconsin-Milwaukee, August 1987.
8. T.L. Barr, in Practical Surface Analysis (D. Briggs and M.P. Seah, editors, Wiley, New York, 1983).
9. R.G. Frieser, J. Electrochem. Soc. 113, 357 (1966).
10. S.D. Hansen and C.R. Aita, J. Vac. Sci. Technol. A 3, 660 (1985).
11. P. Clauws and J. Vennik, Phys. Stat. Sol. B 66, 553 (1974).
12. E. Gillis and E. Boesman, Phys. Stat. Sol. 14 337 (1966).
13. C.J. Ballhausen and H.B. Gray, Inorg. Chem 1, 111 (1962).

14. W. Lambrecht, B. Djafari-Rouhani, and J. Vennik, J. Phys. C 19, 369 (1986).

15. K. Affolter, H. Kattelus, and M.-A. Nicolet, Proc. Mater. Res. Soc. 47, 167 (1985).

16. V.I. Khitrova and Z.G. Pinsker, Sov. Phys.-Crystal 6 712 (1962).

17. see for example: L.E. Toth, Transition Metal Carbides and Nitrides, Academic, New York, 1971); H.J. Goldschmidt, Interstitial Alloys (Plenum, London, 1967).

18. A.F. Wells, Structural Inorganic Chemistry (Oxford, London, 1950) p. 593-596.

19. C.R. Aita and N.C. Tran, J. Appl. Phys. 54, 6051 (1983).

20. C.R. Aita and N.C. Tran, J. Appl. Phys. 56, 958 ((1984).

21. C.R. Aita, J. Appl. Phys. 58, 3169 (1985).

22. A.M. Klumb, MS Thesis, University of Wisconsin-Milwaukee, December 1987.

23. C.R. Aita, J.R. Siettmann, K.J. Huber, A.M. Klumb, and N.C. Tran, 17th Annual Symp. Appl. Vac. Sci. and Technol. Clearwater Beach, Florida, 1988.

24. C.R. Aita, 34th Natl. Symp. Amer. Vac. Soc., Anaheim, California, 1987.

III. REFEREED PUBLICATIONS SUPPORTED BY ARO

1. "Low temperature reactive sputter deposition of vanadium oxide." S.D. Hansen and C.R. Aita, J. Vac. Sci. Technol. A 3, 660 (1985).

2. "Glow discharge mass spectrometry for sputtering discharge diagnostics." Carolyn Rubin Aita, J. Vac. Sci. Technol. A 3, 625 (1985) Review.

3. "Optical behavior of sputter deposited aluminum nitride." C.J.G.Kubiak, C.R. Aita, F.S. Hickernell, and S.J. Joseph, Proc. Mater. Res. Soc. 47, 75 (1985).

4. "Characterization of sputter deposited Al-nitride and Al-oxide by x-ray photoelectron loss spectroscopy." Charlene J.G. Kubiak, Carolyn Rubin Aita, Ngoc C. Tran, and Tery L. Barr, Proc. Mater. Res. Soc. 60, 385 (1986).

5. "Optical behavior of sputter deposited vanadium pentoxide." Carolyn Rubin Aita, Ying-Li Liu, Mei Lee Kao, and Steven D. Hansen, J. Appl. Phys. 60, 749 (1986).

6. "$(ArO)^+$ and $(ArO_2)^+$ ions in rf sputter deposition discharges." Carolyn Rubin Aita and Robert J. Lad, J. Appl. Phys. 60, 837 (1986).

7. "Low temperature oxidation of non-stoichiometric sputter deposited vanadium pentoxide." Carolyn Rubin Aita and Mei Lee Kao, J. Vac. Sci. Technol. A 5, 2714 (1987).

8. "AuO^+ and AuO_2^+ gaseous ions formed during the sputter deposition of Au films in Ar-O_2 discharges." Carolyn Rubin Aita, J. Appl. Phys. 61, 5182 (1987).

9. "O^+, O_2^+, O_3^+, and O_4^+ ions in Ar-O_2 sputtering discharges: comments on 'Oxidation mechanism in rf CO_2 plasma,' Vacuum 36, 85 (1986)." Carolyn Rubin Aita and Michel E. Marhic, Vacuum 38, 37 (1988).

10. "Interlayer spacing of sputter deposited vanadium pentoxide films." Carolyn Rubin Aita, Chee-Kin Kwok, and Mei Lee Kao, Proc. Mater. Res. Soc. 82, 435 (1987).

11. "Near ultraviolet-visible-near infrared optical behavior of sputter deposited GeO_x ($1.85 \leq x \leq 2.30$)." Carolyn Rubin Aita, Michel E. Marhic, and Curt N. Sayers, Proc. 2nd International Conference on the Effects of Modes of Formation on the Structure of Glass, in press (1988).

12. "Resistivity changes and phase evolution in W-N films sputter deposited in Ne-N_2 and Ar-N_2 discharges." Karl J. Huber and Carolyn Rubin Aita, J. Vac. Sci. Technol. A 6, in press (1988).

13. "Al, Al-N, and AlN-coated steel corrosion behavior in O_2-free KCl solutions." W.S. Tait, C.O. Huber, B.C. Begnoche, J.R. Siettmann, and C.R. Aita, J. Vac. Sci. Technol. A 6, in press (1988).

14. "Growth of Al and Al-nitride films in N_2-Ne and N_2-(Ne+Ar) discharges." James R. Siettmann and Carolyn Rubin Aita, J. Vac. Sci. Technol. A 6, in press (1988).

INVITED AND CONTRIBUTED PAPERS AT NATIONAL SYMPOSIA

1. "X-ray photoelectron loss spectroscopy of wide energy band gap aluminum compounds." Carolyn R. Aita, Charlene J. Kubiak, Ngoc C. Tran, and Tery L. Barr, First International Conference on the Structure of Surfaces, Berkeley, California, 1984.

2. "Glow discharge mass spectrometry for sputtering discharge diagnostics." C.R. Aita, 31st National Symposium of the American Vacuum Society, Reno, Nevada, 1984. (Invited)

3. "Growth of vanadium oxide by reactive sputter deposition." S.D. Hansen and C.R. Aita, 31st National Symposium of the American Vacuum Society, Reno, Nevada, 1984.

4. "Reactive sputter deposition of aluminum nitride and oxide films." C.R. Aita, 14th Annual Symposium on Applied Vacuum Science and Technology, AVS and DOE co-sponsored, Clearwater, Florida, 1985. (Invited)

5. "Optical behavior of sputter deposited aluminum nitride: correlation with chemistry." C.J.G. Kubiak and C.R. Aita, 1985 Spring Meeting of the Materials Research Society, San Francisco, California, 1985.

6. "Formation of argon-oxygen ions in rf sputtering discharges." Carolyn Rubin Aita, 32nd National Symposium of the American Vacuum Society, Houston, Texas, 1985.

7. "Characterization of sputter deposited Al-nitride and Al-oxide by x-ray photoelectron loss spectroscopy." C.R. Aita, C.J.G. Kubiak, N.C. Tran, and T.L. Barr, 1985 Fall Meeting of the Materials Research Society, Boston, Massachusetts, 1985.

8. "Sputter deposition and characterization of vanadium pentoxide." C.R. Aita, 15th Annual Symposium of Applied Vacuum Science and Technology, AVS and DOE co-sponsored, Clearwater Beach, Florida, 1986. (Invited)

9. "Diagnostics of sputter deposition glow discharges." C.R. Aita, Annual Symposium of the Delaware Valley Chapter of the American Vacuum Society (AVS Topical Symposium: Advances in Sputtering and Plasma Processing), King of Prussia, Pennsylvania, 1986. (Invited)

10. "Oxygen species in Ne-O_2 and Ar-O_2 rf sputter deposition discharges and their effect on Pt-O alloy film growth." Carolyn Rubin Aita, 39th Annual Gaseous Electronics Conference, Madison, Wisconsin, 1986. (Invited)

11. Production of gold-oxide ions during sputter deposition of gold films in argon-oxygen discharges." Carolyn Rubin Aita, 39th Annual Gaseous Electronics Conference, Madison, Wisconsin, 1986.

12. Low temperature oxidation on non-stoichiometric sputter deposited vanadium pentoxide: crystallography and optical behavior." C.R. Aita and M.L. Kao, 33rd National Symposium of the American Vacuum Society, Baltimore, Maryland, 1986.

13. "Interlayer spacing of sputter deposited vanadium pentoxide films." C.R. Aita, C.-K. Kwok, and M.L. Kao, 1986 Fall Meeting of Materials Research Society, Boston, Massachusetts, 1986.

14. "Optical emission spectroscopy for in situ discharge diagnostics of AlN films: relationship to film chemistry." C.J.G. Kubiak, C.R. Aita, and N.C. Tran, 1986 Fall Meeting of Materials Research Society, Boston, Massachusetts, 1986.

15. "Optical behavior of sputter deposited GeO_2 and GeO_x films." C.R. Aita, 16th Annual Symposium on Applied Vacuum Science and Technology, Clearwater Beach, Florida, February 1987. (Invited)

16. "Sputter deposition of glassy GeO_2 and GeO_x films." Carolyn Rubin Aita, Michel E. Marhic and Curt N. Sayers, 2nd Intl. Conference on the Effects of Modes of Formation on the Structure of Glasses, Vanderbilt University, Nashville, Tennessee, June 1987.

17. "Thin films by reactive sputter deposition." Carolyn Rubin Aita, Conference on the Processing of Electronic Materials, American Ceramics Society, Alfred University, Alfred, New York, July 1987. (Invited)

18. "Growth of AlN_x films in N_2-Ne, N_2-Ne-Ar, and N_2-Ar discharges; construction of ternary gas phase diagrams." James R. Siettmann and Carolyn Rubin Aita, 34th Natl. Symposium of the American Vacuum Society, Anaheim, California, November 1987.

19. "Resistivity changes and phase evolution in W-N films sputter deposited in Ne-N_2 and Ar-N_2 discharges." Karl J. Huber and Carolyn Rubin Aita, 34th Natl. Symposium of the American Vacuum Society, Anaheim, California, November 1987.

20. "Process-induced disorder in sputter deposited thin films of glassy germania." Carolyn Rubin Aita, 34th Natl. Symposium of the American Vacuum Society, Anaheim, California, November 1987.

21. "The effect on phase separation of carrier gas type (Ar, Ne, or Ne+Ar) during reactive sputter deposition of Al-N, W-N, Pt-O, and Au-O films." C.R. Aita, J.R. Siettmann, K.J. Huber, A.M. Klumb, and N.C. Tran, 17th Annual Symposium on Applied Vacuum Science and Technology, Clearwater Beach, Florida, February 1988.

IV. PARTICIPATING SCIENTIFIC PERSONNEL AND DEGREES AWARDED

1) Dr. Carolyn Rubin Aita, PI.

2) Dr. Ngoc C. Tran:
Research Associate, 7/1984-12/1987
Auger and ESCA Laboratory
University of Wisconsin-Madison

STUDENTS:

3) Charlene Jean Gawlak Kubiak:
Research Assistant, 1984-87
*PhD, December 1986.

4) William Steven Tait:
Full-time employee of S.C. Johnson & Son, Racine, WI
PhD candidate, 1984-date

5) Steven Duane Hansen:
Research Assistant, 1984
*MS, December 1984

6) James Richard Siettmann:
Research Assistant, 1984-date,
*MS, August 1987
Johnson Wax Fund Research Fellow, 9/1987-date
PhD candidate

7) Ying-Li Liu:
Graduate School Minority Fellow, 1985
*MS, December 1985

8) Karl John Huber:
Undergraduate Research Aide, 1985
BS, December 1985
Research Assistant, 1-6/1986 and 9-12/1987
Johnson Wax Fund Research Fellow, 9/1986-8/1987
*MS, August 1987
PhD candidate, 8-12/1987.

9) Mei Lee Kao:
Research Assistant, 1985-86
*MS, June 1986

10) Chee-Kin Kwok:
Research Assistant, 1986-date
*MS (Physics), June 1986
PhD candidate

11) Arlene Marie Klumb
Research Assistant, 2-4/1987
*MS, December 1987

V. APPENDICES A - K

APPENDIX A

GLOW DISCHARGE MASS SPECTROMETRY FOR SPUTTERING DISCHARGE DIAGNOSTICS

Glow discharge mass spectrometry for sputtering discharge diagnostics

Carolyn Rubin Aita
Materials Department and the Laboratory for Surface Studies, University of Wisconsin-Milwaukee, Milwaukee, Wisconsin 53201

(Received 4 October 1984; accepted 4 December 1984)

Glow discharge mass spectrometry (GDMS) is an *in situ* method used to determine the mass and energy of positive ions incident on the substrate during sputter deposition. In the first part of this review, we describe the sputtering glow discharge, creation of positive ions in the glow, determination of their mass and energy by GDMS, and the relationship between ionic flux and the flux of corresponding neutral species incident on the substrate. In the last section, several examples of the use of GDMS during reactive sputter deposition are presented, illustrating the strengths and limitations of this technique.

I. INTRODUCTION

Sputter deposition is a glow discharge process used for growing thin films of both elemental and compound materials. Although important for the reproducible production of materials with predictable properties, much remains to be learned about the manner in which discharge chemistry affects film chemistry and atomic order, from which all other properties are derived.

Glow discharge mass spectrometry (GDMS)[1] is an *in situ* method which is used to determine the mass and energy of positive ions incident on the substrate during the course a deposition. Positive ions of target species detected by GDMS are created from, and hence, their population is related to neutral species in the glow discharge. Information about the neutral flux incident on the substrate can often be obtained from a knowledge of the ionic flux.

A survey of the materials systems which have been investigated by GDMS is presented in Table I. The technique has demonstrated applicability as a basic research tool and as a means of process monitoring and control. Coburn,[1] Coburn *et al.*,[2-8] Hecq and Hecq,[9-11] and Shinoki and Itoh,[12] used GDMS to study the discharges associated with both rare and reactive gas bombardment of over 20 different target materials. Purdes *et al.*,[13] and Aita *et al.*[14-19] used GDMS as a diagnostic tool during reactive sputter deposition to understand film chemistry and structure in terms of discharge chemistry. Tisone, Bolker, and Latos[20-22] used GDMS for in-line process control.

In the next four sections of this review, we describe the sputtering glow discharge, the creation of positive ions in the glow, and the determination of their mass and average energy by GDMS. Most of the particles incident on the substrate are uncharged and the relationship between the flux of ionic species and the corresponding neutral flux is discussed in the sixth section. In the last section, several examples of the use of GDMS are presented, illustrating the strengths and limitations of this technique.

II. THE GLOW DISCHARGE

A glow discharge is one in which the cathode emits electrons under bombardment by particles and light quanta from the gas. Sputter deposition is carried out in a low pressure glow discharge (10^{-3} to 10^{-1} Torr).[23] In a planar system, the electrodes are parallel plates separated by several centimeters. The target is placed over the cathode and the substrates are placed over the anode.

The discharge is excited by applying a large negative voltage to the cathode ($\sim 10^3$ V) while the anode is kept near ground potential. Excitation can be either from a dc or rf

TABLE I. Materials systems studied by GDMS.

Target	Sputtering gas	Ref.
(1) Al	argon	18,19
(2) Au	argon	7
(3) Co	argon	4,7
(4) Cu	argon	1,6
	neon	5,7
	argon + oxygen	13
	neon + oxygen	13
(5) Eu	argon	11
(6) Nb	argon	6
(7) Ni	argon	7
(8) Pt	argon + oxygen	9
(9) Ta	argon + oxygen	20,21,22
	argon + nitrogen	16,17
(10) V	argon	4
(11) Zr	argon + nitrogen	12
(12) CdTe	argon	6
(13) NaCl	argon	4,6
(14) NiO	argon	4
(15) GaAs	argon	4,6
(16) SiO_2	argon	7
	neon	2
(17) In_2O_3	argon	4
(18) Ta_2O_5	argon	4
	argon + oxygen	20,21,22
(19) ZnO	argon + oxygen	14,15
(20) $BaTiO_3$	argon	6
(21) $Y_3Fe_5O_{12}$	argon	6
(22) EuO–6%Fe	argon	2
	neon	2
(23) Pb_xSn_{1-x}	argon	4
(24) Sb_2O_3–Y_2O_3	argon	4
(25) MnCrSb	argon	4
(26) CoNi alloy	argon	4
(27) NiCu alloy	argon	6
(28) MnGaGe alloy	argon	6
(29) CuTa alloy	argon	6
(30) FeAlCu alloy	argon	1,4
(31) Teflon	argon	6

source. In a dc-excited system, the target is part of the cathode and must be conducting. In an rf-excited system, the target need not be conducting.[24–26] However, to insure that an equal number of positive and negative charge carriers strike its surface in an rf half cycle, the target develps a negative self-bias that can be nearly as large as the amplitude of the rf voltage applied to the cathode.[24,27]

Distinct striations of darkness and light develop parallel to the electrodes. Sequentially from cathode to anode, these regions are[28]:

(1) The Aston dark space, where electrons accumulate to be accelerated away from the negative field at the target surface.

(2) The cathode glow, primarily associated with the loss of excitation when positive ions sputtered from the target are neutralized by electrons near the target surface.

(3) The cathode or Crookes dark space, through which (a) electrons are accelerated away from the target, thereby gaining sufficient energy to ionize gas species efficiently, and (b) positive ions are accelerated towards the target, thereby gaining sufficient momentum to cause sputtering when they strike the target surface.

The width of the Crookes dark space is determined by the mean free path over which an electron is accelerated before undergoing inelastic collisions with gas species which randomize its motion. A large number of positive ions are created as a result of these initial collisions, and a strong positive space-charge region develops at the boundary of the Crookes dark space and the negative glow.

(4) The negative glow, a plasma sustained by the ionization of gas species by impact with electrons. The negative glow is a region of intense radiation, the color of which is characteristic of the sputtering gas between the electrodes.

(5) The anode sheath, a Langmuir sheath which forms around an object placed in contact with a plasma.

The discharge is abnormal and obstructed. "Abnormal" refers to the condition when the entire cathode surface is covered by the negative glow. "Obstructed" refers to the placement of the anode close enough to the cathode so that it is in the negative glow; neither Faraday dark space, positive column, anode dark space, nor anode glow develops.

The electric field drops from a high value at the target surface to zero at the boundary between the Crookes dark space and the negative glow, which acts as a virtual anode. The motion of both electrons and positive ions changes from beamlike in the Crookes dark space to random in nature in the negative glow.

The potential drops from the large negative value V_c at the target surface to zero at the boundary of the Crookes dark space and the negative glow. The potential rises in the negative glow to a small positive value V_p (the plasma potential) relative to the potential at the anode surface V_a. The surface of an anode that is not a perfect conductor floats at a small negative potential with respect to ground.

Sputtering occurs when gas species originating as positive ions in the negative glow are accelerated across the Crookes dark space and after undergoing symmetric charge exchange collisions, $X^+(\text{fast}) + X^0(\text{slow}) \rightarrow X^+(\text{slow}) + X^0(\text{fast})$, strike the target as high energy neutral species.[29] Target species are ejected by a momentum transfer process, with energies on the order of 1 to 10 eV.[30] Most of the ejected target species are uncharged, assume a random motion between the electrodes, and condense on any surface in their path. In this manner, a film is deposited on the substrate. However, high energy neutral gas species which have been elastically scattered from the target surface,[31] fast electrons which have not been slowed down by inelastic collisions,[32–35] and positive ions from the negative glow with energy equal to $V_p - V_a$[1,3] also strike the substrate, adding to the complexity of the environment in which the film grows.

It is sometimes advantageous to apply a small external voltage, usually with a negative bias, to the anode. Increasing negative values of V_a increase the maximum energy $(V_p - V_a)$ with which positive ions strike the substrate. Enhanced bombardment by rare gas ions increases the resputtering of material from the growth interface concurrent with deposition and decreases the amount of loosely bound impurities incorporated into the film.[36–38] Other effects of a negative anode bias are discussed in Sec. VII C.

III. PRODUCTION OF POSITIVE IONS

A positive ion produced at the target by the sputtering process will be unable to leave the strong cathode field and will be neutralized near or returned to the target surface. It is important to emphasize, therefore, that positive ions of target species detected by GDMS are created in the negative glow.

Several direct ionization processes which can occur are[39]:

(1) Ionization of a ground state atom or molecule by a collision with an electron with kinetic energy greater than the first ionization potential of the neutral species.

(2) Ionization of a ground state atom or molecule species by an elastic collision with a positive ion whose velocity is such that both momentum and energy are conserved.

(3) Ionization of a ground state atom or molecule by a collision with an excited atom with total energy equal to or greater than the first ionization potential of the neutral species. A special case is Penning ionization[40,41] in which the excited atom is at a metastable energy level from which a radiative transition to the ground state is forbidden. Rare gas atoms have long lived metastable states immediately above the ground state (Table II[42]) with sufficient energy to ionize many elemental and compound target species. Penning ionizaiton is an important process for the creation of positive ions from neutral minority species in the negative glow.

(4) Associative ionization,[41,43–45] the formation of an ionic complex by a collision between an excited atom and an atom

TABLE II. Low-lying metastable energy levels of rate gas atoms.

Species	Metastable energy, eV	Ionization energy, eV
1. He	19.8, 20.7	24.58
2. Ne	16.6, 16.7	21.56
3. Ar	11.5, 11.7	15.76
4. Kr	9.9, 10.5	14.00
5. Xe	8.3, 9.4	12.13

or molecule in its ground state. The complex ion is stabilized because the electron released by the reaction carries away the heat of reaction in the form of kinetic energy.[43] Associative ionization is responsible for the formation of ions in the glow for which there are no corresponding neutral species, for rare gas dimer ions, and for rare gas–reactive gas ionic complexes.[2–4,6,12–16,46,47]

(5) Ionization of a ground state atom or molecule by absorption of a photon of energy equal to or greater than the first ionization potential of the neutral species.

(6) Nonresonant transfer of charge between an excited atom and a ground state molecule which may become excited to a repulsive energy level and dissociate.

Indirect ionization processes can also occur. These are cumulative processes which involve a sequence of excitation collisions ultimately leading to an ionizing event.

IV. DETECTION OF POSITIVE IONS BY GDMS

Glow discharge mass spectrometry was first described by Coburn.[1] A typical experimental setup by which GDMS is accomplished is shown in Fig. 1. The GDMS apparatus is differentially pumped and maintained at a pressure of $\sim 10^{-6}$ Torr. The system with which we have worked consists of a sampling orifice positioned in the substrate table. Beneath the orifice is an ion extractor lens—a three element Einsel lens and a magnetic separator by which the ion beam is collimated and secondary electrons are separated out. After passing through the ion extractor lens, the ion beam enters a quadrupole mass analyzer where particles are separated on the basis of mass-to-charge ratio. The output signal, detected by either a channeltron or a Faraday cup, represents the ion current from a particular combination of mass and charge, from which the chemical type of the ion is deduced. Difficulty in interpretation arises because different combinations of mass and charge can have the same mass-to-charge ratio, and hence, yield overlapping signals.

The factor that distinguishes GDMS from traditional residual gas analysis is that in the latter, an ionization process external to the glow discharge is used to create ions from neutral species which are sampled from the sputtering chamber. Ions detected by GDMS are created in the negative glow in the natural course of events during the sputtering process.

The least complicated spectra are generated by sputtering an elemental target in a rare gas. More complicated spectra are generated when:

(1) A compound target is sputtered in a rare gas. In this case, dissociation of the target material can occur either at the target surface under bombardment by energetic particles[26] or by collisional processes in the discharge,[48] as evidenced by the dominance of atomic species in the spectra shown in Figs. 2 and 3(a).

(2) An elemental target is sputtered in a reactive gas (Fig. 4). In this case, a chemical reaction can occur at the target surface and/or at the substrate.[49–51] The flux incident on the substrate is determined by a balance between compound formation at and removal from the target surface without dissociation and compound dissociation at the target surface and in the discharge.

(3) A compound target sputtered in a reactive gas [Fig. 3(b)]. The same balance cited in case (2) applies here.

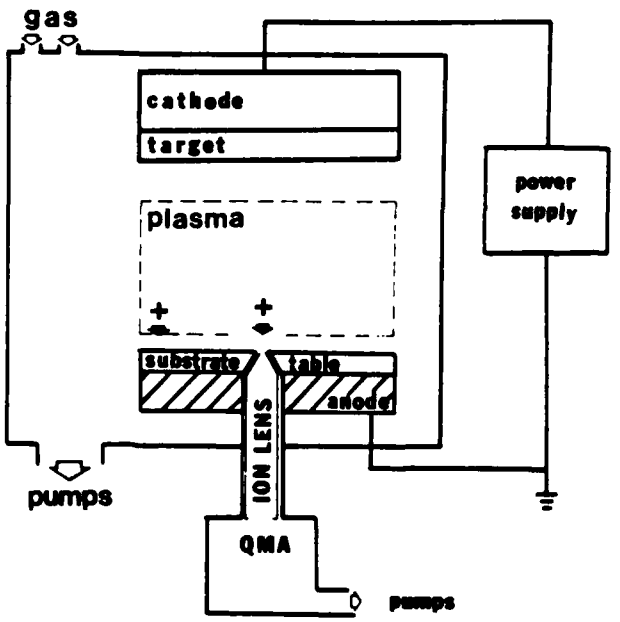

FIG. 1. Sputter deposition system with an attached glow discharge mass spectrometer.

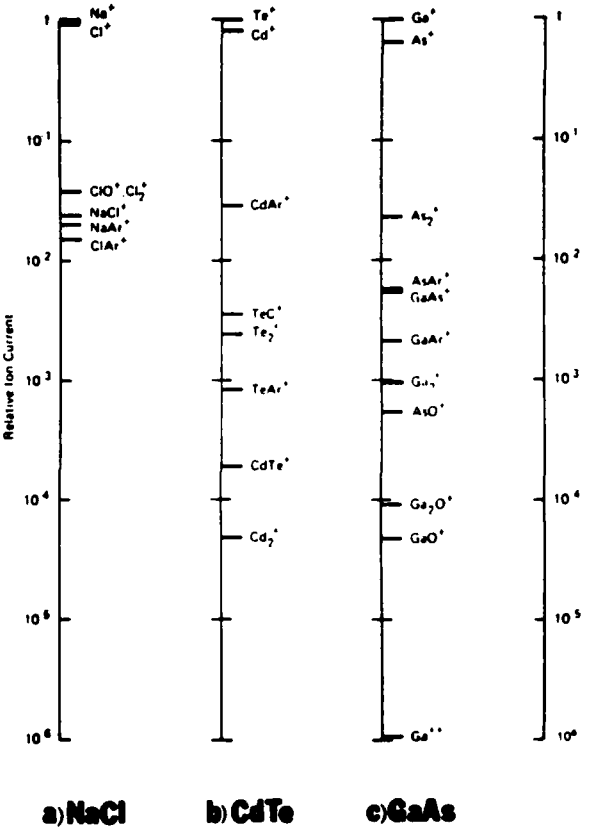

FIG. 2. Ionic current from various compound targets sputtered in an rf-excited discharge operated at 6×10^{-2} Torr and 100 W power: (a) NaCl, (b) CdTe, (c) GaAs. Only signals from ions bearing target species are included (Ref. 3).

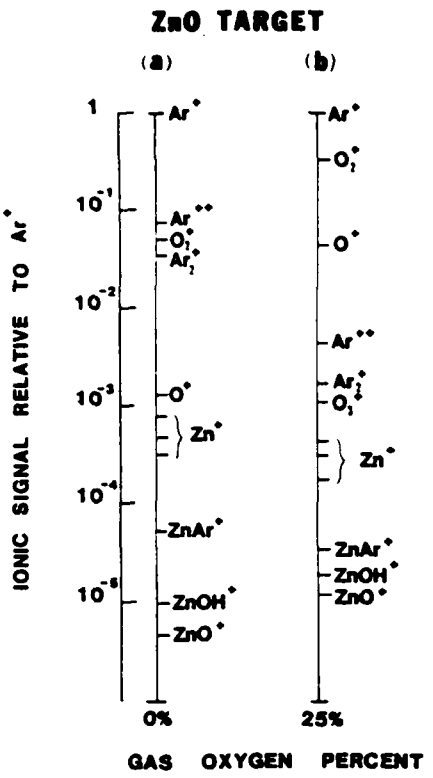

FIG. 3. Ionic current obtained by sputtering a ZnO target in an rf-excited discharge containing (a) Ar, and (b) 75% Ar/25% O_2 operated at 1×10^{-2} Torr with -1000 V (rms) applied to the cathode. Three isotopes of Zn (64, 66, 68 amu) are shown. Their relative ionic current is equal to their abundance in nature. Current corresponding to the formation of ZnO and ZnOH from each isotope can also be observed, but for the sake of clarity, only the current from $Zn^{66}O^+$ and $Zn^{66}OH^+$ is shown in the figure (Ref. 14).

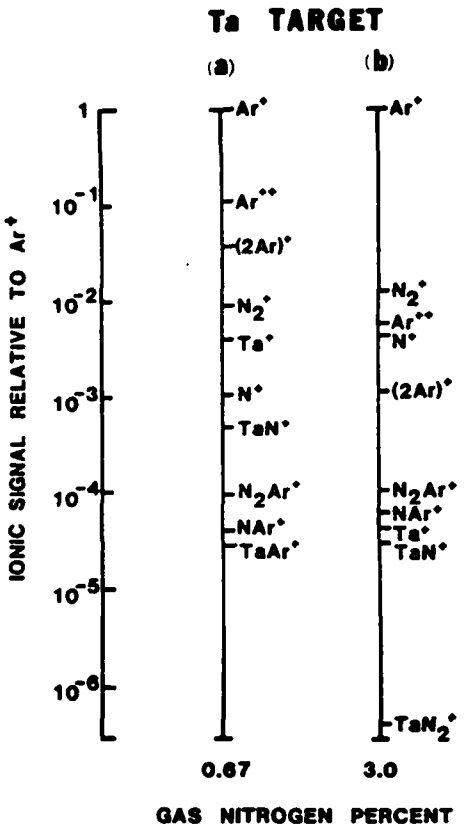

FIG. 4. Ionic current obtained by sputtering a Ta target in an rf-excited Ar discharge containing (a) 0.67% N_2, and (b) 3.0% N_2 operated at 1.5×10^{-2} Torr with -725 V (rms) applied to the cathode (Ref. 16).

V. MEASUREMENT OF PLASMA POTENTIAL

Using the apparatus described above, the average energy of a particular ionic species in the negative glow can be measured by applying an increasing positive retarding voltage to one of the three ion extractor lens elements and observing the output signal of the quadrupole mass analyzer for the species of interest using a Faraday cup with the anode at ground potential ($V_a = 0$). When the retarding potential is equal to the potential at which ions arrive from the negative glow, no positive ions pass through the lens and no current is detected.

A study of the effect of discharge geometry and anode biasing on the plasma potential of various ionic species in rf discharges was carried out by Coburn and Kay.[3] The results show an increase in V_p with decreasing target-to-wall area ratio in contact with the discharge. A negative anode bias does not effect V_p. In general, single positive charged species do not undergo symmetric charge exchange collisions in the anode sheath. Whitten[52] found that V_p measured from the Ar^+ ion current increases slowly with decreasing discharge pressure and increasing power.

VI. RELATIONSHIP OF ION TO NEUTRAL FLUX

When a target of element X is sputtered in a rare gas in which there is a concentration of species $[R^m]$ excited to a metastable electronic level with energy equal to or greater than the first ionization potential of X, the ion current X^+ was found to be directly proportional to the product $[R^m][X]$, where $[X]$ is the concentration of neutral target atoms in the negative glow.[5] This result indicates that the ionization of X occurs by the Penning process.

In terms of relating ionic to neutral flux, the cross section for Penning ionization is known not to significantly vary from element to element.[41] The relative ion current from target molecules and their fragments from a compound target was found to be a good indicator of the relative flux of the corresponding neutral species incident on the substrate provided that all species involved can be Penning ionized by metastables of the particular sputtering gas used in the experiment.[6] Complications in interpretation arise when a sputtered target species cannot be Penning ionized because of energy considerations. In such cases, a simple correspondence between the relative ionic current and the neutral flux of a particular species cannot be made.

Another problem arises when relative ionic currents are used to estimate the relative yields from a molecular target; that is, to attempt to quantify the extent of dissociation at the target surface. This cannot be done because dissociative processes occur in the negative glow as well as at the target surface. The GDMS spectra will therefore appear to be more atomic in nature than is representative of the flux of neutral species which leave the target surface.

VII. APPLICATIONS

Three specific cases in which GDMS was used during reactive sputter deposition are discussed briefly in this section.

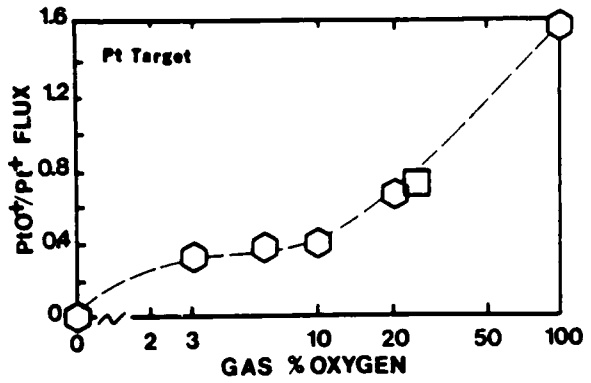

FIG. 5. Relative PtO^+/Pt^+ ionic current obtained by sputtering a Pt target in rf-excited Ar/O_2 discharges operated at 1×10^{-2} Torr with -1000 V (rms) applied to the cathode, shown as a function of gas O_2 content. Hexagons represent data obtained in our laboratory, the square represents data from Ref. 9.

A. Detection of platinum target oxidation

A small amount of O_2 added to an Ar discharge during the reactive sputter deposition of Pt results in the growth of a type of platinum oxide.[53–56] A comparison of the dependence of oxide growth on cathode voltage and deposition rate in Ar/O_2 nd Ne/O_2 discharges suggest that Pt–O bond formation in the film is controlled by the oxidation of Pt metal at the target surface.[56]

Initial supporting evidence came from Hecq *et al.*[9] who detected both PtO^+ and PtO_2^+ species by GDMS when a Pt target was sputtered in an $Ar/25\%$ O_2 rf discharge. Pt^+ and PtO^+ ionic current intensities were monitored in our laboratory during the sputtering of a Pt target in Ar/O_2 discharges. The PtO^+/Pt^+ relative ionic intensity is shown in Fig. 5. Since both Pt and PtO (with first ionization potentials at 9.0 and 11.2 eV, respectively) are Penning ionizable by Ar^m, the relative ionic flux shown in Fig. 5 represents the corresponding flux of neutral species incident on the substrate. GDMS has been used here (1) to verify that oxidation of the Pt target occurs, and (2) to show that even for very small amounts of O_2 in the sputtering gas, a significant number of neutral PtO species are incident on the substrate.

B. Relationship of the Zn^+/ZnO^+ flux to the structure of ZnO films

Zinc oxide, a hexagonal close-packed wurtzite-type compound, is an important material for piezoelectric transducer applications. For an optimal piezoelectric response, the basal planes of the ZnO crystallites must be oriented parallel to the substrate.

GDMS studies of the sputtering of a ZnO target in Ar/O_2 discharges show that considerable dissociation of the compound occurs for all partial pressures of O_2 [see, for example, Fig. 3(b)].[14,15] Furthermore, a minimum in the Zn^+/ZnO^+ ionic flux [Fig. 6(a)] is strongly correlated with the number of basal planes aligned parallel to the substrate [Fig. 6(b)]. The Zn^+/ZnO^+ ionic flux was found to be dependent upon both sputtering gas O_2 content[14] and the discharge power.[15]

It is tempting to assume the Zn^+/ZnO^+ flux is an accurate indicator of the relative number of neutral Zn and ZnO

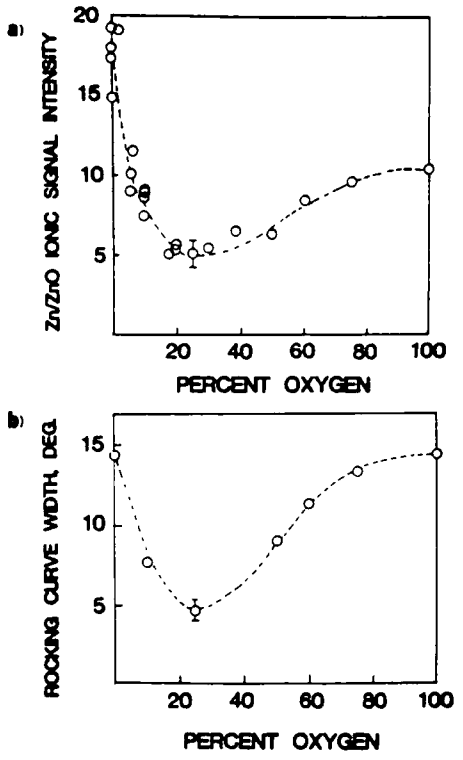

FIG. 6. (a) The relative Zn^+/ZnO^+ current shown as a function of sputtering gas O_2 content. (b) The average deviation of the normal to ZnO basal planes from the substrate normal, obtained by x-ray diffraction rocking measurements on films grown from a ZnO target sputtered in rf-excited discharges operated at 1×10^{-2} Torr with -1000 V (rms) applied to the cathode (Ref. 14).

species incident on the substrate and correlate a strong basal orientation in the films with the number of species which arrive already in oxide form. However, this cannot be done. Zinc, with a first ionization potential of 9.39 eV is the only neutral species in this system for which it is certain that Penning ionization by Ar^m can occur. The first ionization potential of ZnO is not known. Therefore, although the ZnO–O–Ar system lends itself well to the use of GDMS as a process control procedure (by controlling O_2 partial pressure, rf power to minimize the Zn^+/ZnO^+ flux), its use to obtain information about the relative flux of neutral species in this system is limited.

C. Enhancement of Ta^+ flux and arrival energy by anode biasing during reactive deposition of tantalum nitride

A negative bias voltage applied to the anode during the reactive deposition of Ta in atmospheres containing small amounts of N_2 results in a lower film resistivity and in the stabilization Ta_2N, the transition phase between N-doped bcc Ta and fcc TaN.[57] GDMS was used[9,17] to correlate these results with an increase in (1) the Ta^+ flux relative to TaN^+, and (2) the energy of the arriving Ta^+ ions. Ta^+ flux and energy enhancement for a given sputtering gas N_2 content increases the atomic density of Ta atoms in the films with consequent changes in crystal structure and electrical behavior.

VIII. SUMMARY

Presented above is an introduction to glow discharge mass spectrometry, an *in situ* method for determining the mass and energy of positive ions incident on the substrate during sputter deposition. Our goal was to demonstrate the use of GDMS to gain information about the relationship of discharge chemistry to film growth.

The examples presented in this review illustrate the use of GDMS during reactive sputter deposition to determine: (1) the oxidation or nitridization of a metal target. (2) The relative neutral flux of target species incident on the substrate, provided that the ions detected by GDMS are created from these neutrals by the Penning process. (3) The relative ionic flux of target species, regardless of the means by which the ions are created. The intent here is either to gain information about the effect of ionic flux on a particular film property, or to use the ionic flux ratio for process control.

ACKNOWLEDGMENTS

Acknowledgment is made of discussions with G. C. Whitten, M. E. Marhic, M. G. Lagally, and J. W. Coburn essential to the preparation of this paper, and of the assistance of T. A. Myers and J. M. Mennig with collection of much of the GDMS data presented here. Work done at University of Wisconsin was supported by a gift from the Digital Equipment Corporation and under U.S. Army Research Office Project No. 21334-MS.

[1]J. W. Coburn, Rev. Sci. Instrum. **41**, 1219 (1970).
[2]J. W. Coburn and E. Kay, Appl. Phys. Lett. **18**, 435 (1971).
[3]J. W. Coburn and E. Kay, J. Appl. Phys. **43**, 4965 (1972).
[4]J. W. Coburn, E. Taglauer, and E. Kay, J. Appl. Phys. **45**, 1779 (1974).
[5]E. W. Eckstein, J. W. Coburn, and E. Kay, Int. J. Mass Spectrom. Ion Phys. **17**, 129 (1975).
[6]J. W. Coburn, E. W. Eckstein, and E. Kay, J. Vac. Sci. Technol. **12**, 151 (1975).
[7]J. W. Coburn, E. W. Eckstein, and E. Kay, J. Appl. Phys. **46**, 2823 (1975).
[8]J. W. Coburn and E. Kay, J. Chem. Phys. **64**, 904 (1976).
[9]M. Hecq, A. Hecq, and T. Robert, J. Vac. Sci. Technol. **16**, 960 (1979).
[10]M. Hecq and A. Hecq, Thin Solid Films **76**, 35 (1981).
[11]M. Hecq and A. Hecq, J. Appl. Phys. **56**, 872 (1984).
[12]F. Shinoki and A. Itoh, J. Appl. Phys. **46**, 3381 (1984).
[13]A. J. Purdes, B. F. T. Bolker, J. D. Bucci, and T. C. Tisone, J. Vac. Sci. Technol. **14**, 98 (1977).
[14]C. R. Aita, A. J. Purdes, R. J. Lad, and P. D. Funkenbusch, J. Appl. Phys. **51**, 5533 (1980).
[15]C. R. Aita, R. J. Lad, and T. C. Tisone, J. Appl. Phys. **51**, 6405 (1981).
[16]C. R. Aita, T. A. Myers, and W. J. LaRocca, J. Vac. Sci. Technol. **18**, 324 (1981).
[17]C. R. Aita and T. A. Myers, J. Vac. Sci. Technol. A **1**, 348 (1983).
[18]C. R. Aita, J. Appl. Phys. **53**, 1807 (1982).
[19]C. R. Aita and C. J. Gawlak, J. Vac. Sci. Tenolol. A **1**, 415 (1983).
[20]T. C. Tisone and T. S. Latos, United States Patent No. 4172020, October 23, 1979.
[21]T. C. Tisone, B. F. T. Bolker, and T. S. Latos, J. Vac. Sci. Technol. **17**, 415 (1980).
[22]B. F. T. Bolker, T. C. Tisone, and T. S. Latos, J. Vac. Sci. Technol. **18**, 328 (1981).
[23]See for example, J. A. Thornton, in *Deposition Technologies for Film and Coatings*, edited by R. F. Bunshah (Noyes, Park Ridge, New Jersey, 1982), pp. 170–237.
[24]G. S. Anderson, W. N. Mayer, and G. K. Wehner, J. Appl. Phys. **38**, 2991 (1967).
[25]P. D. Davidse and L. I. Maissel, J. Appl. Phys. **37**, 574 (1966).
[26]J. L. Vossen and J. J. O'Neill, Jr., RCA Rev. **1968**, 149.
[27]H. S. Butler and G. S. Kino, Phys. Fluids **6**, 1346 (1963).
[28]See, for example, A. Von Engel, *Ionized Gases* (Clarendon, Oxford, 1965), pp. 217–257.
[29]W. D. Davis and T. A. Vanderslice, Phys. Rev. **131**, 219 (1963).
[30]G. K. Wehner, G. S. Anderson, and L. Maissel, in *Handbook of Thin Film Technology*, edited by L. I. Maissel and R. Glang (McGraw-Hill, New York, 1970), pp. (3)3–38, (4)2–41.
[31]J. A. Thornton and D. W. Hoffman, J. Vac. Sci. Technol. **18**, 203 (1981).
[32]L. T. Lamont, Jr., and A. Lange, J. Vac. Sci. Technol. **7**, 198 (1970).
[33]D. G. Muth, J. Vac. Sci. Technol. **8**, 99 (1971).
[34]I. Brodie, L. T. Lamont, Jr., and D. O. Myers, J. Vac. Sci. Technol. **6**, 124 (1969).
[35]D. J. Ball, J. Appl. Phys. **43**, 3047 (1972).
[36]L. I. Maissel and P. M. Schaible, J. Appl. Phys. **36**, 237 (1965).
[37]R. Frerichs, J. Appl. Phys. **33**, 1898 (1962).
[38]R. Frerichs and C. J. Kircher, J. Appl. Phys. **34**, 3541 (1963).
[39]H. S. W. Massey and E. H. S. Burhop, *Electronic and Ionic Impact Phenomena* (Clarendon, Oxford, 1968), Vol. 1.
[40]F. M. Penning, Z. Phys. **46**, 225 (1925); **57**, 723 (1929).
[41]H. Hotop and A. Niehaus, Z. Phys. **215**, 1395 (1968); **228**, 68 (1969).
[42]Reference 26, p. 43.
[43]J. A. Hornbeck and J. P. Molnar, Phys. Rev. **84**, 621 (1951).
[44]Z. Herman and V. Cermak, Nature **199**, 588 (1963).
[45]J. L. Franklin, Adv. Chem. Ser. **72**, 1 (1968).
[46]C. R. Aita and M. E. Marhic, J. Appl. Phys. **52**, 6584 (1981).
[47]C. R. Aita and M. E. Marhic, J. Vac. Sci. Technol. A **1**, 69 (1983).
[48]E. G. Jones and A. G. Harrison, Int. J. Mass Spectrom. Ion Phys. **5**, 137 (1970).
[49]E. Hollands and D. S. Campbell, J. Mater. Sci. **3**, 544 (1968).
[50]J. Heller, Thin Solid Films **17**, 163 (1973).
[51]T. Abe and T. Yamashina, Thin Solid Films **30**, 19 (1975).
[52]G. C. Whitten, Final Technical Report, NSF Faculty Research Participation Project No. Ser 76-04790.
[53]M. Hecq, A. Hecq, J. P. Delrue, and T. Robert, J. Less-Common Met. **64**, 25 (1979).
[54]M. Hecq and A. Hecq, J. Vac. Sci. Technol. **18**, 219 (1981).
[55]C. R. Aita and Ngoc C. Tran., J. Appl. Phys. **54**, 6052 (1983).
[56]C. R. Aita and Ngoc C. Tran., J. Appl. Phys. **56**, 963 (1984).
[57]E. Krikorian and R. J. Sneed, J. Appl. Phys. **37**, 3647 (1966).

APPENDIX B

GROWTH OF Al AND Al-NITRIDE FILMS IN N_2-Ne AND N_2-(Ne+Ar) DISCHARGES: CONSTRUCTION OF A TERNARY GAS PHASE DIAGRAM

J. Vac. Sci. Technol. A 6 May-June 1988 (in Press)

JVST
Abstract#263
Program#TF-TuP1

GROWTH OF Al AND Al-NITRIDE FILMS IN N_2-Ne AND N_2-(Ne+Ar) DISCHARGES: CONSTRUCTION OF A TERNARY GAS PHASE DIAGRAM.

James R. Siettmann and Carolyn Rubin Aita
Materials Department and the Laboratory for Surface Studies
University of Wisconsin-Milwaukee
P.O. Box 784
Milwaukee, Wisconsin 53201

ABSTRACT

An Al target was sputtered in N_2, N_2-Ne, and 5%N_2-(Ne+Ar) discharges. The resulting films were studied by x-ray diffraction, Rutherford backscattering spectroscopy, and resistivity measurements. The results were combined with data previously obtained for the N_2-Ar system. A three-gas composition diagram was constructed onto which phase evolution in the films was mapped.

In general, phase evolution proceeded as follows: Al->microcrystalline cermet->microcrystalline AlN->multiorientation AlN->single basal orientation AlN. For the same nominal discharge N_2 content, the use of Ne in place of Ar as the rare gas component of the discharge surpressed the formation of the Al, cermet, and microcrystalline AlN phases, and enlarged the region over which basal orientation AlN was formed. In situ optical emission spectroscopy data suggested that this result is related to an increased N_2^+/Al° flux in the discharge when Ne rather than Ar gas was used.

I. INTRODUCTION

AlN coatings cannot be formed by a vapor-solid reaction between an Al surface and ground state N_2 molecules because Al does not chemisorb this species.[1] AlN can, however, be grown by sputter deposition. In a previous study,[2] we reported that when an Al target was sputtered in Ar-N_2 discharges, phase evolution proceeded from metallic Al to a short range order or microcrystalline phase to AlN oriented with basal planes parallel to the substrate as the nominal N_2 content of the discharge was increased. Phase evolution was related to an increase in the number of N_2^+ ions in the discharge.

In the present study, we investigated the use of Ne and Ne+Ar mixtures as the rare gas component of the discharge. Ne atoms in low lying metastable energy states (E_m=16.6, 16.7eV) can Penning ionize[3] ground state N_2 by a radiationless transfer of excitation to produce N_2^+, whereas Ar atoms in low-lying metastable energy states (E_m=11.5, 11.7eV) cannot. Film crystallography was determined by x-ray diffraction (XRD). Rutherford backscattering spectroscopy (RBS) was used to obtain chemical data on selected samples. Electrical resistivity of conducting films was measured at room temperature. Phase evolution was determined as a function of the nominal discharge composition. Combined with the results obtained for the Ar-N_2 system,[2] we began to construct a ternary N_2-Ne-Ar gas composition diagram on which to map phase evolution in the films. In addition, optical emission spectroscopy was used to monitor the relative number of neutral Al atoms and N_2^+ ions in the discharge volume as a function of discharge composition and phase evolution is discussed in terms of these species.

II. EXPERIMENTAL PROCEDURE

Films were grown in a Model 8620J MRC rf (13.56MHz) diode sput-

ter deposition apparatus. A 13cm-diam, 99.9995% Al target was thermally bonded to a water-cooled stainless steel cathode. Supersil quartz and <111>-cut Si substrates were placed on a water-cooled Cu pallet. The portion of the pallet not covered by the substrates was coated with Al followed by AlN prior to deposition to prevent backsputtering of Cu into the growing film. The anode-cathode spacing was 7cm. The cathode voltage was -1700V(p-p) and the anode was at ground potential for all depositions.

Prior to deposition, the chamber was evacuated to $\leq 8 \times 10^{-7}$torr with a liquid N_2-trapped, hot Si-base oil diffusion pump. The gases were admitted separately into the chamber to a total pressure of 1×10^{-2}torr. Depositions were carried out in discharges containing: 1) 100%N_2, 2) N_2-Ne containing 5-95%N_2, 3) 5%N_2-95%(Ne+Ar) containing (10%Ne+85%Ar)-(85%Ne+10%Ar), and 4) 5%N_2-95%Ar. The purity of the gases was 99.999% for Ar and N_2 and 99.996% for Ne.

Two presputters proceeded each deposition. The purpose of the first presputter, carried out in pure Ar for 1h, was to remove the oxide layer formed on the target surface upon exposure to air.[4] The second presputter, carried out in the gas composition of choice, allowed time for the discharge and target reactions to reach a state of dynamic equilibrium. A movable shutter covered the substrates during the presputters. The shutter was opened and films were deposited for 1h. Specific deposition parameters are recorded in Table I.

A Model HR320 Instruments SA optical spectrometer with a 2400 groove/mm holographic grating capable of 0.5Å resolution was used for in situ optical emission studies. Radiation emitted from the discharge region between anode and cathode was sampled through

an 8cm-diam glass window with a transmission cut-off at 3200Å. The window was shuttered when data was not being taken to prevent intensity decreases in the course of the experiment due to window coating. The output data was in the form of light intensity as a function of wavelength. In particular, two emission peaks were monitored: 1) The Al[4s($^2S_{1/2}$)->3p($^2P_{3/2}$)] transition at 3961Å.[5] This transition corresponds to the de-excitation of a neutral Al atom from its first excited state to the ground state, and is used here to probe the relative concentration of ground state Al^o. 2) The $N_2^+[B^2\Sigma_u^+ \rightarrow X^2\Sigma_g^+]$ transition (first negative band system) with a ν_{00} band head at 3914Å.[6] The first negative band system corresponds to de-excitation to ground state N_2^+ and is used here to probe the relative concentration of this species in the discharge. Al^o is assumed to originate as a sputtered target species and N_2^+ created by ionizing collisions with various species, e.g. e^-, Ne^m, in the plasma volume.

Film crystallography was determined by double angle x-ray diffraction using unresolved CuKα radiation. Peak position (2θ), relative intensity (I), and full width at one half maximum intensity were determined. The interplanar spacing (d) was calculated using the Bragg relationship: $n\lambda=2d\sin\theta$. The diffractometer was calibrated to the $\{10\bar{1}1\}$ diffraction peak of a quartz standard at $2\theta=26.66\pm0.02^o$. The width of the peak, which was 0.18^o, was assummed to represent broadening solely from instrument effects.

Film thickness was measured using a Tencor Alpha-200 Model profilometer with an instrument accuracy of ±5%. Growth rate was determined from this measurement and is recorded in Table I. Sheet resistance was measured on conducting films using a four-point

probe .[7] Resistivity was calculated from sheet resistance and thickness using the method described in Ref. (7). Rutherford backscattering spectroscopy was used to determine the Al and N atomic concentration in selected films. An IonX Model 4175 analyzer equipped with 2MeV He^{++} bombarding ions was used.

III. RESULTS AND DISCUSSION

A. Film Characteristics:

The appearance of films on quartz substrates under transmitted visible light and the resistivity of films on Si are recorded in Table I. No entry indicates that resistivity was too large to measure with a four-point probe. Crystallographic data of all films on quartz and N/Al atomic concentration of selected samples are recorded in Table II.

From the data presented here, it can be seen that films deposited in 100%N_2 (Run 1) and N_2-Ne containing 5-90%N_e (Runs 2-9) are basal orientation AlN. The{0002} planes of the hcp wurtzite AlN lattice structure in individual crystallites are oriented parallel to the substrate. The {0002} interplanar spacing for unstressed bulk AlN is 2.49Å.[8] The relationship $\varepsilon=(c-c_o)/c_o$ was used to calculate the deviation of the lattice parameter $c=2d_{\{0002\}}$ from that of bulk AlN, c_o. The value of ε ranges from 0 to +0.008, indicating a tensile stress in the film perpendicular to the substrate plane. This value should not be interpreted as long range elastic strain in the AlN lattice based on a continuum model.[9] Instead, ε should be taken to be the average value of short range strain due to isolated imperfections in the film which disrupt the periodicity of the lattice[10] (e.g. displaced or missing atoms from allowed lattice sites, incorporation of foreign impurities

such as Ne, H_2O, and C).

Films deposited in 5%N_2-95%Ne (Run 10) are multiple orientation AlN with {0002}, {1120}, and {1013} planes oriented parallel to the substrate. The ratio of the intensities, as shown in Table II, is 100:21:16, which is different than that for a polycrystalline powder sample of AlN.[8] The film though multioientation, shows a preferred {0002} texture.

Films deposited in N_2 and N_2-Ne discharges are electrical insulators, colorless, and transparent. Spectrophotometry measurements in absorption mode[11] not reported here showed that the band gap was 5.9-6.1eV when determined from a short wavelength limit approximation and 6.1eV when determined from the point at which the fundamental absorption band intensity was equal to one-half its maximum value.[12]

The next step in the study involved replacing various amounts of Ne with Ar as the rare gas component of the discharge while holding the N_2 content fixed at 5%. The rationale for choosing this value for N_2 content is as follows. We have shown above that a transition from multiorientation -> single basal orientation AlN occurs when the discharge composition is changed from 5%N_2-95%Ne -> 10%N_2-90%Ne. In a previous study,[2] we have shown that films deposited in 5%N_2-95%Ar have an Al metal structure, which is verified here (Run 18), and a transition to non-metallic properties begins to occur when the gas N_2 content is increased above 5%. So two transition points have been identified in terms of discharge composition: the end points of the 5%N_2-95%(Ne+Ar) system. We now wish to extend these two points into a line, or range of phases.

Runs 11-15, deposited in 5%N_2-95%(Ne+Ar) containing 10-29%Ar showed no well-defined diffraction peaks. The low intensity peaks present in some samples are similar to those reported[2] for depositions in N_2-Ar discharges containing from 20 to less than 50%N_2. These peaks can be attributed to prism {hki0} and dome {h0il} AlN lattice planes. This material has only short range order or microcrystallinity. The large change in resistivity from insulator (Runs 11-13) to moderate conductor (Run 14) to better conductor (Run 15) suggests that these films are cermets with differing amounts of ceramic (AlN) and metal (Al) components on a submicron scale. The N/Al atomic concentration in this series of films changes from ≥ 1 (Runs 12 and 13) to ≤ 1 (Runs 14 and 15, taking into account experimental error. Commensurate with the change in chemistry is a color change from clear (Runs 12 and 13) to dark brown (Runs 14 and 15), and an increase in reflectivity.

Runs 16 and 17 deposited in 5%N_2-95%(Ne+Ar) containing 47.5 and 85%Ar showed diffraction from the Al lattice[13] and had a resistivity close to that of pure Al. The surface of these films, as well as that of films deposited in 5%N_2-95%Ar (Run 18) was opaque grey-black. This surface coating was easily removed by rubbing revealing an underlying grey-black metallic film. The film-quartz interface, viewed from the underside of the substrate, was highly reflective grey-black.

The results presented above are summarized in the three-gas composition diagram shown in Fig. 1. This drawing was constructed by the method used to construct ternary phase diagrams. Each gas composition is represented by a point relative to the three sides of an equilateral triangle, the corners of which represent the

unmixed gases. Tentative phase field boundaries, drawn here as dashed lines, were estimated by assuming that phase evolution varies as a linear combination of the volume of N_2, Ar, and Ne in the discharge. This assumption may not hold in every case. Determination of precise phase boundaries will be the subject of future research.

B. Optical Emission Spectroscopy

In an optically thin plasma, the emission intensity I_{ki} of a transition from level k->level i is proportional to $(h\nu_{ik}A_{ki}n_k)$, where $h\nu_{ik}$ is the energy of the emitted photon, A_{ki} is the Einstein coefficient for spontaneous emission, and n_k is the population of the upper level.[14] Here, we use relative changes in the intensity ratio: $I[N_2^+(3914\text{Å})]/I[Al^\circ(3961\text{Å})]$ to estimate changes in the ratio of the upper level populations and hence in the ratio of the ground state populations of N_2^+ and Al° species in the discharge. The number of each species in the discharge is assummed to be proportional to the number that strike the substrate. It was suggested in Ref. (2) that the factor that limits the formation of AlN at the substrate is the arrival of N_2^+ species. Therefore, a large $I[N_2^+(3914\text{Å})]/I[Al^\circ(3961\text{Å})]$ ratio should promote AlN growth, a small ratio favors Al growth.

$I[N_2^+(3914\text{Å})]/I[Al^\circ(3961\text{Å})]$ is shown in Fig. 2a as a function of gas N_2 content for N_2-N_e and N_2-Ar discharges. Figure 2b shows the intensity ratio as a function of Ar content in $5\%N_2$-95%(Ne+Ar) mixtures, that is, gas mixtures that lie along the vertical line connecting the two data points at $5\%N_2$ in Fig. 2a.

A comparison of Fig. 2 with the data presented in Tables I and II along with our knowledge of the N_2-Ar system shows that Al is

is deposited (Runs 16-18) when the $I[N_2^+]/I[Al^o]$ ratio is ≤ 0.3. Transparent, colorless films which are crystallographically or chemically identifiable as AlN are deposited when $I[N_2^+]/I[Al^o]$ is ≥ 0.9. These films include microcrystalline (Runs 12 and 13, and depositions in N_2-Ar containing 20 to $<50\%N_2$), multiorientation (Run 10), and single basal orientation (Runs 1-9, and depositions in N_2-Ar containing $\geq 50\%N_2$) structures. When $I[N_2^+]/I[Al^o]$ is less than 0.9 and greater than 0.3, the series of films that result (Runs 11, 14, and 15) are microcrystalline, range in appearance from pale brown transparent to dark brown reflective, and in electrical behavior from insulator to conductor.

From the data presented in this section, it can be seen that the use of the $I[N_2^+(3914\text{Å})]/I[Al^o(3961\text{Å})]$ ratio to predict phase changes driven by the relative arrival flux of N_2^+ and Al^o species, that is, transition from Al->AlN_x->AlN, is possible. However, once the intensity ratio has exceeded the limit at which AlN is deposited, the prediction of the structure of AlN (microcrystalline, multiorientation, or basal orientation) is not possible from gas system to system.

IV. SUMMARY

An Al target was sputtered in N_2, N_2-Ne, and $5\%N_2$-(Ne+Ar) discharges. The resulting films were studied by XRD, RBS, and resistivity measurements. The results were combined with data previously obtained for the N_2-Ar system. A three-gas composition diagram was constructed onto which phase evolution in the films was mapped.

In general, phase evolution in sputter deposited Al-N alloys proceeded as follows: Al->microcrystalline cermet->microcrystalline AlN->multiorientation AlN->single basal orientation AlN. For the

same nominal discharge N_2 content, the use of Ne in place of Ar as the rare gas component of the discharge surpressed the formation of the Al, cermet, and microcrystalline AlN phases, and enlarged the region over which basal orientation AlN was formed. Optical emission intensity data suggests that this result is related to an increased N_2^+/Al^o flux in the discharge when Ne rather than Ar gas is used.

Acknowledgements: The authors thank Dr. C.N. Sayers for obtaining the RBS data and Prof. B. Brown for enabling us to use the XRD facilities in the Department of Geological Sciences, UW-Milwaukee. This work was supported by the E.I. Du Pont de Nemours Co. and under U.S. ARO Grant No. DAAG29-84-K-0126.

REFERENCES

[1] G. Ehrlich, Proc. Eighth International Summer Institute in Surface Science (R. Vanselow, editor, CRC Press, Boca Raton, Florida, 1987).

[2] C.R. Aita and C.J. Gawlak, J. Vac. Sci. Technol. A 1, 403 (1983).

[3] F.M. Penning, Z. Phys. 46, 225 (1925); 57, 723 (1929).

[4] C.R. Aita, J. Appl. Phys. 53, 1807 (1982).

[5] G. Herzberg, Atomic Spectra and Atomic Structure (Dover, New York, 1944) p. 198.

[6] G. Herzberg, Spectra of Diatomic Molecules (Van Nostrand, Princeton, New Jersey, 1950) p. 554.

[7] L.B. Valdes, Proc. IRE 42, 420 (1954).

[8] Jt. Comm. on Powder Diffraction Standards (1974), Powder Diffraction File No. 25-1134.

[9] S. Maniv, W.D. Westwood, and E. Colombini, J. Vac. Sci. Technol. 20, 162 (1982).

[10] C.J. Gawlak and C.R. Aita, J. Vac. Sci. Technol. A 1, 415 (1983).

[11] J.R. Siettmann, Growth of AlN_x Films in N_2-Ne, N_2-Ne-Ar, and N_2-Ar Discharges: Construction of Ternary Gas Composition Diagrams. MS Thesis. University of Wisconsin-Milwaukee, 1987.

[12] T.S. Moss, Optical Properties of Semi-Conductors (Butterworth, London, 1961) pp. 38-43.

[13] Ref. 8, Powder Diffraction File No. 4-787.

[14] Ref. 6, p. 20.

TABLE I: DEPOSITION PARAMETERS, GROWTH RATE, VISUAL APPEARANCE, AND RESISTIVITY OF SPUTTER DEPOSITED AL AND AL-NITRIDE FILMS.

RUN	SPUTTERING GAS			POWER (W)[a]	RATE (Å/MIN)[b]	VISUAL APPEARANCE[c]	RESISTIVITY (μΩ-CM)[d]
	$\%N_2$	%NE	%AR				
1.	100	0	0	500	59±3	CLEAR TRANS	
2.	95	5	0	500	70±3	CLEAR TRANS	
3.	90	10	0	500	75±4	CLEAR TRANS	
4.	80	20	0	550	67±4	CLEAR TRANS	
5.	65	35	0	475	83±7	CLEAR TRANS	
6.	50	50	0	410	66±10	CLEAR TRANS	
7.	35	65	0	390	46±7	CLEAR TRANS	
8.	20	80	0	340	42±2	CLEAR TRANS	
9.	10	90	0	310	68±4	CLEAR TRANS	
10.	5	95	0	260	64±8	CLEAR TRANS	
11.	5	85	10	225	93±2	PALE BR TRANS	
12.	5	76	19	220	93±11	CLEAR TRANS	
13.	5	74	21	220	97±6	CLEAR TRANS	
14.	5	71	24	220	127±6	DARK BR TRANS	218.8±0.3
15.	5	66	29	235	130±3	DARK BR. REFL	84.3±0.6
16.	5	47.5	47.5	240	220±4	GR-BL OPAQUE	6.6±0.5
17.	5	10	85	240	298±10	GR-BL OPAQUE	3.3±0.3
18.	5	0	95	250	272±6	GR-BL OPAQUE	4.5±0.4

[a] CATHODE VOLTAGE=1700V(P-P) FOR ALL DEPOSITIONS

[b] ERROR REPRESENTS ±1SD

[c] TRANS=TRANSPARENT, REFL=REFLECTIVE, BR=BROWN, GR-BL= GREY-BLACK

[d] RESISTIVITY PURE AL=2.8μΩ-CM

TABLE II: CRYSTALLOGRAPHIC PARAMETERS AND CHEMISTRY OF SPUTTER DEPOSITED AL AND AL-NITRIDE FILMS.

RUN	2θ(DEG)	FWHM(DEG)	D(Å)	PLANE	REL I	N/AL AT.CONC.
1.	36.05	0.38	2.49	ALN 0002		
2.	36.06	0.37	2.49	ALN 0002		
3.	36.06	0.30	2.49	ALN 0002		
4.	36.03	0.30	2.49	ALN 0002		
5.	36.01	0.34	2.49	ALN 0002		
6.	35.82	0.29	2.51	ALN 0002		
7.	36.00	0.32	2.50	ALN 0002		
8.	36.00	0.30	2.50	ALN 0002		
9.	35.97	0.29	2.50	ALN 0002		
10.	35.91	0.34	2.50	ALN 0002	100	
	56.40	1.20	1.85	ALN $11\bar{2}0$	21	
	66.30	2.20	1.41	ALN $10\bar{1}3$	16	
11.						1.2±0.2
12.	NO LONG RANGE ORDER DETECTABLE BY XRD					1.3±0.2
13.						0.9±0.1
14.						0.8±0.1
15.						
16.	38.53	0.24	2.34	AL 111		
17.	38.54	0.24	2.34	AL 111	100	
	44.78	0.25	2.02	AL 200	41	
18.	38.48	0.26	2.34	AL 111	100	
	44.72	0.28	2.03	AL 200	40	

FIGURE CAPTIONS:

Fig. 1. Ternary gas composition (N_2-Ne-Ar) diagram onto which phase evolution in sputter deposited Al and Al-nitride films is mapped.

Fig. 2 The ratio of optical emission intensities from the ν_{00} band head of the $N_2^+[B\rightarrow X]$ transition at 3914Å and the $Al^o[4s\rightarrow 3p]$ transition at 3961Å as a function of a) discharge N_2 content in the N_2-Ne and N_2-Ar gas systems, and b) discharge Ar content in the 5%N_2-(Ne+Ar) gas system.

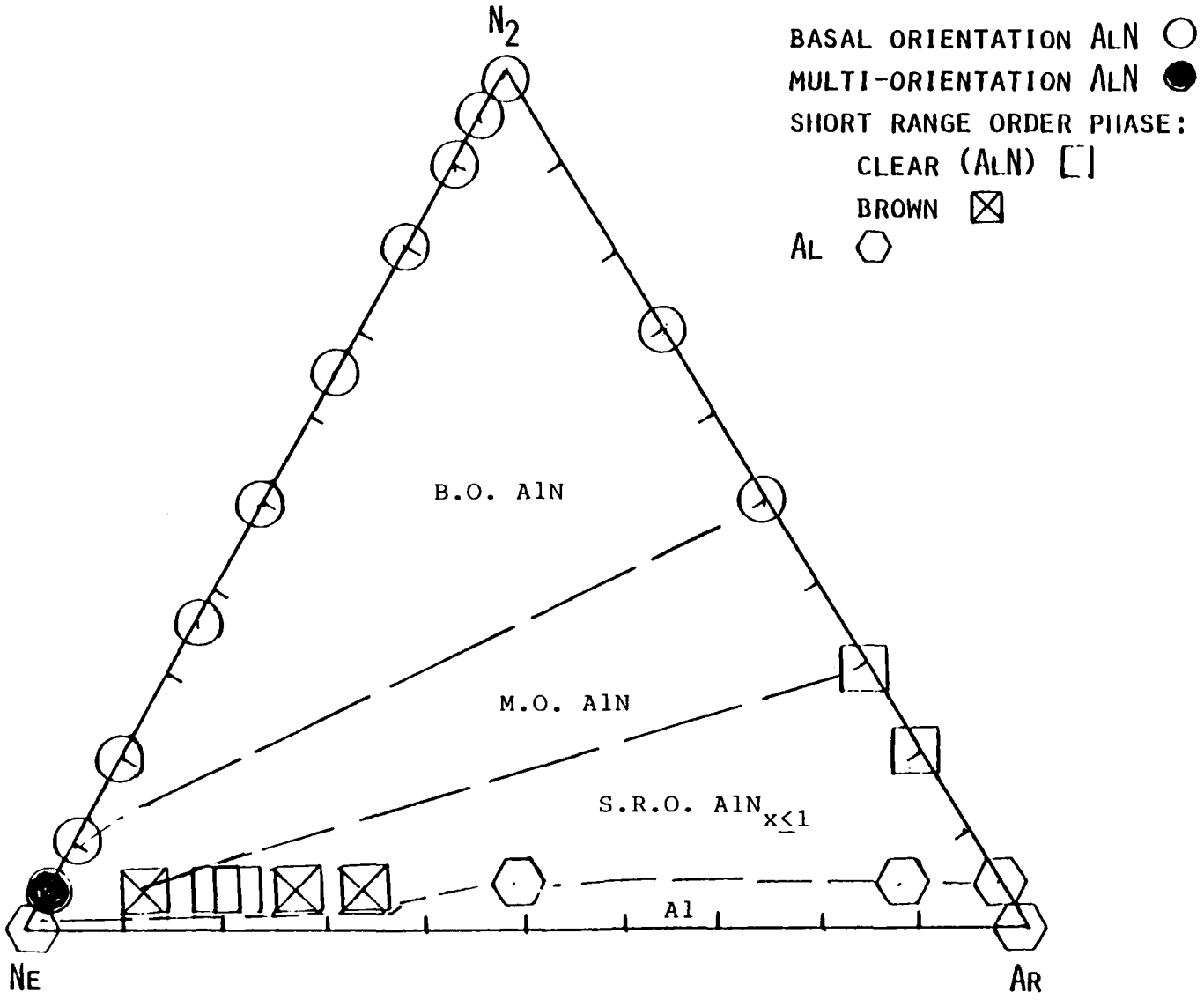
N2
BASAL ORIENTATION AlN
MULTI-ORIENTATION AlN
SHORT RANGE ORDER PHASE:
CLEAR (AlN)
BROWN
Al
B.O. AlN
M.O. AlN
S.R.O. AlN x≤1
Al
NE
AR

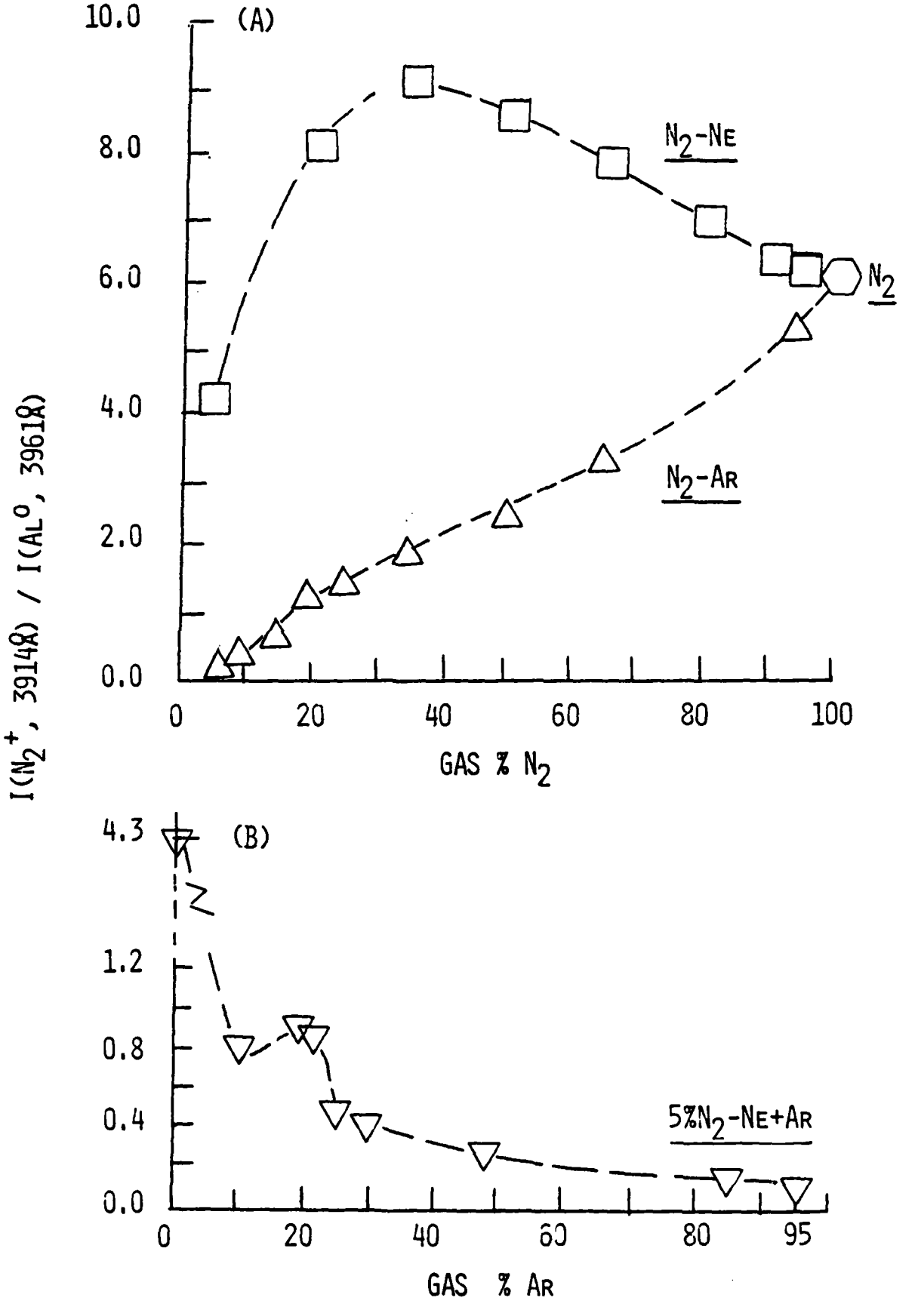
(A)
10.0
8.0
6.0
4.0
2.0
0.0
0
20
40
60
80
100
GAS % N2
I(N2+, 3914Å) / I(AL°, 3961Å)
N2-NE
N2-AR
N2
(B)
4.3
1.2
0.8
0.4
0.0
0
20
40
60
80
95
GAS % AR
5%N2-NE+AR

APPENDIX C

Al, Al-N ALLOY, AND AlN-COATED STEEL CORROSION BEHAVIOR IN O_2-FREE KCl SOLUTIONS

Abstract # : 608
Program # : AS1-MoM6
Put on JVST manuscript

J. Vac. Sci. Technol. A 6 May-June 1988 (in press)

Al, Al-N ALLOY, AND AlN-COATED STEEL CORROSION BEHAVIOR IN O_2-FREE KCl SOLUTIONS

W. S. Tait
S.C. Johnson & Son Inc
Racine, Wisconsin 53403

C. O. Huber
Department of Chemistry
University of Wisconsin-Milwaukee
Milwaukee, Wisconsin 53201

B. C. Begnoche
E. I. Du Pont de Nemours Co. Inc.
Imaging Systems Department
Florence, South Carolina 29501

J. R. Siettmann[a] and C. R. Aita[b]
Materials Department and the Laboratory for Surface Studies
University of Wisconsin-Milwaukee
P.O. Box 784
Milwaukee, Wisconsin 53201

ABSTRACT

Al, Al-N alloy cermet, and AlN films were grown on 1008 steel substrates using reactive sputter deposition. Corrosion rates of the steel+coating composite in an O_2-free 0.2M KCl electrolyte were measured under conditions of cathodic polarization. The results show that an AlN coating lowered the corrosion rate of steel by over an order of magnitude. However, the corrosion rate was enhanced and under certain conditions exceeded that of steel when Al-N alloy cermet and Al coatings were used. This phenomenon was explained in terms of a reactive porous electrode model.

---

a) Johnson Wax Fund Research Fellow
b) send all correspondence to this author

I. INTRODUCTION

Mild steel is resistant to corrosion in dry air but rapidly corrodes when exposed to an aqueous environment. Alloying with more corrosion-resistant metals,[1] coating the surface with organic films,[2] and adding corrosion inhibitors to the aqueous environment,[3] are examples of conventional methods used to increase steel corrosion resistance. Recently, glass metal alloy coatings,[4] ion implantation coatings,[5] reactive sputter deposited coatings,[6,7] and plasma assisted chemical vapor deposited coatings[8] on steel have been studied. While these coatings result in better steel corrosion resistance, they are often susceptable to degradation by aggressive anionic species such as Cl^- ions. In order to address this deficiency, we researched the potential use of sputter deposited Al-nitride coatings on mild steel. In the present study, we investigated the corrosion behavior of sputter deposited Al, Al-N alloys, and AlN in the presence of O_2-free KCl solutions. AlN is a III-V refractory compound that is insoluble in H_2O and only sparingly soluble in boiling 5M HCl.[9] This material, therefore, appears to be a good candidate for resistance to Cl^- ion degradation.

II. EXPERIMENTAL PROCEDURE AND RESULTS

A. Film Preparation and Properties:

Films were grown by reactive sputter deposition on 16mm-diam 1008 steel discs. The composition of the steel is 99.45%Fe, 0.08%C, 0.45%Mn, 0.007%P, and 0.017%S. The surface of the steel discs were polished using a 5μm particle size diamond slurry, ultrasonically cleaned using a triple solvent procedure (10min in tricholorethylene, acetone, and ethyl alcohol successively), and dried in hot dry air.

A Model 8620J MRC rf diode apparatus was used for film growth. The details of the deposition process for these materials, as well as their characterization, are given in Ref. 10. To summmarize here, an Al target was sputtered in 5%N_2-95%(Ne+Ar) discharges in which the Ne/Ar ratio was varied. The deposition parameters used for specific runs are recorded in Table I.

Film crystal structure, appearance on quartz substrates under transmitted visible light, and electrical resistivity are also recorded in Table I. It can be seen that there is a phase evolution in the films from multiorientation AlN (Run A) -> microcrystalline AlN (Run B) -> microcrystalline cermet with increasing electrical conductivity (Runs C and D) -> multiorientation Al (Run E) as the ratio of Ne/Ar in the discharge was decreased.

Microstructure of the as-deposited films was investigated using scanning electron microscopy. Micrographs of the film surface in secondary electron emission mode are shown in Fig. 1. It can be seen that Runs A and B, which are AlN, have a fine microstructure barely resolvable at 20kX magnification. Run C, a cermet, shows bimodal growth. It was not possible to distinguish composition differences between large and small grains in our instrument. However, based on an argument that the energy barrier, hence critical radius for nucleation varies inversely with the melting point of the material,[11] it is likely that the cermet is two phase: the large grains being the Al component and the small grains the AlN component. Run D, which is a cermet of lower resistivity and higher reflectivity (hence more metallic), also shows bimodal growth but with a greater volume of larger grains (Al) than Run C. Run E, which is Al, has a large-

grained microstructure. Cross-sectional examination of Run E showed that the porous structure shown in Fig. 1e was indeed representative of the film throughout its thickness.

B. Electrochemical Measurements:

Electrochemical measurements were made by using the film+steel sample as the test electrode in a Model K47 EG&G Princeton Applied Research corrosion cell. The principle behind the measurment is as follows. An electrode in solution at its open circuit potential V_o has both oxidation (anodic) and reduction (cathodic) reactions occurring at its surface. When the electrode potential is moved approximately $\pm$50mV from V_o by applying a voltage V, the electrode surface reaction becomes predominately cathodic or anodic, depending upon the polarity of V. In this study, we applied a negative voltage, which suppressed the anodic reaction at the test electrode. Thus, the only possible electrode reaction was the reduction of an electrochemically active species from solution, e.g. H^+. The current density, I, resulting from the applied voltage was directly proportional to the active species' reduction rate.

The relationship between current and overpotential, $V-V_o$, for an electrode in an efficiently stirred solution (one in which mass transport to the electrode is not a determining factor of I) is expressed by the Butler-Volmer form of the Tafel equation,[12]

$$I=I_o\left\{\exp\left[-\alpha nF(V-V_o)/RT\right]\right\} \qquad (1)$$

where I_o is the exchange current density whose physical significance is discussed below, n is the number of electrons/species engaging in

the electrochemical reaction, α is the transfer coefficient,[13] F is Faraday's constant, R is the ideal gas constant, and T is the ambient temperature.

The exchange current density is obtained graphically by extrapolating the linear portion of a cathodic polarization curve of I versus V to V_o, as shown schematically in Fig. 2. O_2 was purged from the test electrolyte in our study. Therefore, the only possible cathodic reaction at the test electrode at V_o was the reduction of H^+ ions. If we consider the coating to be electrochemically inert, the overall corrosion reaction of interest here is,

$$Fe^o + 2H^+ \rightarrow Fe^{+2} + H_2^o \qquad (2)$$

and the cathodic half-cell reaction is,

$$2H^+ + 2e^- \rightarrow H_2^o . \qquad (3)$$

The exchange current density is a measure of the exchange rate for the reaction described by Eq. (2), hence a measure of the steady-state corrosion rate for the electrode. I_o is used here as the parameter by which to characterize Al, Al-N alloy, and AlN-coated steel corrosion rates.

A 0.2M KCl electrolyte solution was prepared from 18MΩ-cm deionized H_2O and analytical reagent grade KCl. The electrolyte was N_2-sparged for 12 to 16h prior to test electrode immersion and sparging was continued throughout the test to insure that O_2 was not present. Test electrodes were equilibrated in solution for 24h prior

to cathodic polarization.

Cathodic polarization curves were generated by applying an increasingly negative voltage up to -250mV greater than V_o. A scan rate of 0.1mV/s was used. The values for V_o were determined to be -715mV for Run A, -723mV for Run B, 750±31mV for Run C, -675mV for Run D, and -666mV for Run E. V_o for Fe is equal to -660mV and -1882mV for pure Al.[14] A saturated calomel electrode with a Luggin probe salt bridge was used as a reference for V. Test solutions were vigorously stirred with a Teflon-coated magnetic bar during the polarization experiments. After testing, the electrode was removed from solution and dried with hot N_2 gas.

The values of I_o calculated from the cathodic polarization curves are shown in Fig. 3 as a function of discharge Ar content.

III. DISCUSSION

After 24h in 0.2M KCl solution, it can be seen from Fig. 3 that there is a wide difference in corrosion behavior represented by the five coatings investigated here. I_o was lowest for AlN-coated steel (Runs A and B), increased by more than an order of magnitude for cermet-coated steel (Runs C and D), and by over two orders of magnitude for Al-coated steel. An uncoated steel electrode yielded I_o values between 4.1 and 5.5μA/cm^2, and a commercial grade 1100 Al electrode (1.0%Si+Fe, 0.05-0.2%Cu, 0.05%Mn, 0.10%Zn) yielded I_o =3μA/cm^2.

From the data presented in Fig. 3 and the values for Al and bare steel, we conclude that AlN (Runs A and B) is electrochemically inert on steel and Eq. (2) can be applied to describe the corrosion reaction. The film is also non-porous with respect to providing internal

surfaces for reaction. There are two processes which lead to H^+ ion reduction through combination with an e^- under these conditions:

1) e^- transfer (possibly accompanied by Fe^{+2} migration) from the substrate-film interface through the film to the film-electrolyte interface where the reduction reaction given by Eq. (3) occurs.

2) H^+ diffusion from the electrolyte-film interface through the film to the film-substrate interface where the reduction reaction occurs.

At the other extreme, Al, when deposited on steel, enhances steel corrosion, as evidenced by the fact that I_o for Run E is larger than I_o for uncoated steel. The value of I_o for bulk Al is lower than that for steel. Therefore, the enhancement of the corrosion rate observed for Run E is not due to the corrosion of Al alone, but to an interaction between Al and Fe, and to the porosity of the electrode.[15] Al and Fe have different values of V_o. Therefore, a galvanic reaction between these two metals is possible. As a consequence, the following reactions can occur at the reactive, porous electrode:

1) Al^o (solid) participates in a reduction reaction with the electrolyte within the film pores,[16]

$$2Al^o + 6H^+ \rightarrow 2Al^{+3} + 3H_2^o . \qquad (4)$$

2) Al^o (solid) and Fe^{+2} (in solution) form a galvanic cell within the film pores at the Al-Fe interface. The cell reaction is,

$$2Al^o + 3Fe^{+2} \rightarrow 2Al^{+3} + 3Fe^o . \qquad (5)$$

The product Fe^{o} is deposited on the substrate in the vicinity of the of the Al-Fe interface. Away from the Al-Fe interface, Fe corrodes according to Eq. (2).

3) Fe in a +2 oxidation state reacts with water in the electrolyte,

$$Fe^{+2} + 2H_2O^{o} \rightarrow Fe(OH)_2^{o} + 2H^{+}. \quad (6)$$

This reaction is especially damaging because the production of H^{+} lowers the electrolyte pH in the pore, thereby increasing the local corrosion rate of Fe^{o}.

4) A reaction similar to Eq. (6) occurs for Al^{+3} in the electrolyte,

$$2Al^{+3} + 3H_2O^{o} \rightarrow 2Al(OH)_3^{o} + 6H_2^{+}. \quad (7)$$

This reaction, as in the case of Eq. (6), increases the production of H^{+} thereby further increasing Fe^{o} and Al^{o} corrosion rates.

Reactions in the vicinity of a pore in a reactive electrode are schematically shown in Fig. 4.

IV. SUMMARY

Al, Al-N alloy cermet, and AlN films were grown on 1008 steel substrates using reactive sputter deposition. Corrosion rates of the steel+coating composite in an O_2-free 0.2M KCl electrolyte were measured under conditions of cathodic polarization. The results show

that an AlN coating lowered the corrosion rate of steel by over an order of magnitude. However, the corrosion rate was enhanced and under certain conditions exceeded that of steel when Al-N alloy cermet and Al coatings were used. This phenomenon was explained in terms of a reactive porous electrode model.

Acknowledgments: The authors thank Dr. C.J.G. Kubiak for helpful comments. Corrosion testing was carried out by W.S.T. at S.C. Johnson and Son. J.R.S. was supported by a S.C. Johnson Research Fellowship. C.R.A. was supported by a grant from the E.I. Du Pont de Nemours Co. and under U.S. ARO Grant No. DAAG29-84-K0126.

REFERENCES

1) H.H. Uhlig, Corrosion and Corrosion Control (Wiley, New York, 2nd ed., 1971) p.119.

2) H. Liedheiser, Jr., Corrosion 38, 1 (1982).

3) N.E. Hamner, in Corrosion Inhibitors (edited by C.C. Natan, NACE, Houston, 1973) p.1.

4) H. Yoshioka, S. Yoshida, A. Kawashima, K. Asami, and K. Hashimoto, Corrosion Sci. 26, 795 (1986).

5) P. Agarwal, P. Nath, H.J. Doerr, R.F. Bunshah, G. Kuhlman, and A.J. Koury, Thin Solid Films 83, 37 (1981).

6) H.E. Townsend, H.J. Cleary, and L. Allegra, Corrosion 37, 348 (1981).

7) R. Wang and M.D. Merz, Corrosion 40, 272 (1984).

8) W.J. James, Proc. Electrochem. Soc. 84, 292 (1984).

9) K.M. Taylor and C. Lenie, J. Electrochem. Soc. 107, 308 (1960).

10) J.R. Siettmann and C.R. Aita, AVS 1987 National Symposium, Abs#263, Program# TF-TuP1 (manuscript in review).

11) C.A. Neubegauer, in Handbook of Thin Film Technology (edited by L.I. Maissel and R. Glang, McGraw-Hill, New York, 1970).

12) A.J. Bard and L.R. Faulkner, Electrochemical Methods: Fundamentals and Applications, (Wiley, New York, 1980) p. 103.

13) K.J. Vetter, "Electrochemical Kinetics (Academic, New York, 1967) p. 97.

14) K.E. Heusler and W.J. Lorenz, in Standard Potentials in Aqueous Solution (edited by A.J. Bard, R. Parsons, and J. Jordon, Dekker, New York, 1985) p. 407.

15) H. Kaesche, Metallic Corrosion (NACE, Houston, 1985) pp. 322, 340.

16) "Pore" is used here to mean any internal surface.

TABLE I: DEPOSITION PARAMETERS AND MATERIALS PROPERTIES OF SPUTTER DEPOSITED AL AND AL-NITRIDE FILMS

RUN	SPUTTERING GAS			POWER	THICKNESS	APPEARANCE[c]	RESISTIVITY	STRUCTURE
	$\%N_2$	%NE	%AR	(W)[a]	(μM)[b]		(μΩ-CM)[d]	
A.	5	95	0	260	1.0	CLEAR TRANS	INSULATOR	MULTIORIENT-ATION ALN
B.	5	76	19	220	1.4	CLEAR TRANS	INSULATOR	MICROCRYSTAL-LINE ALN
C.	5	71	24	220	1.1	DARK BR TRANS	218.8±0.3	MICROCRYSTAL-LINE CERMET
D.	5	66	29	235	1.1	DARK BR REFL	84.3±0.6	MICROCRYSTAL-LINE CERMET
E.	5	47.5	47.5	240	1.4	GR-BL OPAQUE	6.6±0.5	MULTIORIENT-ATION AL

a) CATHODE VOLTAGE = -1700V (P-P); DISCHARGE PRESSURE = 10^{-2} TORR

b) ±20%

c) UNDER VISIBLE TRANSMITTED LIGHT. TRANS=TRANSPARENT, REFL=REFLECTIVE, BR=BROWN, GR=BL=GREY-BLACK (ON QUARTZ SUBSTRATES).

d) RESISTIVITY OF PURE AL (BULK)=2.8μΩ-CM

FIGURE CAPTIONS

FIG. 1: Scanning electron micrographs of the surface of as-deposited films on steel substrates: a) Multiorientation AlN, clear transparent insulator; b) Microcrystalline AlN, clear transparent insulator; c) Micorcrystalline Al+AlN cermet, dark-brown transparent conductor (ρ=218.8μm-cm); d) Microcrystalline Al+AlN cermet, dark-brown transparent conductor (ρ=84.3μm-cm); e) Multiorientation Al (ρ=6.6μm-cm).

FIG. 2: A cathodic polarization curve showing V_o, the open circuit potential and I_o, the exchange current density.

FIG. 3: The exchange current density as a function of the Ar content of the sputtering discharge.

FIG. 4: Electrochemical reactions in the vicinity of a pore of reactive electrode near the film-substrate interface.

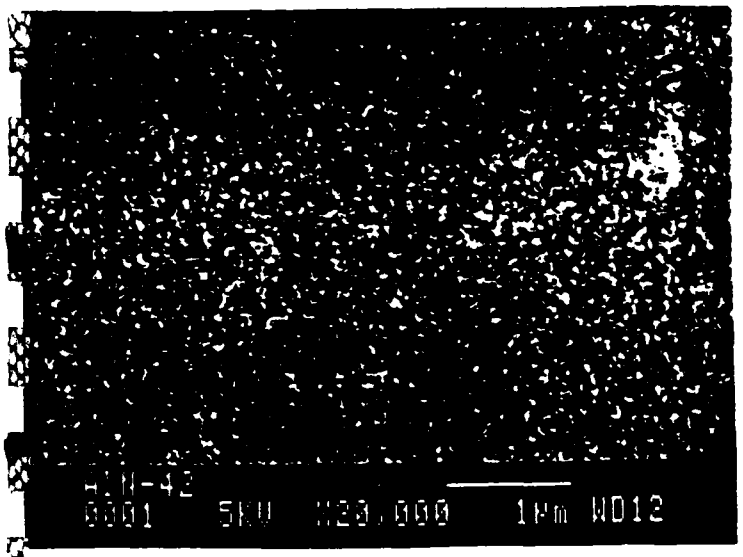
AlN-42
0001 5KV X20,000 1μm WD12

1A

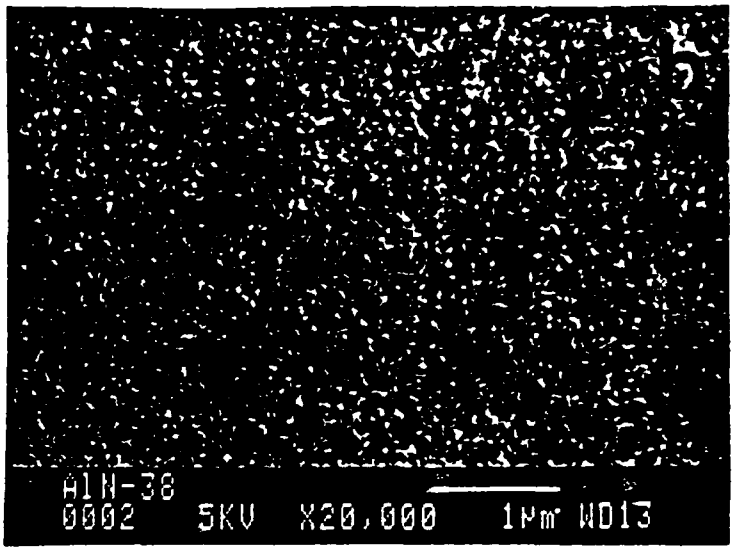
AlN-38
0002 5KV X20,000 1μm WD13

1B

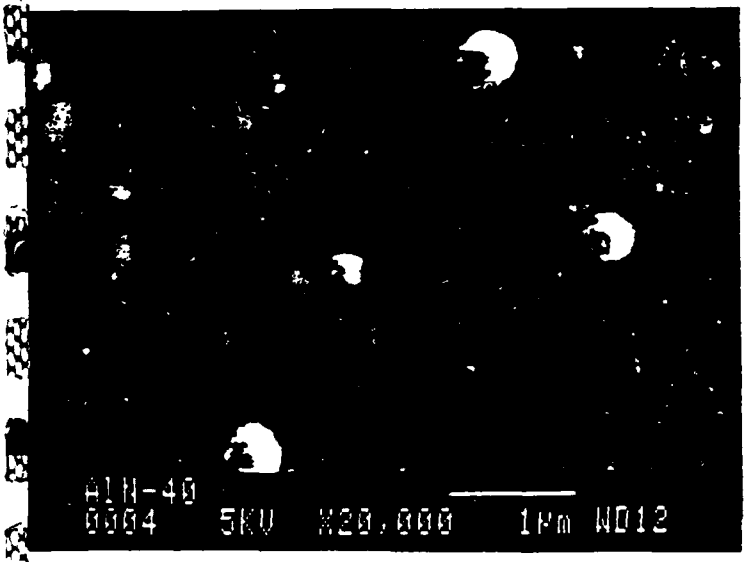
AlN-40
0004 5KV X20,000 1μm WD12

1C

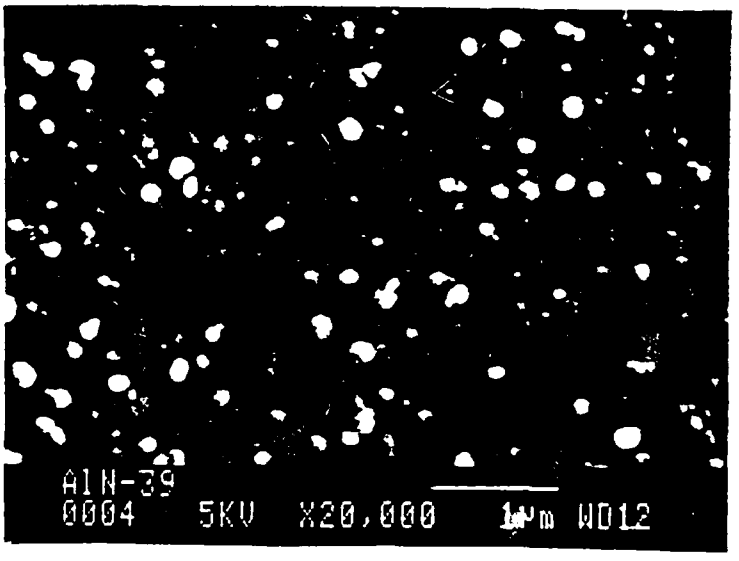
AlN-39
0004 5KV X20,000 1μm WD12

1D

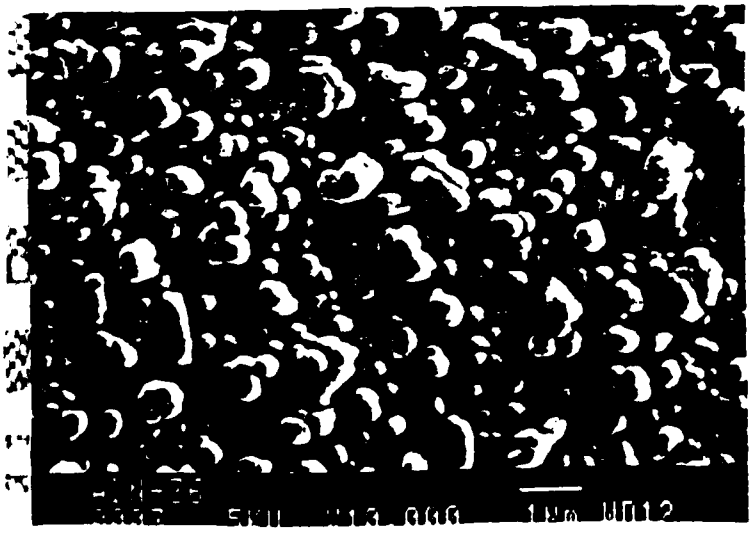

1E

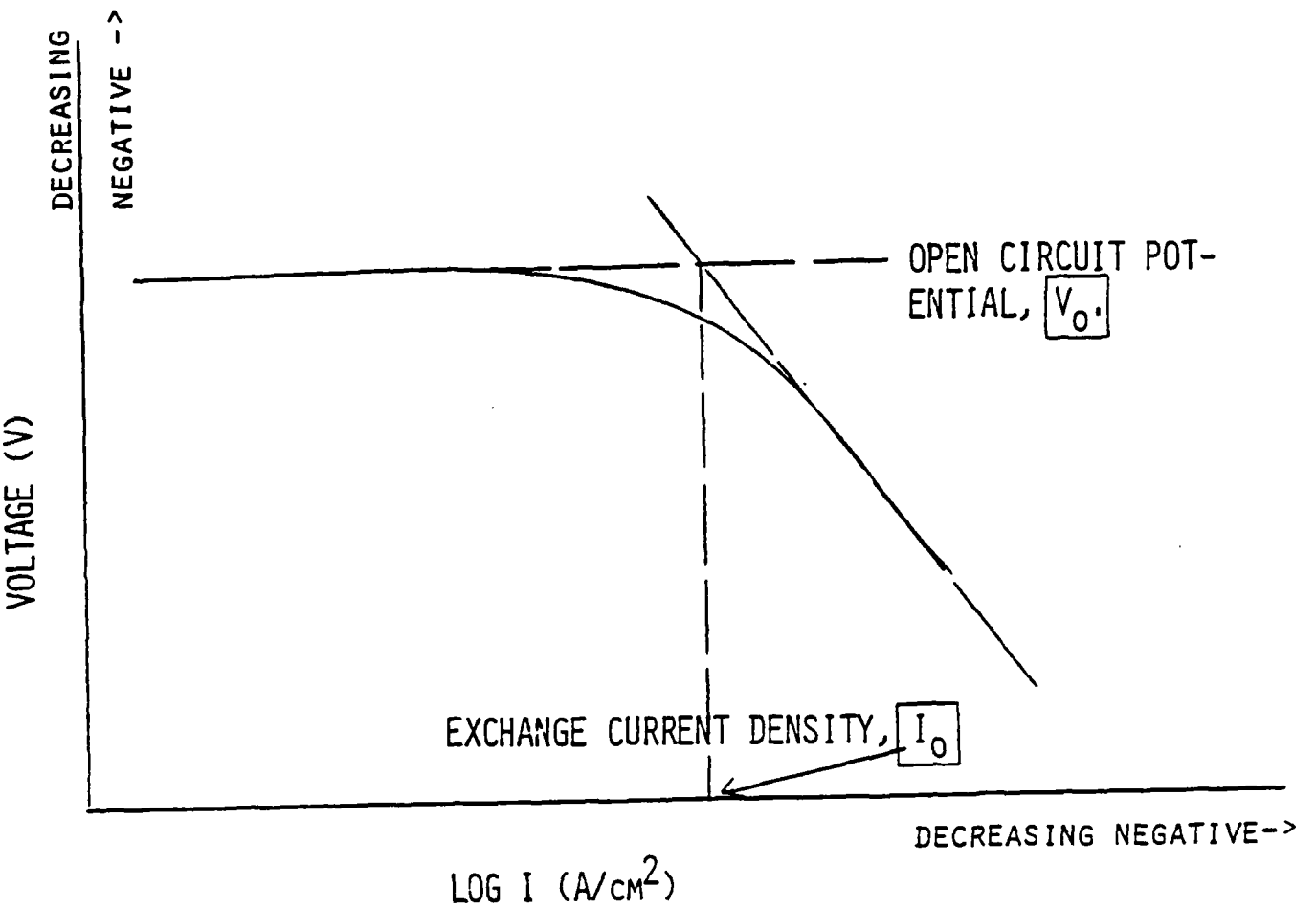
DECREASING
NEGATIVE ->
VOLTAGE (V)
OPEN CIRCUIT POTENTIAL, V_o.
EXCHANGE CURRENT DENSITY, I_o
DECREASING NEGATIVE->
LOG I (A/cm^2)

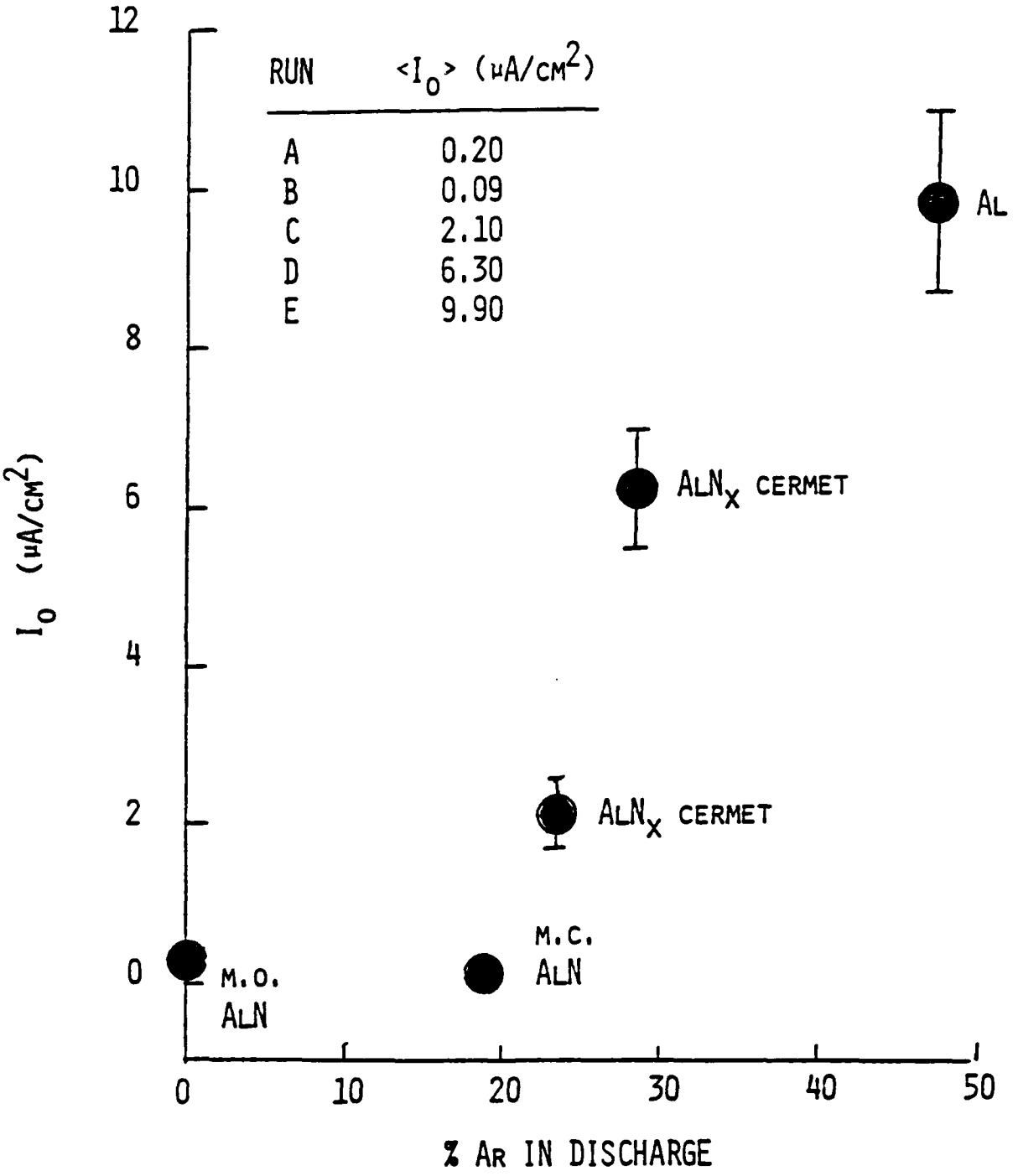
RUN
<I0> (μA/cm2)
A
0.20
B
0.09
C
2.10
D
6.30
E
9.90
AL
ALNx CERMET
ALNx CERMET
M.C. ALN
M.O. ALN
I0 (μA/cm2)
% AR IN DISCHARGE
0
2
4
6
8
10
12
0
10
20
30
40
50

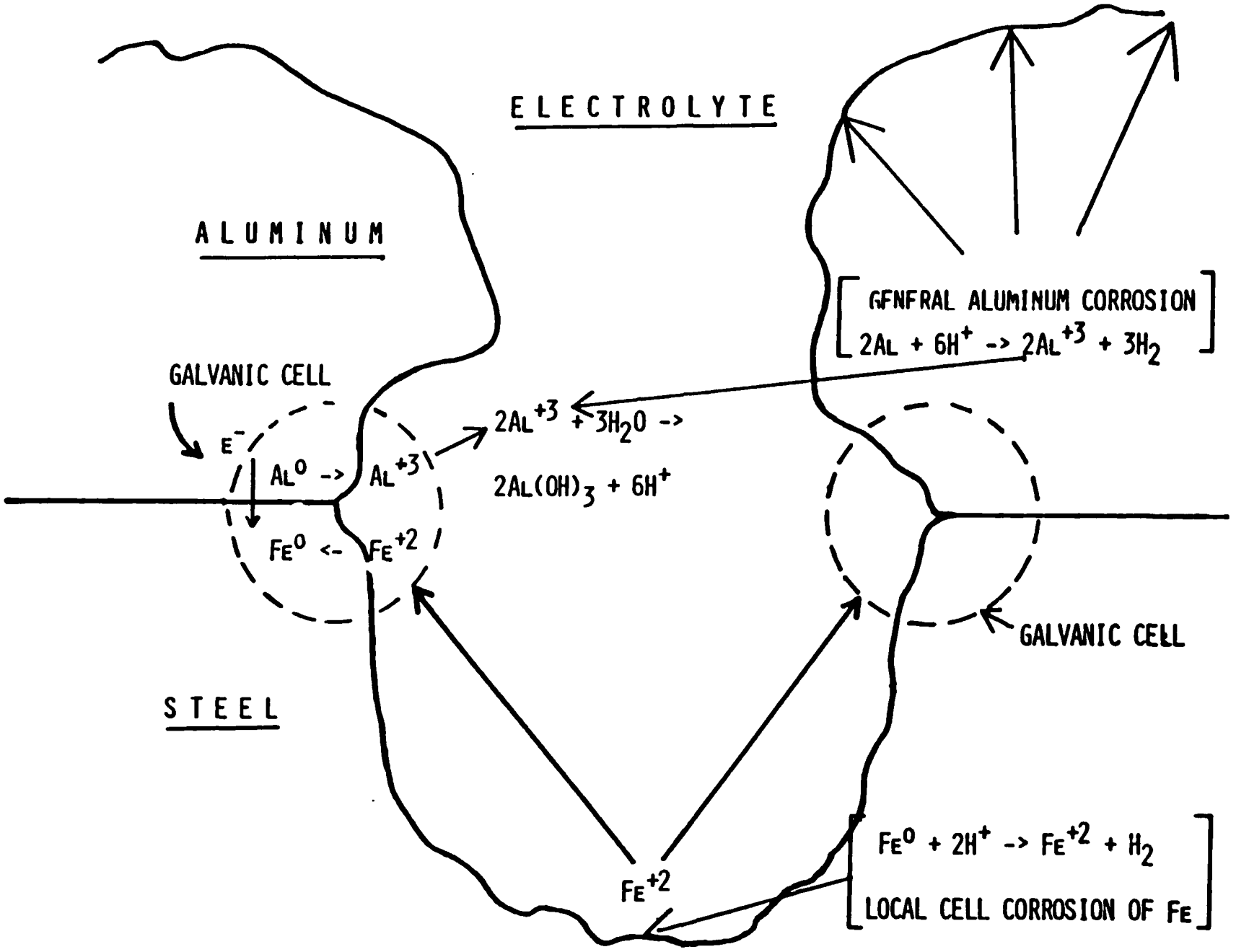
ELECTROLYTE
ALUMINUM
GENERAL ALUMINUM CORROSION
2AL + 6H+ -> 2AL+3 + 3H2
GALVANIC CELL
E-
AL0 -> AL+3
2AL+3 + 3H2O ->
2AL(OH)3 + 6H+
FE0 <- FE+2
GALVANIC CELL
STEEL
FE+2
FE0 + 2H+ -> FE+2 + H2
LOCAL CELL CORROSION OF FE

APPENDIX D

CHARACTERIZATION OF SPUTTER DEPOSITED Al-NITRIDE AND Al-OXIDE BY X-RAY PHOTOELECTRON LOSS SPECTROSCOPY

CHARACTERIZATION OF SPUTTER DEPOSITED Al-NITRIDE AND Al-OXIDE BY X-RAY PHOTOELECTRON LOSS SPECTROSCOPY

CHARLENE J. G. KUBIAK,* CAROLYN RUBIN AITA,* NGOC C. TRAN,** AND TERY L. BARR*
* Materials Department and the Laboratory for Surface Studies
University of Wisconsin-Milwaukee, P. O. Box 784, Milwaukee, WI 53201
**Materials Science Center
University of Wisconsin-Madison, Madison, WI 53706

ABSTRACT

The results of an x-ray photoelectron loss spectroscopy (XPLS) study of several wide band gap aluminum compounds are presented here. XPLS is a new application of x-ray photoelectron spectroscopy involving the determination of the energy separation, ΔE, between a particular core photoelectron peak and its principal loss peak. The materials investigated here are sputter deposited thin film Al-nitride and oxide, and bulk single crystal α-alumina. It is not possible to distinguish between these materials on the basis of the chemical shift in the binding energy of the Al2p and Al2s photoelectrons (Siegbahn shift). The results show that XPLS can be used to distinguish between these materials. ΔE in Al-oxides and nitride differs by several eV and is independent of sample charging. Comparison with ΔE calculated using a free electron gas model is made and related to the plasmon nature of ΔE.

INTRODUCTION

Thin films of Al-nitride can be grown near room temperature by reactive sputter deposition. However, oxygen-bearing contaminants in the sputtering discharge seriously affect film crystallinity and optical behavior [1]. Sometimes an oxide [1] or oxynitride [2] second phase is formed. It is difficult to distinguish between Al-nitride and Al-oxide using traditional x-ray photoelectron spectroscopy on the basis of the chemical shift in the Al core electron binding energy because:

1. The Al2p and Al2s electron binding energy for several Al-oxide polymorphs overlap that for Al-nitride.
2. The apparent shift in binding energy due to sample charging is usually greater than the Siegbahn chemical shift. In an attempt to correct for charging, referencing to the C1s XPS peak of adventitious carbon is frequently used. However, this technique is not always reliable. Furthermore, adventitious carbon may be removed upon depth profiling the sample by sputter etching.

In theory, it is possible to distinguish between Al-nitride and Al-oxide on the basis of the existence of an N1s spectrum and the absence of an O1s spectrum different from that for O physisorbed on AlN. However, all three elements are present in many technologically interesting systems and measurement of the O1s binding energy encounters the same problems mentioned above with respect to the Al2p and Al2s photoelectron spectra.

The loss peak is generated by the inelastic interaction of the ejected core photoelectron or its corresponding hole with the sea of valence band electrons [3-5]. For the case of harmonic oscillations of the valence band electrons in a simple metal (plasmons) in which there is no electron localization in the valence band or core electron polarization, ΔE is given by the free electron gas expression [6]:

$$\Delta E = \hbar [4\pi e^2 n/m]^{1/2} \qquad (1)$$

where e is the charge on an electron, n is the density of valence band electrons, and m is the mass of an electron.

Even for wide band gap materials, loss peaks represent collective transitions if there is sufficient valence band electron delocalization [7,8]. However, part of the valence band electron density may behave in a non-collective manner. These localized states may perturb ΔE above or below the free electron gas value, and cause dispersion in the values of ΔE associated with photoelectrons originating from different energy states [4,5].

XPLS is easy to instrument. The technique can be carried out on a conventional ESCA system. However, a critical difference between XPLS and other more difficult-to-instrument electron energy loss spectroscopies, EELS for example, is that in XPLS, the measurement is made in the relaxed hole ion system, the final state. Theoretical arguments show that for many materials systems, the value of ΔE is independent of relaxation effects [3-5]. If this is the case, then XPLS yields information about the initial chemical state of the material.

With respect to Al-N and Al-O compounds, the purpose of the present study is to answer three questions:

1. Can these materials be distinguished on the basis of different values of ΔE?
2. Is ΔE independent of sample charging?
3. Do loss features represent collective transitions of the valence band electrons? To determine this, the values of ΔE obtained by XPLS will be compared with theoretical calculations using a free electron gas model.

EXPERIMENTAL PROCEDURE

A Perkin-Elmer Physical Electronics Model 548 AES/ESCA system was used to take high resolution spectra of the Al2p and Al2s principal XPS peaks using an analyzer energy of 50 eV, and their companion loss peaks using an analyzer energy of 100 eV. Mg $k\alpha$ x-ray radiation was used. A gold standard was used to calibrate the position of the $Au4f_{7/2}$ peak at 83.8 eV, measured to an accuracy of ±0.2 eV. Depth profiling of the samples for times up to 300 sec using a 100 eV, 10 ma, Ar^+ ion beam was carried out. The sputtering rate for the materials examined here was estimated to be between 0.3 and 0.5 Å/sec. Depth profiling is used to obtain chemical information from layers below the film surface. The reader is reminded, however, that sputter etching may damage the film surface, and produce artifacts not representative of film chemistry [9].

The following materials were examined:

1. Bulk single crystal (0001)-cut α-alumina. Data were collected from three samples.
2. Thin film alumina grown by sputter deposition on water-cooled Si-(111) substrates using an Al target and an rf-excited oxygen discharge operated at 600 W rf forward power. Data were collected from three samples. The films showed no x-ray diffraction peaks, indicating that there was no long range crystallographic order. These films are referred to here as "amorphous" or "a-alumina".
3. Thin film Al-nitride grown by reactive sputter deposition on water cooled Si-(111) substrates using an Al target and an rf-excited nitrogen discharge operated at rf forward power levels from 300 to 800 W. The films were found to be Al-rich [1]. Partial oxidation of the excess Al occurred upon exposure to air. The single x-ray diffraction peak from the films was attributable to the (0001) planes of the wurtzite-type AlN lattice. No N-O bonding [2] was detected by XPS.

The chemical composition of the Al-nitride films, obtained from the relative intensity of the Al2p, N1s, and O1s XPS peaks multiplied by the

TABLE I: Change in Chemistry of Al-Nitride Films with Deposition Discharge Power, Depth Profiling, and Room Temperature Aging

Power (W)	Al:N:O Atomic Ratio 0 sec etch	5 sec etch	120 sec etch
300	*10:6:4	10:5:5	10:6:-
	+10:4:13	10:4:11	10:5:5
500	+10:6:10	10:6:7	10:7:7
700	+10:7:9	10:6:9	10:8:8
800	*10:8:2	-	-
	+10:7:9	10:9:6	-

Data taken (*) 5 days and (+) 350 days after deposition.

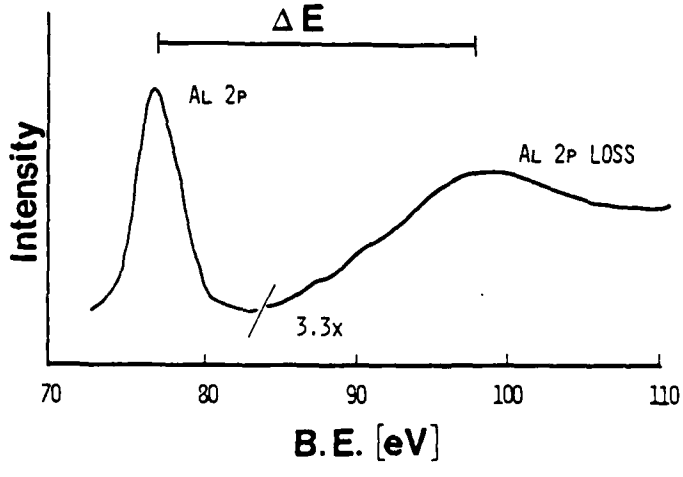

Fig. 1: A typical XPLS spectrum, associated with the Al2p photoelectron in Al-nitride. ΔE is the separation between the principal Al2p photoelectron peak and its largest companion bulk loss peak.

appropriate sensitivity factor [10] is recorded in Table I. To observe the effects of room temperature aging [1], data was taken from films 5 and 350 days after deposition. It should be noted that although the O content in the films increases in time, the N/Al ratio does not change significantly. This result indicates that O is not replacing N in the films during the aging process.

RESULTS

A typical loss spectrum, in this case associated with the Al2p photoelectron in Al-nitride, is shown in Fig. 1. To compare the value of ΔE generated by photoelectrons from different energy states in the same material, ΔE(Al2p) and ΔE(Al2s) are shown as a function of the sputter etch time for individual Al-nitride films in Fig. 2, and for α-alumina and a-alumina in Fig. 3.

It can be seen from Fig. 2 that within experimental error (±0.4 eV), the value of ΔE is independent of whether the loss spectrum was induced by an Al2p or Al2s electron. In contrast, there is pronounced dispersion in ΔE associated with Al2p and Al2s photoelectrons in α-alumina, as can be seen from Fig. 3a. In the case of a-alumina (Fig. 3b), the data presented here is inconclusive with respect to ΔE(Al2p)-ΔE(Al2s) dispersion. Although the values for ΔE(Al2p) consistently lie above those for ΔE(Al2s), they are still within experimental error of each other.

To compare the behavior of ΔE associated with photoelectrons from the same energy state in Al-nitride and oxide, ΔE(Al2p) and ΔE(Al2s) are shown in Figs. 4a and 4b versus sputter etching time for all samples. It can be seen that nitrides and oxides are clearly distinguishable (by several eV) on the basis of both ΔE(Al2p) and ΔE(Al2s). However, Al-nitride films having different amounts of incorporated O cannot be differentiated on the basis of ΔE.

In α-alumina, there is no systematic change greater than experimental uncertainty in either ΔE(Al2p) or ΔE(Al2s) with sputter etching. However, in a-alumina and Al-nitride, there is a small decrease in ΔE with sputter etching. The reason for this decrease is, at present, not clear. One possible explanation is based on the relative stability of octahedral (more stable) and tetrahedral (less stable) bonds in binary systems which contain a common metal cation. In α-alumina, Al is in 6-fold coordination with O, with Al occupying 2/3 of the octahedral interstices in the close-packed hexagonal O sublattice [11]. In Al-nitride, Al is in 4-fold coordination with N, with Al occupying 1/2 of the tetrahedral interstices in the close-packed hexagonal N sublattice [12]. The average coordination number of Al with O in a-alumina lies between 4 and 6 [13-15]. A chemical etching study [16], however, showed that in order to relieve surface strain (to decrease the number of dangling bonds), a larger number of Al atoms are in 6-fold coordination at the surface of the material than in the interior. It is possible that this change in Al coordination number in a-alumina causes the abrupt decrease in ΔE from a value identical with α-alumina at the film surface to a lower value after a 5 sec sputter etch.

Figure 5 shows ΔE(Al2p) versus the Al2p principal XPS peak energy in all samples in which charge referencing to the C1s peak at 284.6 eV was possible. It can be seen that although the Al2p principal peak energy overlaps for the Al-nitride and oxides studied here, ΔE(Al2p) for each set of compounds is clearly distinguishable.

To demonstrate that ΔE is independent of sample charging, Fig. 6 shows ΔE(Al2p) versus the Al2p principal peak energy before correction for charging was made. It can also be seen from Fig. 6 that the shift in

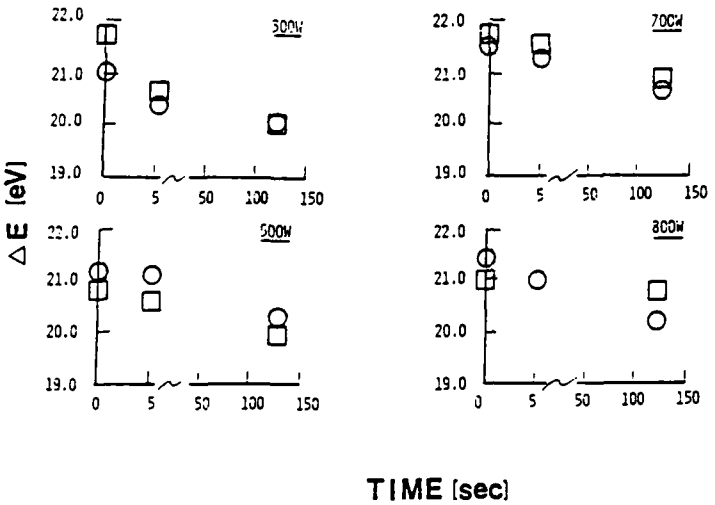

Fig. 2: ΔE as a function of sputter etching time for sputter deposited Al-nitride films. Squares represent ΔE(Al2s), circles represent ΔE(Al2p).

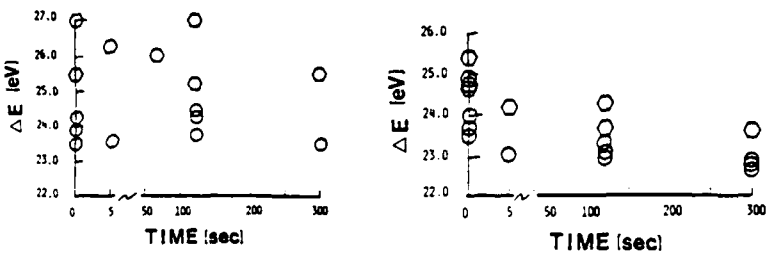

Fig. 3: ΔE as a function of sputter etching time for (a) single crystal α-alumina, (b) sputter deposited a-alumina. Circles represent ΔE(Al2s), hexagons represent ΔE(Al2p).

384

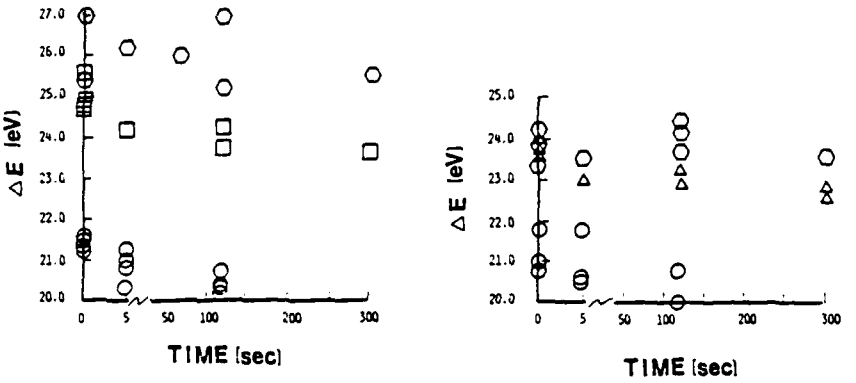

Fig. 4: (a) ΔE(Al2p) and (b) ΔE(Al2s) as a function of sputter etching time for all samples. (Hexagons-α-alumina; triangles and squares-a-alumina; circles-Al-nitride).

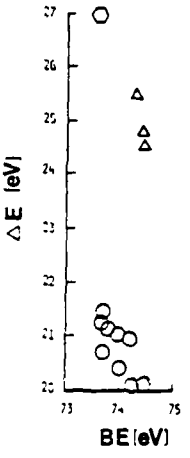

Fig. 5: ΔE versus Al2p photoelectron peak after charge referencing. (Hexagons-α-alumina; triangles-a-alumina; circles-Al-nitride.)

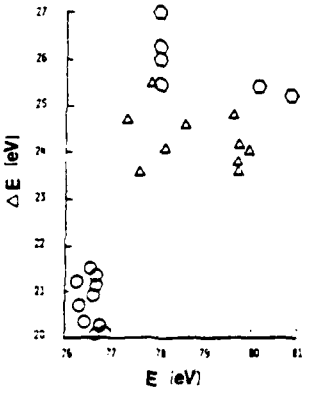

Fig. 6: ΔE versus Al2p photoelectron peak before charge referencing to C. (Hexagons-α-alumina; triangles-a-alumina; circles-Al-nitride.)

the Al2p principal peak energy caused by sample charging is on the order of several eV.

DISCUSSION AND CONCLUSIONS

From the data presented above, it can be concluded that the separation of the first loss peak from its principal XPS peak for Al2p and Al2s photoelectrons differs in Al-oxides and nitrides by several eV (Figs. 2 to 4). These materials cannot be distinguished on the basis of the measured principal XPS peak energy (Fig. 5). Furthermore, ΔE is independent of sample charging (Fig. 6). For these reasons, XPLS is a technologically useful characterization technique.

The question which remains to be addressed concerns the physical basis of the loss spectra in these wide band gap materials. In metallic Al, loss features can be attributed to plasma oscillations of the valence electrons. The value of ΔE(Al2p) obtained by XPLS on metallic Al is 15.8 eV [5] in agreement with the value calculated using Eq. (1) for a free electron gas (FEG) [17].

Table II summarizes the range of XPLS results obtained here, as well as the calculated value of ΔE using the FEG model. In the case of Al-nitride, it can be seen from Table II that the FEG calculation [18] yields a value within experimental error of the values for ΔE obtained by XPLS. In addition, there is no dispersion in the values of ΔE(Al2p) and ΔE(Al2s). It is therefore suggested that the loss features in the XPLS spectrum of Al-nitride are plasmon in origin and ΔE is consistent with the value calculated using a FEG model.

With respect to the aluminas, the situation is more complex. In α-alumina there is a large dispersion in ΔE(Al2p) and ΔE(Al2s). Loss features in this material are therefore not entirely plasmon in nature. The values of ΔE(Al2p) do not agree with FEG calculations using either 18 or 24 valence electrons/Al_2O_3 molecule [14,15]. Agreement between ΔE(Al2s) and FEG calculations using 18 valence electrons/Al_2O_3 molecule may be coincidental.

TABLE II: Comparison of ΔE Obtained by XPLS with Free Electron Gas Calculations

Material	ΔE, XPLS (eV)[+]	ΔE, FEG (eV)
α-alumina	Al2p: 25.2-27.0 Al2s: 23.0-24.5	24.0,* 27.9**
a-alumina	Al2p: 23.6-25.5 Al2s: 22.5-24.0	20.2,* 23.4**
Al-nitride	Al2p: 20.2-21.8 Al2s: 19.8-21.8	20.0

[+] Range of all data; ±0.4 eV experimental error.
* Assuming 18 valence electrons/Al_2O_3 molecule, O2s e^- not counted [14,15].
** Assuming 24 valence electrons/Al_2O_3 molecule, O2s e^- counted [14,15].

In α-alumina, ΔE(Al2p)-ΔE(Al2s) dispersion has not been firmly established from the results of this study. Free electron gas calculations using 24 valence electrons/Al_2O_3 molecule yield a value within experimental error of the lower end of the ΔE(Al2p) range and within the ΔE(Al2s) range of values obtained by XPLS. As in the case of α-alumina, however, this agreement may be coincidental. We cannot therefore conclude that a FEG model accurately describes the loss features in aluminas. However, it is suggested that Eq. (1) be taken as the first term in a series in which successive terms account for perturbations due to non-collective behavior of part of the valence band electron population [5]. Future work will consider modification of the free electron gas model in this manner for the aluminas.

ACKNOWLEDGEMENTS: This work was supported under U.S. Army Research Office Grant No. DAAG29-84-0126. We thank M.G. Lagally for making the Auger/ESCA Laboratory at UW-Madison available for our use.

REFERENCES

1. C. J. G. Kubiak, C. R. Aita, F. S. Hickernell, and S. J. Joseph, Proc. Mater. Res. Soc. 47, 75 (1985).

2. J. A. Kovacich, J. Kasperkiewicz, D. Lichtman, and C. R. Aita, J. Appl. Phys. 55, 2935 (1984).

3. J. W. Gadzuk, J. Electron Spec. Rel. Phenom. 11, 335 (1977).

4. T. L. Barr, Appl. Sur. Sci. 10, 1 (1983).

5. T. L. Barr, B. Kramer, S. I. Shah, M. Ray, and J. E. Greene, Proc. Mat. Res. Soc. 47, 205 (1985).

6. D. Pines and D. Bohm, Phys. Rev. 85, 338 (1952).

7. D. Pines, Rev. Mod. Phys. 28, 184 (1956).

8. P. Norieres and D. Pines, Phys. Rev. 109, 741 (1958).

9. D. G. Welkie and M. G. Lagally, J. Vac. Sci. Technol 16, 784 (1979).

10. D. Briggs and M. P. Seah, Practical Surface Analysis by Auger and Photoelectron Spectroscopy (Wiley, New York, 1983) pp. 511-514.

11. A. F. Wells, Structural Inorganic Chemistry (Calredon, London, 1950) pp. 379-386.

12. Ibid. pp. 49, 462.

13. J. A. Thornton and J. Chin, Ceramic Bull. 56, 504 (1977).

14. W. Tews and R. Grundler, phys. stat. sol. (b), 109, 255 (1982).

15. W. Tews and R. Zimmermann, phys. stat. sol. (b) 110, 479 (1982).

16. R. G. Frieser, J. Electrochem. Soc. 113, 357 (1966).

17. O. Klemperer and J. P. G. Shepherd, Adv. Phys. 12, 355 (1963).

18. C. R. Aita, unpublished. (6 valence electrons/AlN molecule and 6 molecules/unit cell are assumed.)

APPENDIX E

OPTICAL BEHAVIOR OF SPUTTER DEPOSITED VANADIUM PENTOXIDE

Optical behavior of sputter-deposited vanadium pentoxide

Carolyn Rubin Ai Ying-Li Liu, Mei Lee Kao, and Steven D. Hansen[a)]
Materials Department and the Laboratory for Surface Studies, University of Wisconsin-Milwaukee, P. O. Box 784, Milwaukee, Wisconsin 53201

(Received 27 January 1986; accepted for publication 27 March 1986)

A series of V–O alloy films were sputter deposited on glass substrates using a vanadium target and rf-excited Ar/O_2 discharges containing 2%–8% O_2. On the basis of x-ray results, the films were nominally identified as vanadium pentoxide. Optical transmission and reflection characteristics were measured by double-beam spectrophotometry in the 390- to 700-nm-wavelength region. From these measurements, the absorption coefficient α was determined as a function of the incident photon energy $h\nu$. The absorption edge of all films showed two distinct regions of behavior: a high photon energy region in which α varied linearly with $(h\nu)^2$ and a low-energy tail. The behavior of α is discussed in terms of the structural and electronic changes in the films due to nonstoichiometry and compared to results obtained for single crystal V_2O_5.

I. INTRODUCTION

A recent study[1] shows that vanadium pentoxide undergoes a semiconductor–to–metal phase transition[2–5] at 257 ± 5 °C. A large change in electrical behavior accompanies the phase change and thermally activated electrical switches have been fabricated from this material. Since optical and electrical behavior are coupled, vanadium pentoxide may have potential use in optical switches and write-erase media as well.

Vanadium pentoxide is especially interesting in thin-film form because of the possibility of integration into microelectronics circuitry. Thin films have been produced by thermal evaporation[6] and sputter deposition using a V_2O_5 target.[7] In our laboratory, films which are nominally vanadium pentoxide were grown by reactive sputter deposition using a V target and Ar/O_2 discharges.[8] Based on growth rate results and *in situ* discharge diagnostics using optical emission spectroscopy, we concluded that an oxide layer was formed at the target surface once the O_2 content of the sputtering gas reached a critical value. This phenomenon has been observed during sputter deposition of other oxide systems as well.[9]

In the present study, we examine the room-temperature optical behavior of V–O alloy films deposited in Ar/O_2 mixtures containing up to the critical O_2 value necessary for the formation of an oxide layer at the target. The term "alloy" used here means "a mixture of V and O intimately united". Double-beam spectrophotometry was used to measure the transmission and reflection characteristics in the 390 nm (3.18 eV) to 700 nm (1.77 eV) wavelength region. This spectral region was chosen because it encompasses the fundamental optical absorption edge of bulk V_2O_5.[10–13] From measurements of reflectance and transmittance, the optical absorption coefficient was calculated as a function of incident photon energy.

The purpose of this study is twofold. First, if sputter-deposited films are to be used for optical switching devices, the optical behavior of the material in its preswitched, or initial state must be well characterized. Second, optical absorption edge characteristics yield information about the fundamental nature of the films (chemistry, atomic order) which can then be related to processing parameters and discharge characteristics. In the present study, supplementary x-ray diffraction was carried out, which, when coupled with absorption edge characteristics, gives insight into film structure.

The evolution of structure in films grown by reactive sputter deposition is governed by kinetics. For this reason, high melting point compounds can be grown on near-room-temperature substrates. Metastable alloys can be synthesized with a wide range of properties and unusual behavior not attainable in bulk material. It is essential to understand the steps which lead to the production of a particular alloy or compound if the process is to be reproducible and transferable from apparatus to apparatus.

II. EXPERIMENTAL PROCEDURE

A. Film deposition

A hot-oil diffusion pumped rf-diode apparatus was used for film preparation. The substrates were laboratory glass slides placed in thermal contact with the water-cooled Cu anode. A 7.5 cm, 99.7% V target was bonded (MRC Permabond) to the water-cooled stainless-steel cathode and sputtered in Ar/O_2 discharges containing from 2% to 8% O_2. This range was chosen because 2% O_2/Ar is the smallest ratio that could be reproducibly attained and 8% O_2/Ar is the ratio at which the surface of the target becomes fully oxidized (with all other experimental parameters used here held constant). The deposition parameters used to obtain each sample are summarized in Table I. Further details of the relationship of deposition parameters to discharge characteristics are given in Ref. 8.

B. Optical behavior

A Perkin-Elmer Model 330 UV-Visible-IR double beam spectrophotometer with a specular reflection attachment was used to measure the transmission and reflection of near-normal incidence radiation in the 390–700-nm-wavelength

[a)] Permanent address: The General Electric Company, P. O. Box 414, Milwaukee, Wisconsin 53201.

 0021-8979/86/140749-05$02.40

TABLE I. Parameters used to deposit vanadium pentoxide films.

Sample	Gas % O_2	Target voltage[a] (kV $p-p$)	Growth rate[b] (Å/min)
A	2	2.20	30
B	4	2.20	24
C	6	2.20	18
D	8	2.20	20

The following deposition parameters were held fixed; 300 W rf forward power, 0.01 Torr total gas pressure, 4 cm anode-cathode spacing. For presputter conditions see Ref. 8.

[a] ± 0.05 kV.

[b] ± 1%.

range. All measurements were made in laboratory air at room temperature.

In transmission mode, the film + substrate composite was placed in the path of the sample beam and a bare substrate was placed in the path of the reference beam. In this manner, absorption by the substrate, although small (10%) throughout the wavelength region under consideration, was subtracted from the data. The output data were in the form of $\log_{10}(I_0/I)$ versus the wavelength of the incident radiation. I_0 is the intensity of incident radiation and I is the intensity of radiation which exits the film.

In reflection mode, no sample was placed in the path of the reference beam. Instead, the instrument was calibrated over the wavelength range under consideration using a protected Al mirror standard.

Reflectance (R), transmittance (T), and absorbance (A) are related to each other in the following manner:

$$A + T + R = 1. \tag{1}$$

Absorbance is defined in terms of the absorption coefficient α.[14] For a sample of thickness x,

$$\alpha x = \ln(I_0/I), \tag{2}$$

and

$$T = [(1-R)^2 \exp(-\alpha x)]/[1 - R^2 \exp(-2\alpha x)]. \tag{3}$$

Equation (3) is used here to calculate α in the vicinity of the fundamental optical absorption edge, when $R^2 \exp(-2\alpha x) \ll 1$. Based on experimental data for the worst case, the term $R^2 \exp(-2\alpha x)$ is less than 3% of unity.

C. Crystallography and thickness measurements

The bulk semiconducting phase of vanadium pentoxide is a layered structure. The orthorhombic bimolecular unit cell has dimensions $a = 11.519$ Å, $b = 4.373$ Å, and $c = 3.564$ Å.[15] The multicell structure consists of trigonal bipyramids joined at shared edges to form zig-zag chains along the c axis. The chains are cross-linked with O_3 groups to form layers in the (010) plane. Translation along the b axis shows the structure to consist of alternating layers of V + O atoms and O alone. These layers can be seen in the projection of the (001) plane shown in Fig. 1. The distance between equivalent layers is equal to the (010) interplanar spacing. Detailed representations of the V_2O_5 lattice are given in Refs. 16–18.

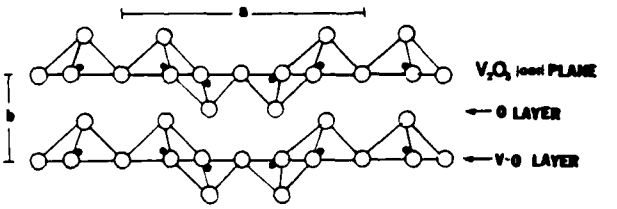

FIG. 1. A projection of the (001) plane of the orthorhombic V_2O_5 lattice. White circles indicate O atoms, black circles indicate V atoms (after Ref. 18).

Bragg–Brentano (double angle) x-ray diffraction was used to determine lattice planes oriented parallel to the substrate. Diffraction patterns were obtained using 1.5428-Å wavelength unresolved Cu$K\alpha$ radiation. The sample was rotated through an angle θ while simultaneously rotating the detector through an angle 2θ. The diffractometer was calibrated using an NBS Si powder standard. Precise peak position was measured to an accuracy of ± 0.02°. The full width at one-half the maximum intensity was found to be 0.18° for the Si (111) peak at $2\theta = 28.47°$. This value represents peak broadening caused solely by instrument effects.

Film thickness was determined using a profilometer to measure the height of a step produced by masking a region of the substrate during deposition. The instrument-related uncertainty in each measurement is ± 20 Å. The thickness of each sample is recorded in Table II.

III. RESULTS

Optical behavior: In terms of visual appearance, all films are transparent. Samples A and B are green. Samples C and D are honey yellow, the color of bulk single crystal V_2O_5 (Ref. 12).

The absorption coefficient calculated using Eq. (3) is shown as a function of the incident photon energy in Fig. 2. Sample D has a featureless absorption edge. In the high-energy region of the edge ($\alpha > 3 \times 10^4$ cm^{-1}, $h\nu > 2.48$ eV), α varies linearly with $(h\nu)^2$, as shown in Fig. 3. In the low-energy region of the edge, α has an exponential dependence on $h\nu$.

In the high-energy region of the absorption edge, α for samples B and C coincides with that for sample D. However, both samples B and C have low-energy tails in which α does not vary exponentially with $h\nu$. The absorption edge of sample A also has two distinct regions of behavior. For photon energy $> \sim 2.5$ eV, α varies linearly with $(h\nu)$,[2] but increases less rapidly than in the other samples. The low-ener-

TABLE II. Thickness and crystallographic data for vanadium pentoxide films.

Sample	Gas % O_2	Thickness (10^3 Å)	b[a] (Å)	FWHM[b] (deg)	$\Delta b \times 10^{-3}$
A	2	5.4	4.362	0.35	− 2.5
B	4	4.3	4.362	0.30	− 2.5
C	6	3.2	4.366	0.29	− 1.6
D	8	3.6	4.373	0.30	0

[a] ± 0.005 Å uncertainty in each measurement; $b_0 = 4.373$ Å.

[b] ± 0.04° uncertainty in each measurement.

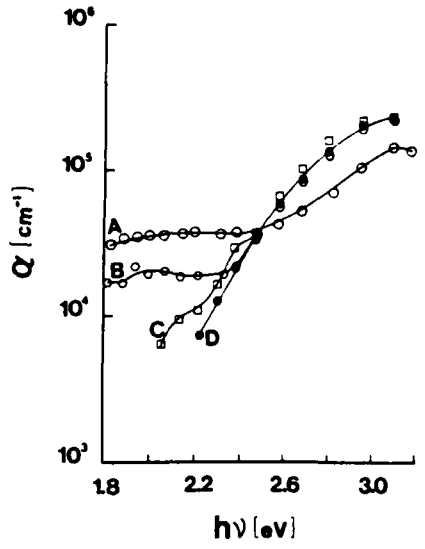

FIG. 2. The absorption coefficient α as a function of the incident photon energy $h\nu$ for sputter-deposited vanadium pentoxide. The sputtering gas O_2 content used to grow each film is as follows: sample A, 2%; sample B, 4%; sample C, 6%; sample D, 8%.

gy region of the edge in sample A is a plateau of nearly constant α.

Crystallography: All films show two x-ray diffraction peaks. These peaks are attributable to (010) and (020) orthorhombic V_2O_5 lattice planes. The film structure is such that the b axis in all crystallites is oriented perpendicular to the substrate. (010)-type planes, which consist of alternating layers of V + O and O atoms, lie parallel to the substrate. The average (010) interplanar spacing increases with increasing sputtering gas O_2 content, as recorded in Table II.

The difference in (010) interplanar spacing between these samples and bulk unstressed V_2O_5 is given by the relationship:

$$\Delta b = (b - b_0)/b_0, \tag{4}$$

where b_0 is the (010) interplanar spacing for bulk V_2O_5. Δb changes from -2.5×10^{-3} to zero as the sputtering gas O_2 content is increased from 2% to 8%. The expression "strain" is not used here to describe Δb because the measured (010) interplanar spacing may be that which results in an unstrained lattice for a particular nonstoichiometry.

The diffraction peak width at one-half the maximum intensity (FWHM) is recorded in Table II. Within experimental uncertainty, the FWHM is the same for all samples and greater than expected from instrumental effects alone. In general, materials parameters which contribute to peak broadening are small crystallite size, stacking faults, and nonuniform strain (distribution of lattice spacings about the average value). Two orders of two diffraction peaks are required to realistically estimate the individual contribution of each factor.[19]

IV. DISCUSSION

From the data presented above, it can be seen that the optical absorption edge of all samples shows two distinct regions of behavior: a high photon energy region in which α varies linearly with $(h\nu)^2$ and a low-energy tail. In samples B, C, and D, the transition between these regions occurs abruptly at 2.48 eV, indicating that there is a change in the type of optical transition at this photon energy. The high photon energy region is associated with valence-to-conduction-band transitions and the low-energy tail is associated with transitions involving impurity states within the energy band gap. Investigators[12] working with single-crystal V_2O_5 report a change in the slope of α vs $h\nu$ at $\sim$2.45 eV (Fig. 4), in reasonable agreement with the results obtained here.

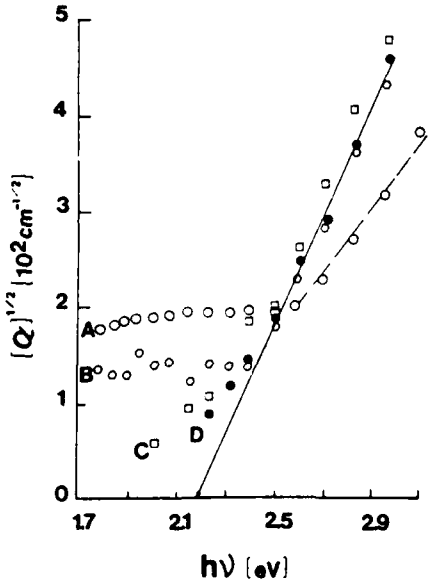

FIG. 3. The square root of the absorption coefficient as a function of the incident photon energy for sputter-deposited vanadium pentoxide. The solid line is a best fit of the data for sample D to Eq. (5). The dashed line is a best fit of the data for sample A to Eq. (5).

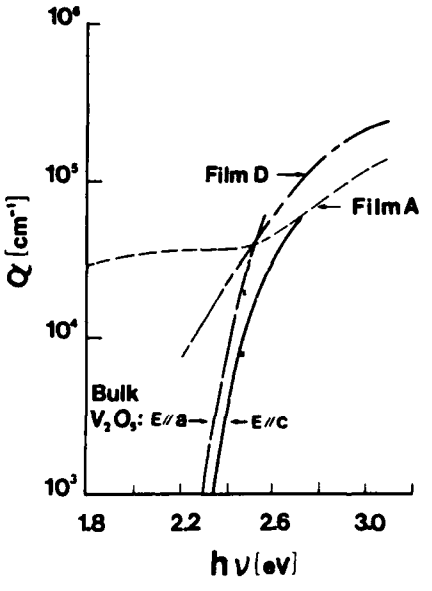

FIG. 4. The absorption coefficient as a function of the incident photon energy for bulk single-crystal V_2O_5. The data were taken from Ref. 11. Measurements were made with the electric field vector E in the (010) plane parallel to either the a or c axis, as labeled. Crosses indicate a transition in α from an exponential to power dependence on $h\nu$. For comparison, the extremes in sputter-deposited film behavior obtained in this study are included.

However, the absorption edge of the films differs from that of bulk material in two respects: (1) the functional dependence of α on $h\nu$ in the high-energy region and (2) the prominence of the low-energy tail. Investigators of bulk V_2O_5 disagree about the functional dependence of α on $h\nu$. Working with single crystals, Kenny *et al.*[12] and Bodo and Hevesi[13] found α to vary linearly with $(h\nu)^{3/2}$. This dependence is characteristic of a forbidden direct transition across the band gap of a crystalline solid. Working with polycrystalline powder, Karvaly and Hevesi[11] found α to vary linearly with $(h\nu)^{1/2}$. This dependence is characteristic of an allowed direct transition across the band gap of a crystalline solid. In these studies, the room-temperature band gap was calculated by extrapolating α vs $(h\nu)^{3/2}$ or $(h\nu)^{1/2}$ to $\alpha = 0$. E_G was found to lie between 2.30 and 2.36 eV, depending on investigator and crystal anisotropy.

With respect to the films studied here, two types of band-to-band transitions in which α varies linearly with $(h\nu)^2$ are as follows.

(1) An allowed indirect transition in a crystalline solid[14]:

$$\alpha = A(h\nu - E_G)^2, \tag{5}$$

where A is a constant. Equation (6) is shown as a solid line in Fig. 3 for samples B, C, and D, with $E_G = 2.18$ eV, and a dashed line for sample A with $E_G = 1.95$ eV.

(2) A nondirect transition in a noncrystalline solid[20]:

$$(\alpha h\nu) = B(h\nu - E_0)^2. \tag{6}$$

E_0 is the optical band gap and B is a constant. Transitions across E_0 occur between extended states in the valence and conduction bands. A parabolic density of states for both bands is assumed. Electron momentum, however, need not be conserved during the transition. Figure 5 shows $(\alpha h\nu)^{1/2}$ as a function of $h\nu$ for all samples. The solid line represents the best fit through the data for sample D, which when extrapolated to $\alpha = 0$ yields $E_0 = 2.18$ eV. The dashed line represents the best fit for sample A, which yields $E_0 = 1.95$ eV at $\alpha = 0$.

In order for Eq. (6) to be applicable to our material, the films must have sufficient topological[21] disorder so that electron momentum need not be conserved during the transition.[20,22] All of the films have some degree of crystallinity perpendicular to the substrate plane (Table II). There is a repetition of successive V–O and O layers parallel to the substrate. However, the degree of randomness within the substrate plane (randomness in the orientation of the a and c axes from one crystallite to the next) is not known. The large FWHM of the (010) diffraction peak can be caused by microcrystallinity *parallel* to the substrate[23] as well as perpendicular. For this reason, the model which has traditionally been applied to a noncrystalline solid can also be considered here. This model is particularly satisfying because it involves a transition between parabolic bands, consistent with the results for single crystal V_2O_5 described above.

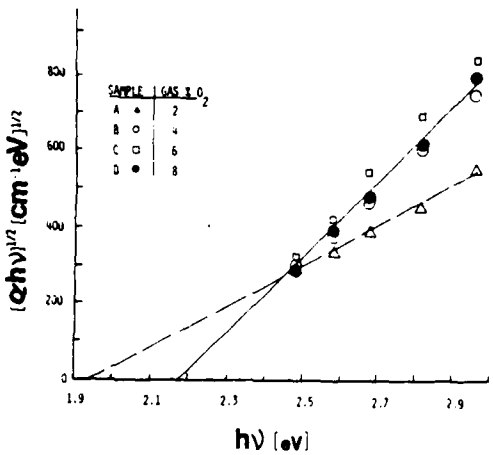

FIG. 5. $(\alpha h\nu)^{1/2}$ as a function of the incident photon energy for $h\nu > 2.48$ eV for sputter-deposited vanadium pentoxide. The solid line is a best fit of the data for sample D to Eq. (6). The dashed line is a best fit of the data for sample A to Eq. (6).

Gilles and Boesman[16] proposed a model describing the effect of increasing nonstoichiometry on the V_2O_5 structure which is useful for interpretation of our results. Based on an electron paramagnetic resonance study, the defect center of as-grown single crystal V_2O_5 was found to involve an O vacancy in the O layer between two V–O layers in (010)-type planes. Atomic order in V–O layers is not structurally disturbed by a small amount of O vacancies in adjacent O layers. However, when a sufficient number of O atoms are removed from an O layer, adjacent V–O layers collapse, giving rise to V_6O_{13}-type stacking faults. V–O coordination in the faulted areas changes from distorted octahedral (V_2O_5) to tetrahedral (V_6O_{13}).

With respect to the films studied here, consideration of the model discussed above indicates that V–O coordination controls the behavior of the absorption edge in the high photon energy region. Short-range order is known to control absorption behavior for $h\nu > E_G$ in other materials with equivalent local cation–anion bonding but different long-range order.[22] Decreasing sputtering gas O_2 content from 8% to 2% increases nonstoichiometry, a gross manifestation of which is the change in color from yellow to green. Initially, the effect of nonstoichiometry is to contract the (010) interplanar spacing as O vacancies are created, although V–O coordination does not change. Hence, samples B, C, and D have different (010) interplanar spacing although identical absorption edges for $h\nu > 2.48$ eV. As nonstoichiometry increases further, the stacking faults that develop give rise to a change in V–O coordination and to a change in the shape of high-photon-energy region of the absorption edge (sample A).

The low-energy tail appears to be sensitive to electronic defects arising from nonstoichiometry. The exponential tail in sample D is characteristic of a continuum of states adjacent to either the conduction- or valence-band edge and extending into the gap.[14,20,22,24,25] The exponential dependence of the tail, $d[\ln \alpha(h\nu)]/d(h\nu)$, is equal to $(2\ kT)^{-1}$ for single crystal V_2O_5 (Ref. 12) and $(6.4kT)$ for sample D. Broadening of an exponential tail in both crystalline and noncrystalline semiconductors has been associated with impurity concentration, in particular with impurities which lead to charged defects.[20,24,25]

As the sputtering gas O_2 content is decreased from 8% (sample D) to 6% (sample C), the low-energy tail further

broadens and develops two small bands at 2.14 and 2.38 eV. These features are related to states within the band gap which do not form a continuum of states adjacent to either the valence- or conduction-band edge. Hence the exponential shape of the tail is lost.[24] As the sputtering gas O_2 content is further decreased (samples A and B), the low-energy tail flattens out to a plateau of nearly constant α.

Chemical analysis by Auger and x-ray photoelectron spectroscopy was carried out to determine if elemental impurities were present.[26] No elemental impurities were found. We therefore conclude that enhanced absorption in the low-energy tail is associated with self-impurities. In order to electrically compensate for each O vacancy, two V^{+4} ions or one V^{+3} ion must be created.[16] Enhanced absorption in the low-energy tail is most likely associated with either or both of these species.

V. SUMMARY

A series of V–O alloy films were grown on glass substrates by reactive sputter deposition using a V target and Ar/O_2 discharges containing 2% to 8% O_2. The optical behavior of the films from 390 nm (3.18 eV) to 700 nm (1.77 eV) was studied by spectrophotometry. Transmission and reflection measurements were used to determine the absorption coefficient as a function of incident photon energy.

The following conclusions can be drawn from the results presented above:

(1) The optical absorption edge for all films shows two distinct regions of behavior. A high photon energy region in which α varies linearly with $(h\nu)^2$ is associated with valence-to-conduction band transitions. A low-energy tail is associated with interband transitions involving impurity states within the gap.

(2) X-ray diffraction results show that (010) planes of the orthorhombic V_2O_5 lattice are oriented parallel to the substrate in all films. These planes consist of successive layers of V + O and O atoms. The (010) interplanar spacing decreases from the bulk value as the sputtering gas O_2 content decreases from the amount necessary to form an oxide layer at the target surface. The contraction in (010) interplanar spacing is consistent with a model[16] for the structure of nonstoichiometric V_2O_5 with O vacancies in (010)-type O layers.

(3) Optical absorption in the high photon energy region appears to depend upon V–O coordination. Based on the structural model cited above, V–O coordination changes only after enough O vacancies are created so that adjacent V–O planes collapse.

(4) Optical absorption in the low-photon-energy tail increases as the sputtering gas O_2 content decreases from the amount necessary to form an oxide layer at the target surface. Absorption in the tail region is associated with self-impurities, in particular with V in an oxidation state lower than + 5.

ACKNOWLEDGMENTS

This work was supported by the U. S. Army Research Office under Grant No. DAAG29-84-0126. The authors wish to thank G. S. Baker and C. J. G. Kubiak for helpful comments.

[1]G. S. Nadkarni and V. S. Shirodkar, Thin Solid Films **105**, 115 (1983).
[2]F. J. Morin, Phys. Rev. Lett. **3**, 34 (1959).
[3]N. F. Mott, Rev. Mod. Phys. **40**, 677 (1968).
[4]D. Adler, Rev. Mod. Phys. **40**, 714 (1968).
[5]C. N. Berglund and H. J. Guggenheim **185**, 1022 (1969).
[6]L. Michailovits, I. Hevesi, Liem Phan, and Zs. Varga, Thin Solid Films **102**, 71 (1983).
[7]G. A. Rozgonyi and W. J. Polito, J. Electrochem. Soc. **115**, 56 (1968).
[8]S. D. Hansen and C. R. Aita, J. Vac. Sci. Technol. A **3**, 660 (1985).
[9]See, for example, T. Abe and T. Yamashina, Thin Solid Films **30**, 19 (1975); J. Heller, Thin Solid Films **17**, 163 (1973); E. Hollands and D. S. Campbell, J. Mater. Sci. **3**, 544 (1968).
[10]V. G. Mokerov and A. V. Rakov, Sov. Phys. Solid State **11**, 150 (1969).
[11]B. Karvaly and I. Hevesi, Z. Naturforsch **26a**, 245 (1971).
[12]N. Kenny, C. R. Kannewurf, and D. H. Whitmore, J. Phys. Chem. Solids **27**, 1237 (1966).
[13]Z. Bodo and I. Hevesi, Phys. Status Solidi **20**, K45 (1967).
[14]See, for example, J. I. Pankove, *Optical Processes in Semiconductors* (Prentice-Hall, New Jersey, 1971); T. S. Moss, *Optical Properties of Semiconductors* (Butterworths, London, 1961).
[15]Joint Committee on Powder Diffraction Standards, File No. 9-387 (1974). Note that crystal axes *b* and *c* are reversed in this reference from the manner in which they appear throughout the literature.
[16]E. Gillis and E. Boesman, Phys. Status Solidi **14**, 337 (1966).
[17]H. G. Bachmann, F. R. Ahmed, and W. H. Barnes, Z. Kristallogr. Mineral. **115**, S. 110 (1961).
[18]V. A. Ioffe and I. B. Patrina, Phys. Status Solidi **40**, 389 (1970).
[19]L. V. Azaroff, *Elements of X-Ray Crystallography* (McGraw-Hill, New York), pp. 556–558.
[20]G. D. Cody, in *Semiconductors and Semimetals*, edited by J. I. Pankove (Academic, New York, 1984), Vol. 21, Part B.
[21]J. M. Ziman, *Models of Disorder* (Cambridge University, Cambridge, UK, 1979), pp. 36–71, 456–459.
[22]R. Zallen, *The Physics of Amorphous Solids* (Wiley, New York, 1983), pp. 261–274.
[23]C. J. Gawlak and C. R. Aita, J. Vac. Sci. Technol. A **1** 415 (1983).
[24]D. Redfield, Phys. Rev. **130**, 916 (1963).
[25]J. I. Pankove, Phys. Rev. **140**, A2059 (1965).
[26]C. R. Aita and N. C. Tran (unpublished).

APPENDIX F

LOW-TEMPERATURE OXIDATION OF NONSTOICHIOMETRIC SPUTTER DEPOSITED VANADIUM PENTOXIDE

Low-temperature oxidation of nonstoichiometric sputter deposited vanadium pentoxide

Carolyn Rubin Aita and Mei Lee Kao
Materials Department and the Laboratory for Surface Studies, University of Wisconsin–Milwaukee, Milwaukee, Wisconsin 53201

(Received 18 September 1986; accepted 17 November 1986)

V_2O_5 is a layered compound in which alternating sheets of V_2O_5 atoms and O atoms alone are oriented parallel to the ⟨010⟩ lattice direction. Recent interest in O-deficient V_2O_5 centers around its use as an oxidation catalyst. In the present paper, nonstoichiometric V_2O_5 films were sputter deposited onto glass substrates and annealed in air at 280 °C. Changes in crystallography and optical absorption in the 390 to 700 nm wavelength region were determined as a function of time at temperature. Low-temperature oxidation is used here as a probe for understanding the structure of the as-deposited film and to study the evolution of film structure as annealing progresses.

I. INTRODUCTION

Bulk V_2O_5 has an orthorhombic lattice at room temperature, with parameters $a_0 = 11.519$ Å, $b_0 = 4.373$ Å, and $c_0 = 3.564$ Å.[1] In a perfect lattice, each V atom is surrounded by six O atoms which form the corners of a distorted octahedral cage [Fig. 1(a)].[2] Two of the V–O bonds are directed along the *b* axis (⟨010⟩ direction). One of these bonds is much longer than the other, hence weaker, and also longer than the other four V–O bonds in the system. As a result, a V atom in V_2O_5 is in effect in five-, not sixfold, coordination with O.

The effective fivefold coordination of V with O leads to an extended array of pyramids whose apices (vanadyl O atoms) are pointed alternately up or down along the *b* axis.[3–7] The pyramids are joined at shared corners (chain O atoms) to form zig–zag chains along the *c* axis. The chains are crosslinked with groups of three O atoms (bridge O atoms) to form layers perpendicular to the *b* axis. These layers consist of V + O atoms and O atoms alone, as shown in the projection of the {001} plane in Fig. 1(b).

The defect structure of both as-grown bulk single-crystal and thin layers of reduced vanadium pentoxide involves vanadyl O vacancies.[4,6–8] The geometry of a single defect is shown in Fig. 1(c). A model by Gillis and Boesman,[9] based on an electron paramagnetic resonance study,[6] proposed that atomic order in the V–O layers is not disturbed by a small vanadyl O vacancy concentration. However, when there are a sufficient number of vanadyl O vacancies present, V–O planes collapse and the V_2O_5 lattice shears locally to form a fault with a V_6O_{13} structure. V–O coordination in the faulted region changes from distorted octahedral (V_2O_5) to tetragonal (V_6O_{13}). The results of an early low-energy electron diffraction (LEED) study by Fiermans and Vennik[4] showed that the reduction of V_2O_5 involves the removal of every third vanadyl O layer. The intermediate oxides, V_3O_7 and V_4O_9, are described in a survey article by Fiermans *et al.*[10] V–O coordination in these phases is octahedral as in V_2O_5, and their structure can be considered to be V_2O_5 with a superimposed defect sublattice of ordered vanadyl O vacancies.

In a previous study,[11] we examined the optical behavior in the visible spectrum (1.8–3.2 eV) and crystallographic properties of V–O alloy films grown on water-cooled glass substrates by sputtering a V target in Ar–O_2 gas containing less than the critical O_2 content necessary to form an oxide layer at the target surface. On the basis of x-ray diffraction (XRD), the films were nominally identified as V_2O_5, grown with the *b* axis perpendicular to the substrate plane. However, two factors led us to conclude that the films were nonstoichiometric:

(1) There was a low-energy tail on the optical absorption edge. V in an oxidation state of less than + 5 in bulk V_2O_5 is known to cause absorption bands in this region.[7,12–15] Chem-

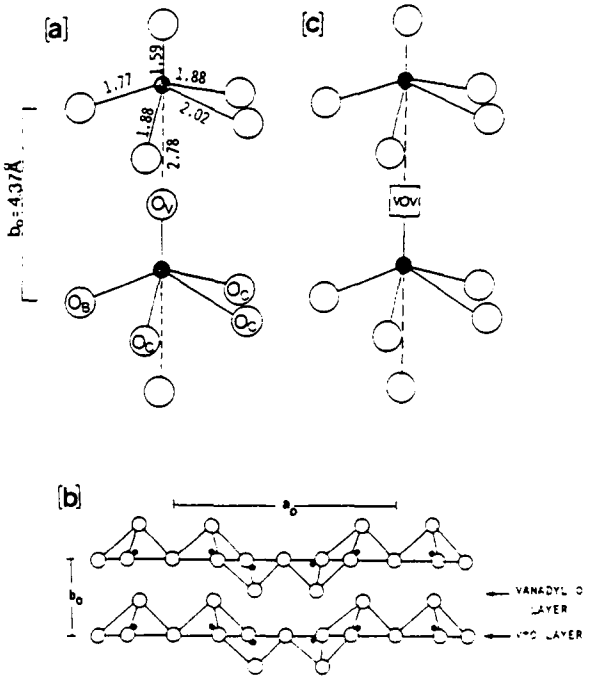

FIG. 1. (a) The effective fivefold coordination of V with O in a perfect V_2O_5 lattice. Dark circles represent V atoms. White circles represent O atoms. O_V = vanadyl O, O_C = chain O, O_B = bridge O. Bond lengths are shown in Å. ($V–O_V$ bond length differs among investigators, the value used here is from Ref. 10.) (b) A projection of the {001} plane of the V_2O_5 lattice (after Ref. 11). (c) The atomic arrangement around a single O_V vacancy.

 0734-2101/87/042714-04$01.00

ical analysis by x-ray photoelectron spectroscopy (XPS) and Auger electron spectroscopy (AES) showed that there were no foreign impurities present in the films which would account for the absorption tail.

(2) The average value of the b-lattice parameter was smaller than that for bulk stoichiometric V_2O_5. Contraction of b is associated with vacancies in the vanadyl O layer and the relaxation of the surrounding V–O layers into the vacancy.[16]

The degree of nonstoichiometry was estimated to be in the range $VO_{2.5-x}$, where $0 < x < 0.33$. This estimate is based on the aforementioned XRD results which show that the as-deposited film contains a V_2O_5 component, that is, is not completely V_6O_{13} ($x = 0.33$). AES line shapes, XPS V/O peak height, and chemical shift in binding energy of the V $2p$ and O $1s$ core electrons are commensurate with those reported for V_2O_5, although AES and XPS are not particularly sensitive techniques for distinguishing higher-order V oxides.[17]

The interest in nonstoichiometric V_2O_5 films centers around the use of this material as an oxidation catalyst.[10,18–20] In the present paper, low-temperature oxidation is used as a probe for understanding the structure of the as-deposited film, and to study the evolution of film structure as annealing progresses.

II. EXPERIMENTAL PROCEDURE

A. Film deposition

A liquid-N_2 cold-trapped, hot-oil diffusion pumped radio-frequency-excited planar diode sputter deposition apparatus was used to grow the films. The target was a 7.6-cm-diam disk of 99.7% V which was bonded to a water-cooled stainless-steel cathode. The substrates were 7.6×2.5 cm glass slides chemically cleaned using a chelating procedure and placed in contact with a Cu anode. To prevent Cu contamination of the film by backsputtering, areas of the anode which were not covered by the substrates were coated with ~ 100 Å of V prior to deposition. The distance between target and substrates was 5 cm.

The chamber was evacuated to a base pressure of 5×10^{-7} Torr, throttled, and backfilled with 0.01 Torr of 99.999% pure Ar gas. With a shutter covering the substrates, the target was sputtered in Ar using 300-W forward power (2.3 kV peak-to-peak) for 45 min. The discharge was extinguished, the chamber was reevacuated, throttled, and backfilled with a gas mixture of Ar–2% O_2 at a total pressure of 0.01 Torr. The target was sputtered in this gas mixture for 45 min. The shutter was then opened and the film was deposited. After deposition, film thickness was determined from the height of a step using a profilometer and found to be 5.4 ± 0.1 kÅ.

B. Optical behavior

A Perkin–Elmer model 330 double-beam spectrophotometer with a specular reflection attachment was used to measure the transmittance T and reflectance R of near-normal incidence radiation in the 390–700 nm wavelength range. The absorption coefficient (α) was calculated as described in Ref. 11, from the following relationship[21]:

$$T = \{(1-R)^2 \exp(-\alpha x)\}/\{1 - R^2 \exp(-2\alpha x)\}. \quad (1)$$

For the experimental data presented here, the term $R_2 \exp(-2\alpha x)$ is always less than 3% of unity and is therefore neglected.

C. Crystallography

Diffraction patterns were obtained using 1.5418-Å wavelength (λ) unresolved Cu $K\alpha$ radiation. The diffractometer was calibrated using the $\{10\bar{1}0\}$ peak of a polycrystalline quartz standard at $2\theta = 20.84°$. The precise peak position ($\pm 0.02°$), the relative intensity, and the full peak width at one-half the maximum intensity (FWHM) were measured. The FWHM due to instrument effects alone was 0.18°, measured from the $\{10\bar{1}0\}$ quartz peak. For each sample, five measurements were made at each of three equidistant places along the length of the glass slide substrate. The interplanar spacing $d_{\{hkl\}}$ was calculated by substituting the peak position into the Bragg equation: $n\lambda = 2d_{\{hkl\}} \sin\theta$.

D. Annealing

The samples were inserted into a quartz tube furnace already at temperature and isothermally annealed in air at 280 °C for 30 to 600 min. This was the lowest temperature at which a change in film behavior could be reproducibly measured. During annealing, a thermocouple was attached to the sample. The sample + glass tube was removed from the furnace for cooling. The temperature of the sample dropped from 280 °C to room in 8 min.

III. RESULTS

A. Crystallography

Only diffraction from $\{010\}$ V_2O_5 planes was detected, before and after annealing. The $\{010\}$ interplanar spacing b, is shown in Fig. 2(a) as a function of annealing time. The value of b for the as-deposited material is equal to 4.363 Å and does not change within experimental error for the first 60 min of annealing. This value is 0.23% less than b_0 (4.373 Å). The value of b increases to 4.379 Å as the annealing time is increased from 60 to 240 min. This value is 0.14% larger than b_0.

The FWHM of the $\{010\}$ diffraction peak is shown in Fig. 2(b) as a function of annealing time. There is a large decrease in FWHM after 30 min of annealing after which a small change occurs. In general, materials parameters which contribute to the FWHM include small crystallite size, variation in interplanar spacing, and stacking or growth faults.

The relative intensity of the $\{010\}$ diffraction peak is shown in Fig. 2(c) as a function of annealing time. There is a 4.5-fold increase in intensity within the first 30 min of annealing, after which no further change occurs. The intensity is directly related to the number of crystallites aligned with b axes perpendicular to the substrate.

B. Optical behavior

The optical absorption coefficient, calculated using Eq. (1), is shown in Fig. 3 as a function of the incident photon

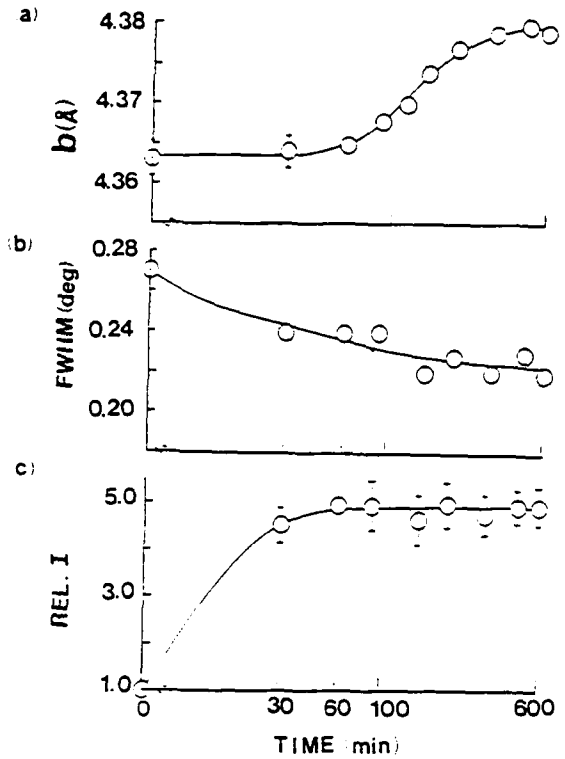

FIG. 2. (a) The interplanar spacing, (b) FWHM, and (c) intensity relative to that obtained from an as-deposited film obtained from the {010}, V_2O_5 x-ray diffraction peak. Error bars indicate two standard deviations from the mean for a sample size > 15. No error bars are shown when the symbol size is > 2 SD.

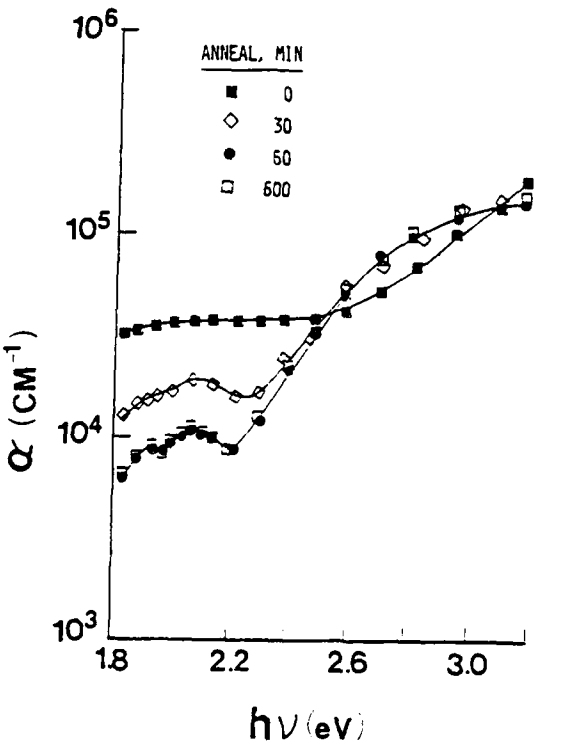

FIG. 3. The optical absorption coefficient as a function of incident photon energy for various annealing times for V_2O_5 films on glass substrates.

energy for annealing times of 0, 30, 60, and 600 min. Changes in α occur for annealing time up to 60 min, after which there is no further change in α. Data for annealing times of 90, 120, 150, 210, 330, and 480 min were identical to that obtained for 60 and 600 min and are not included in Fig. 3.

Two regions of behavior of α as a function of $h\nu$ can be identified:

(1) There is a low-energy region in which α varies slowly with $h\nu$. For the as-deposited material, α is nearly constant for $1.8 < h\nu < 2.5$ eV. For all annealed films, the low-energy region occurs between 1.8 and 2.2–2.3 eV. After a 30-min anneal, the value of α has decreased throughout the low-energy region and a small peak develops at 2.1 eV. After a 60 min anneal, the value of α has further decreased and an additional peak develops at 1.9 eV.

(2) There is a high-energy region in which α increases rapidly with increasing $h\nu$ (charge transfer region). The rapid increase in α is associated with the onset of the fundamental optical absorption edge, resulting from the transfer of electronic charge from valence to conduction band. A large change in the dependence of α on $h\nu$ has occurred in the charge transfer region after a 30-min anneal. Subsequent annealing has no effect on α.

IV. DISCUSSION

Based on the results presented above, the annealing process can be divided into three stages. The first stage (time < 30 min) is marked by pronounced changes in optical absorption. The change in α throughout the charge transfer region indicates a change in the average V–O coordination in the film. This would occur if the as-deposited film contains regions of V_6O_{13}, along with the V_2O_5 phase detected by XRD. The increase in {010} diffraction peak intensity and the decrease in FWHM during the first stage of annealing are consistent with the oxidation of V_6O_{13} growth faults to form V_2O_5.

The decrease in α for $h\nu < 2.3$ eV and the development of a discrete band centered at 2.1 eV indicate a change in the nature of the electronic transition responsible for absorption. The broad, featureless band in the spectrum of the as-deposited film is characteristic of a delocalization of electronic charge. In the case of the isolated defect shown in Fig. 1(c), excess charge is localized near the V site adjacent to the vanadyl O vacancy, giving the ion a V^{+4} nature.[7] Delocalization occurs when the structure of a single defect is disturbed: when the density of vanadyl O vacancies increases so that adjacent defects interact,[6] or when the V_2O_5 lattice collapses to form V_6O_{13}.[6,7,20] As annealing progresses, charge becomes localized in the vicinity of the V site adjacent to the vanadyl O vacancy. Electronic transitions possibly responsible for the absorption band at 2.1 eV are (1) $3d^1 \rightarrow 3d^1$ transitions of the V^{+4} ion in the complex containing the vanadyl O vacancy,[15] or (2) transitions between a $3d^1$ level of the V^{+4} ion and an empty V $3d$ state at the bottom of the V_2O_5 conduction band[7] which has been locally perturbed to lower energy.[8]

The second stage of annealing (30 < time < 60 min) is

marked only by changes in the low-energy region of the absorption spectrum. A further decrease in α and the formation of a second peak at 1.9 eV, indicate that excess charge is becoming increasingly localized. Sharpening of the onset of the fundamental absorption edge indicates a decrease in the number of V $3d$ states (the bottom of the V_2O_5 conduction band) perturbed to lower energy by the presence of vanadyl O vacancies.

The third stage of annealing ($60 < \text{time} \leq 240$ min) is marked by an increase in the lattice constant b with no further change in optical behavior. Possible explanations include the diffusion of additional O to interstitial sites in the vanadyl O layer in spite of the fact that vanadyl O vacancies remain,[20] and the formation of an ordered array of vanadyl O vacancies.[10,22]

V. SUMMARY

We have studied the changes in crystallography and optical absorption in the 390–700 nm wavelength region that occur when nonstoichiometric sputter deposited V_2O_5 films are annealed at low temperature in air. XRD results show that as-deposited films contain a V_2O_5 constituent with {010} planes oriented parallel to the substrate. However, a change in the average V–O coordination during the early stage of annealing supports a model for the as-deposited material in which V_6O_{13} growth faults are present. This is consistent with the structure of reduced bulk V_2O_5 single crystals. Annealing occurs in three stages. First, there is oxidation of regions of the film in which the V–O coordination is not octahedral (as in V_6O_{13} growth faults). Second, there is increased localization of excess electronic charge on the V site adjacent to a vanadyl O vacancy giving the ion a V^{+4} nature. Finally, there is an increase in {010} interplanar spacing with no further change in optical absorption.

ACKNOWLEDGMENTS

We thank Professor G. S. Baker for helpful comments. This work was supported under U. S. Army Research Office Grant No. DAAG29-84-K-0126.

[1]ASTM Joint Commission on Powder Diffraction Standards File No. 9-387, (1974). Lattice parameters b and c are reversed in this reference from the manner in which they appear throughout the literature.
[2]A. Bystrom, K.-A. Wilhelmi, and O. Brotsen, Acta Chem. Scand. **4**, 1119 (1950); L. E. Orgel, *An Introduction to Transition-Metal Chemistry: Ligand Field Theory* (Methuen, London, 1960), pp. 173–174.
[3]H. G. Bachmann, F. R. Ahmed, and W. H. Barnes, Z. Kristal. **115**, S. 11 (1961).
[4]L. Fiermans and J. Vennik, Surf. Sci. **9**, 187 (1968).
[5]A. Mosset, P. Lecante, J. Galy, and J. Livage, Philos. Mag. B **46**, 137 (1982).
[6]E. Gillis and E. Boesman, Phys. Status Solidi **14**, 337 (1966).
[7]P. Clauws and J. Vennik, Phys. Status Solidi B **66**, 553 (1974).
[8]W. Lambrecht, B. Djafari-Rouhani, and J. Vennik, J. Phys. C **19**, 369 (1986).
[9]E. Gillis and G. Remaut, C. R. Acad. Sci. **262**, 1215 (1966).
[10]L. Fiermans, P. Clauws, W. Lambrecht, L. Vandenbrouche, and J. Vennik, Phys. Status Solidi A **59**, 485 (1980).
[11]C. R. Aita, Y.-L. Liu, M. L. Kao, and S. D. Hansen, J. Appl. Phys. **60**, 749 (1986).
[12]C. Sanchez, F. Babonneau, R. Morineau, J. Livage, and J. Bullot, Philos. Mag. B **49**, 279 (1983).
[13]J. Bullot, P. Cordier, O. Gallais, M. Gauthier, and F. Babonneau, J. Non-Cryst. Solids **68**, 135 (1984).
[14]N. Kenny, C. R. Kannewurf, and D. H. Whitmore, J. Phys. Chem. Solids **27**, 1237 (1966).
[15]C. J. Ballhausen and H. B. Gray, Inorg. Chem. **1**, 111 (1962).
[16]W. Lambrecht, B. Djafari-Bouhani, and J. Vennik, Surf. Sci. **126**, 558 (1983).
[17]J. Kasperkiewicz, J. A. Kovacich, and D. Lichtman, J. Electron Spectrosc. Relat. Phenom. **32**, 123 (1983).
[18]M. V. Copaert, Z. Physiol. Chem. **84**, 150 (1973).
[19]L. Fiermans, L. Vandenbrouche, R. Vandenberge, J. Vennik, and G. Dalmai, J. Microsc. Spectrosc. Electron. **4**, 543 (1979).
[20]J. H. Perlstein, J. Solid State Chem. **3**, 217 (1971).
[21]See, for example, J. I. Pankove, *Optical Processes in Semiconductors* (Prentice–Hall, Englewood Cliffs, NJ, 1971).
[22]R. S. D. Tilley and B. G. Hyole, J. Phys. Chem. Solids **31**, 1613 (1970).

APPENDIX G

INTERLAYER SPACING OF SPUTTER DEPOSITED VANADIUM PENTOXIDE FILMS

AD-A193 497 LOW TEMPERATURE FILM GROWTH OF THE OXIDES OF ZINC ALUMINUM AND VANADIUM (.. (U) WISCONSIN UNIV MILWAUKEE LAB OF SURFACE STUDIES C R AITA FEB 88 ARO-21334.19-MS 2/2

UNCLASSIFIED DAAG29-84-K-0126 F/G 7/4 NL

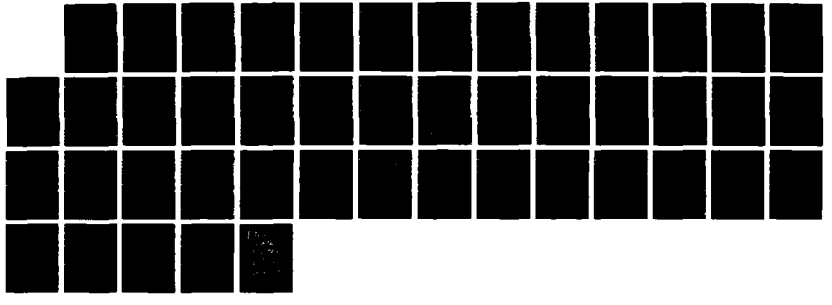

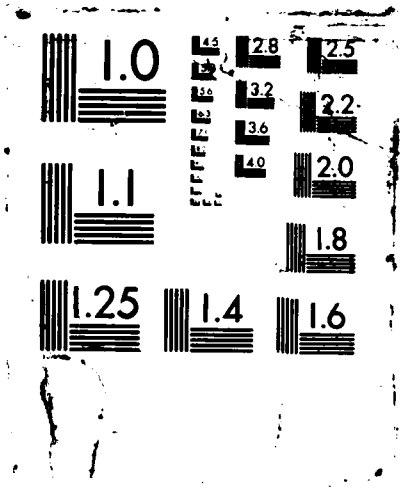
1.0
1.1
1.25
1.4
1.6
1.8
2.0
2.2
2.5
2.8
3.2
3.6
4.0

INTERLAYER SPACING OF SPUTTER DEPOSITED VANADIUM PENTOXIDE

Carolyn Rubin Aita, Chee-Kin Kwok, and Mei Lee Kao
Materials Department and the Laboratory for Surface Studies
University of Wisconsin - Milwaukee
P.O. Box 784
Milwaukee, Wisconsin 53201

ABSTRACT

Vanadium pentoxide films were grown by sputtering a V target in O_2-bearing atmospheres containing 0 to 98% Ar. The interlayer spacing was studied as a function of sputtering gas O_2 content. The results are discussed in terms of defects in the vanadyl O layer and correlated with target surface oxidation.

INTRODUCTION

Vanadium pentoxide is of current interest as an oxidation catalyst [1-4] and as a thermally-activated electrical and optical switching material [5]. At room temperature, the compound is a wide band gap semiconductor [6-9] with an orthorhombic lattice [10]. The atomic arrangement along the [010] lattice direction consists of alternating sublayers of V+O atoms and O atoms alone (vanadyl O sublayer) [11-15]. This arrangement is shown schematically in Fig. 1 which is the projection of the V_2O_5 lattice onto the (001) plane.

The present paper deals with the (010) interplanar spacing of films which have been deposited on unheated laboratory glass slide substrates by sputtering a V target in rf-excited O_2-bearing discharges containing 0 to 98% Ar. All films have in common a component identifiable by x-ray diffraction (XRD) as V_2O_5, oriented with (010) planes parallel to the substrate. No other orientations of the V_2O_5 lattice were detected. No V-suboxides were detected by XRD. However, spectrophotometric measurements [9,16] showed that films deposited in Ar-2% O_2 discharges contained a component in which V-O bonding was not octahedral, characteristic of V_2O_5. We previously concluded that V_6O_{13} growth faults were present, in addition to the V_2O_5 phase. The stoichiometry of these films was estimated to be V_2O_{5-x} with $0 < x < 0.33$.

EXPERIMENTAL PROCEDURE

Film Deposition and *In Situ* Discharge Diagnostics: A liquid N_2-cold trapped, hot-oil diffusion pumped, rf-excited planar diode sputter deposition apparatus was used to grow the films. Film growth has been previously described in Refs. 9, 16, and 17. To summarize here, the sputtering target was a 7.6 cm diameter disc of 99.7% V which was bonded to a water-cooled stainless steel cathode. The substrates were laboratory glass slides chemically cleaned using a chelating procedure and placed in contact with a Cu anode. To prevent Cu contamination of the film by backsputtering of the anode, areas of the anode which were not covered by the substrates were coated with 100 Å of V prior to deposition. The distance between target and substrate surface was 5 cm.

The chamber was backfilled to a pressure of 1×10^{-2} Torr with 99.999% pure Ar gas. Before backfilling, the chamber was evacuated to 5×10^{-7} Torr. The residual gas in the chamber was water-vapor. With a shutter covering the substrates, the target was sputter cleaned using a 300 W Ar discharge for 45 min. The discharge was then extinguished, the chamber was re-

Mat. Res. Soc. Symp. Proc. Vol. 82. © 1987 Materials Research Society

evacuated, throttled, and backfilled with a particular Ar-O_2 mixture or O_2 of 99.97% purity. Discharges containing 2, 4, 6, 8, 10, 25, and 100% O_2 were investigated.

The target was sputtered in the O_2-bearing atmosphere of choice for an additional 45 min before the shutter was opened and a film deposited on the substrates. Deposition time was 3 h. Film thickness ranged from 2 to 5 kÅ depending upon discharge composition [9,17].

Optical emission spectroscopy was used to monitor the number of V atoms sputtered from the target surface during the course of each deposition, as described in detail in Ref. 17. The V atom population in the plasma volume was related to the state of target surface oxidation. We concluded that the target surface became increasingly oxidized by the discharge as the sputtering gas O_2 content was increased from 2 to 8%. At Ar-8% O_2, the target surface was fully oxidized and no longer acted as a getter for O_2 in the discharge.

Crystallography: X-ray diffraction patterns were obtained using 1.5418 Å wavelength (λ) unresolved Cu Kα radiation. The diffractometer was calibrated using the $\{10\bar{1}0\}$ peak of a polycrystalline quartz standard at $2\theta = 20.84^0$. The precise peak position ($\pm 0.02^0$) and the full peak width at one half the maximum intensity (FWHM) were measured. The FWHM due to instrument effects alone was 0.18^0, measured from the $\{10\bar{1}0\}$ quartz peak. For each sample, five measurements were made at each of three equidistant places along the length of the glass slide substrate. The interplanar spacing, d{hkl}, was calculated by substituting the peak position into the Bragg equation: $n\lambda = 2d\{hkl\}\sin\theta$.

RESULTS

The (010) interplanar spacing, b, is recorded in Table I and shown as a function of sputtering gas O_2 content in Fig. 2a. The value of b_o, the interlayer spacing for bulk, unstressed V_2O_5 is equal to 4.373 Å [10]. The difference in interlayer spacing between the films studied here and bulk, unstressed V_2O_5 is given by the relationship:

$$\Delta b = (b-b_o)/b_o \qquad [1]$$

The values of Δb are recorded in Table I. The expression "strain" is not used to describe Δb because the measured (010) interplanar spacing may be that which results in an unstrained lattice for a particular film non-stoichiometry.

Table I: (010) Interplanar Spacing of Sputter Deposited Vanadium Pentoxide

Gas O_2 Content	b [Å]	Δb[%]
2%	4.363 ± 0.003	-0.23
4%	4.363 ± 0.007	-0.23
6%	4.368 ± 0.003	-0.11
8%	4.381 ± 0.004	+0.18
10%	4.402 ± 0.007	+0.66
25%	4.421 ± 0.005	+1.10
100%	4.423 ± 0.003	+1.14

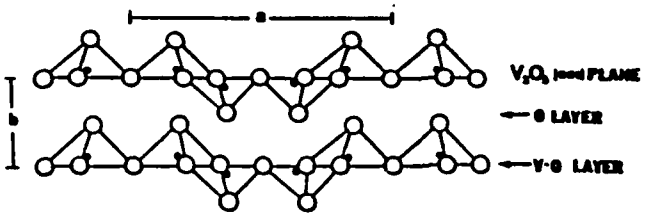

Fig. 1: The V_2O_5 (001) plane. White circles represent O atoms. Black circles represent V atoms. (From Ref. 9)

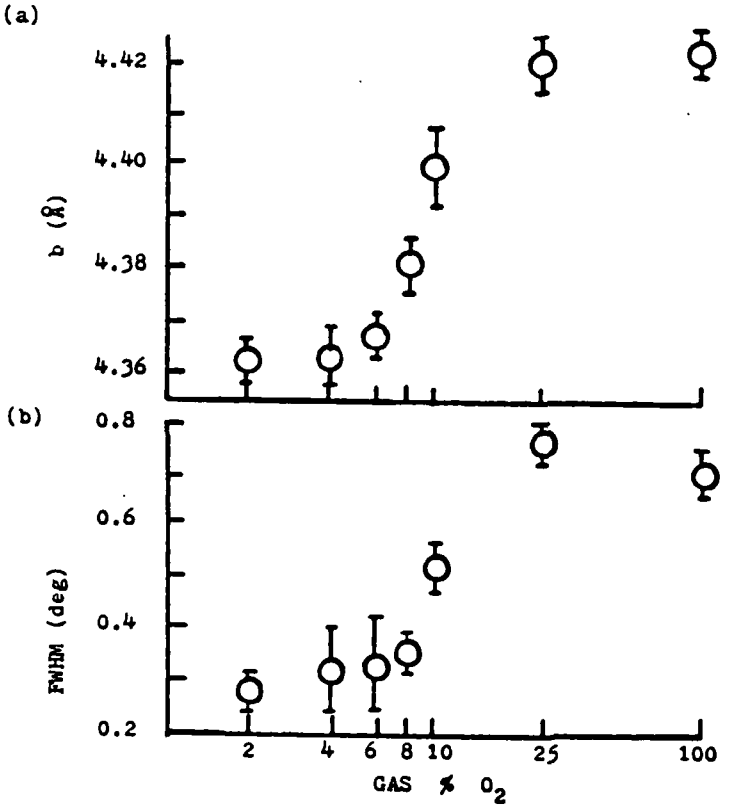

Fig. 2: (a) The (010) interplanar spacing, and (b) the FWHM of the (010) diffraction peak as a function of sputtering gas O_2 content.

The FWHM of the (010) diffraction peak is shown in Fig. 2b as a function of sputtering gas O_2 content. The FWHM for all samples is greater than expected from instrumental effects alone. In general, materials parameters which contribute to peak broadening are small crystallite size, stacking faults, and non-uniform strain (distribution of lattice spacing about the average value). Two orders of two diffraction peaks are required to realistically estimate the individual contribution from each factor [18] and this information is unavailable (as is usually the case) in thin films with a strong preferred orientation.

DISCUSSION

It can be seen from Fig. 2a that there are two regions in which the interlayer spacing varies slowly with sputtering gas O_2 content: $b<b_o$ (gas O_2 content $\leq$ 6%) and $b>b_o$ (gas O_2 content $\geq$ 25%). There is a transition region in which b rapidly increases from less than to greater than b_o. The onset of the transition region is marked by a rapid increase in FWHM, as seen from Fig. 2b, and is concurrent with the complete oxidation of the target surface [17].

We previously studied the dependence of optical absorption on gas O_2 content for sputtering gas containing 2 to 8% O_2 [9]. The results showed that as the sputtering gas O_2 content was decreased from 8 to 4%, vacancies in the vanadyl O sublayer formed. An increase in vanadyl O vacancy concentration was detected first by the growth of an isolated absorption band and subsequently by a broad tail adjacent to the fundamental optical absorption edge at 2.48 eV. A contraction of the interlayer spacing, as seen in the results of the present study, would be expected to accompany the formation of O vacancies in the vanadyl O sublayer as the sputtering gas O_2 content is decreased.

No further decrease in interlayer spacing occurs as the gas O_2 content is decreased from 4 to 2%. As mentioned in the Introduction, films deposited in 2% O_2 gas contain a V_6O_{13} component, in the form of growth faults. Apparently, the V_2O_5 lattice cannot sustain an interlayer contraction < 0.23% without undergoing a phase transition to a lower oxide.

With respect to films deposited in sputtering gas containing >8% O_2, the arrival of excess oxygen, unable to be gettered by the oxidized target surface, and the incorporation of this oxygen into the film as interstitials in the vanadyl O layer [4], would account for the increase in interlayer spacing above b_o. However, precise chemical analysis of the films is required to prove this hypothesis.

SUMMARY

Vanadium pentoxide films were grown by sputtering a V target in O_2-bearing atmospheres containing 0 to 98% Ar. All films had solely a (010) orientation; sublayers of V+O atoms and O atoms alone were oriented parallel to the substrate plane. The interlayer spacing was studied as a function of sputtering gas O_2 content.

The results show that b is very sensitive to the sputtering gas O_2 content. Correlation with previous studies allowed us to relate b to the state of V target surface oxidation. Values of $b<b_o$, the interlayer spacing in bulk unstressed V_2O_5, are discussed in terms of vanadyl O vacancies. Values of $b>b_o$ are discussed in terms of interstitials in the vanadyl O sublayer.

ACKNOWLEDGEMENTS

This research was supported by the U.S. Army Research Office under Contract No. DAAG29-84-K-0126. The authors thank Prof. G.S. Baker for many fruitful discussions.

REFERENCES

1. L. Fiermans, P. Clauws, W. Lambrecht, L. Vandenbrouche, and J. Vennik, phys. stat. sol (a) 59, 485 (1980).
2. M.V. Copaert, Z. Phys. Chem. 84, 150 (1973).
3. L. Fiermans, L. Vandenbrouche, R. Vandenberge, J. Vennik, and G. Dalmai, J. Micros. Spectros. Electron. 4, 543 (1979).
4. J.H. Perlstein, J. Sol. State Chem. 3, 217 (1971).
5. G.S. Nadkarni and V.S. Shirodkar, Thin Sol. Films 105, 115 (1983).
6. N. Kenny, C.R. Kannewurf, and D.M. Whitmore, J. Phys. Chem. Solids 27, 1237 (1966).
7. B. Karvaly and I. Hevesi, Z. Naturforsch 26a, 245 (1971).
8. Z. Bodo and I. Hevesi, phys. stat. sol. 20,K45 (1967).
9. Carolyn Rubin Aita, Ying-Li Liu, Mei Lee Kao, and Steven D. Hansen, J. Appl. Phys. 60, 749 (1986).
10. Joint Committee on Powder Diffraction Standards, File No. 9-387 (1974). Note that the crystal axes b and c are reversed in this reference from the manner in which they appear throughout the literature.
11. H.G. Bachmann, F.R. Ahmed, and W.H. Barnes, Z. Kristallogr. Mineral. 115, S. 110 (1961).
12. L. Fiermans and J. Vennik, Surf. Sci. 9, 187 (1968).
13. A. Mosset, P. Lecante, J. Galy, and J. Livage, Phil. Mag. B 46, 137 (1982).
14. E. Gillis and E. Boesman, phys. stat. sol. 14, 337 (1966).
15. A. Bystrom, K.-A. Wilhelmi, and O Brotsen, Acta Chem. Scand. 4, 1119 (1950).
16. Carolyn Rubin Aita and Mei Lee Kao, J. Vac. Sci. Technol A 5. xxx (1987) in press.
17. S.D. Hansen and C.R. Aita, J. Vac. Sci. Technol. A 3, 660 (1985).
18. L.V. Azaroff, Elements of X-ray Crystallography (McGraw-Hill, New York, 1968) pp. 556-558.

APPENDIX H

RESISTIVITY CHANGES AND PHASE EVOLUTION IN W-N FILMS SPUTTER DEPOSITED IN $Ne-N_2$ AND $Ar-N_2$ DISCHARGES

ABSTRACT #262
PROGRAM #TF-TuP2

J. Vac. Sci. Technol. A 6 (May-June 1988)
Book 2, in press.

RESISTIVITY CHANGES AND PHASE EVOLUTION IN W-N FILMS SPUTTER DEPOSITED IN Ne-N_2 AND Ar-N_2 DISCHARGES

Karl John Huber and Carolyn Rubin Aita
Materials Department and the Laboratory for Surface Studies
University of Wisconsin-Milwaukee
P.O. Box 784
Milwaukee, Wisconsin 53201

ABSTRACT

The effect of discharge N_2 content and rare carrier gas type on the crystal structure and electrical resistivity of sputter deposited W-nitride films is reported here. A diode apparatus was used to sputter a W target in rf-excited Ne-N_2 and Ar-N_2 discharges spanning composition range from pure rare gas to pure N_2. Post-deposition analysis included x-ray diffraction and four-point probe resistivity measurements. The results show that in Ar-N_2 discharges, phase evolution proceeds with increasing discharge N_2 content as follows: $\alpha W+\beta W$ -> low resistivity micro-crystalline phase, a-W(N) -> W_2N -> high resistivity phase, X.W-nitride. The use of Ne-N_2 discharges accelerated the formation of the higher N content phases and surpressed the formation of a-W(N).

I. INTRODUCTION

Tungsten nitride films were produced in this study by rf diode reactive sputter deposition onto {111}-cut Si and glass substrates. Two deposition parameters were investigated: discharge N_2 content and the type of carrier gas used. The purpose of this study was to investigate phase evolution as a function of easily controllable deposition parameters.

Published information about the W-N system is limited. Much of the work to date has been by Nicolet and co-workers [1-3] who deposited W-N alloys using Ar-N_2 discharges in an rf magnetron system. Although the aim of the investigation was for diffusion barrier applications between Si and a metallic overlayer, phase evolution as a function of gas N_2 content and post-deposition annealing was also reported.

Other researchers studied electrical resistivity, [4] superconducting behavior, [5] optical properties, [6] and Schottky barrier properties [7,8] of specific W-nitrides. However, these studies were directed towards the fabrication of a specific device, rather than to obtain fundamental information about the sputter deposited W-N alloy system.

There are three places in a N_2-bearing sputter deposition discharge where chemical reactions that control compound formation in the film can occur: 1) at the substrate, 2) at the target surface by the formation of a nitrided layer which becomes in effect the target material, and 3) in the plasma volume. Plasma volume studies of rf-excited rare+reactive gas sputtering discharges have been reported. [9-11] An important process which occurs

is Penning ionization, the ionization of a ground state N_2 molecule through a collision with a rare gas atom in a low-lying metastable level.[12,13] Metastable Ne atoms carry sufficient energy (E_m=16.6, 16.7eV) to ionize ground state N_2 (first ionization potential=15.6eV) whereas metastable Ar atoms do not (E_m = (11.5, 11.7eV). It is known that by an impact dissociation mechanism, N_2^+ ions are more reactive with a W surface than neutral N_2 species.[14]

In addition to producing N_2^+, there are other possible reasons why the use of Ne rather than Ar carrier gas will aid the nitriding process. As a physical sputterer, Ne with half the mass of Ar will have a smaller energy transfer function[15] when incident on the target surface. For the same accelerating cathode voltage, the sputtering yield will be less when Ne is used. A reduced sputtering yield leads to a reduction in deposition rate. Therefore more time is available for nitriding reactions, which depend upon surface diffusion, to occur at the substrate. Furthermore, Ne incident on a nitrided target surface will cause less dissociation than Ar, again from energy transfer function considerations. The flux arriving at the substrate will therefore consist of a larger percentage of nitrided W species.

II. EXERIMENTAL PROCEDURE

Film Deposition: The films were prepared by sputtering a 12.7cm-diam, 99.995% W target in Ar-N_2 and Ne-N_2 discharges containing 0-100%N_2. A diffusion-pumped, liquid N_2-trapped, rf diode system was used. Gas purity was 99.999% for Ar and N_2, and 99.996% for Ne. A capacitance manometer was used to

establish the partial pressure of the gases which were admitted separately into the chamber. {111}-cut Si wafers and laboratory glass slides were used as substrates. Substrates were chemically cleaned using a chelating procedure and placed in thermal contact with a water-cooled Cu pallet which covered the anode. Prior to deposition the chamber was evacuated to 3.0×10^{-7} torr and backfilled to 1×10^{-2} torr with Ar. The target was cleaned by sputtering with Ar for 60min with a shutter covering the substrates. This cleaning process was followed by a 45min sputtering of the target with the gas mixture under investigation. The second process was carried out to allow the formation and dissociation of a nitrided target layer to reach steady state. In the third and final operation, the shutter was opened and a film was deposited. The anode-cathode spacing was 5cm, the cathode voltage (V_c) was either -1000 or -1600V (p-p), and the anode was at ground. Specific deposition conditions are recorded in Table I.

Film Characterization: A section of each substrate was masked during deposition to produce a step from which film thickness was measured using a Tencor Alpha-200 model profilometer with an instrument accuracy of $\pm 5\%$. Growth rate was calculated by dividing the value of the film thickness by deposition time.

Sheet resistance was measured using a four-point probe.(16) Resistivity was calculated by taking the product of the sheet resistance, a shape factor (4.532 for an infinite sheet), and film thickness.

Crystallography was determined by x-ray diffraction (XRD) using 1.54Å wavelength unresolved Cu Kα radiation. Diffraction patterns in the 2θ range from 20-90° were taken. Peak position (2θ), relative intensity (I), and full width at half the maximum intensity (FWHM) were determined. Interplanar spacing (d) was determined from the Bragg equation. The accuracy in measuring peak position was ±0.1°. The instrument was calibrated using a quartz standard. The FWHM of the quartz $\{10\bar{1}1\}$ diffraction peak at 2θ=26.66° was 0.18°. This value was assumed to represent peak broadening caused solely by instrument effects.

III. RESULTS AND DISCUSSION

Table I lists film thickness, growth rate, and resistivity. Growth rate and resistivity are shown as a function of discharge N_2 content in Figs. 1 and 2 respectively. Figure 3 shows typical XRD patterns in the 2θ range from 30 to 44°. Quantitative results obtained from XRD are recorded in Table II.

Bulk W (αW) has a bcc lattice structure and a resistivity of 5.4μΩ-cm. The resistivity reported for sputter deposited W films[1,7,17] is considerably higher than that for bulk W. This has been attributed to the formation of a metastable phase, fcc βW which has an A15 crystal structure.[17]

In the present study, αW and βW phases were found to coexist in films deposited using pure Ar and Ne discharges. The resistivity of these films lies between that of αW and the range of values reported for βW, 150-350μΩ-cm.

Films deposited in Ar-N_2 discharges containing 10-25%N_2 show a single broad diffraction peak, indicating the presence of a

microcrystalline phase denoted here "a-W(N)". The resistivity of these films is low, ranging from 175±20 to 337±96 $\mu\Omega$-cm. The N-rich W_2N_{1+x} phase was formed when the discharge N_2 content was increased to 50%. The d-spacings for W_2N_{1+x} recorded in Table II indicate a W_2N lattice [18] expanded with interstitial nitrogen [1].

Diffraction patterns of films deposited in Ar-N_2 discharges containing 75% N_2 show a single weak peak, corresponding to a d-spacing of 2.51-2.56Å. This peak is also present in films deposited in 100% N_2. No assignment can be made on the basis of this reflection. The phase to which it corresponds is denoted "X.W-nitride" here. Films which contain X.W-nitride have a high resistivity. In consideration of the weakness of the reflection, it is likely that the X.W-nitride phase is embedded in a matrix of material that shows no long range crystallographic order when inspected by XRD.

Phase evolution in films deposited in Ar-N_2 discharges in this study is similar to that reported in Ref. (1). Low resistivity films identified as "amorphous" in Ref. (1) are considered to be identical to the microcrystalline a-W(N) produced here. In both studies, the yet-be-identified X.W-nitride phase was present. Neither βW(N) (containing $\geq$18- <33 atom% N) nor W_2N (containing 33 atom% N) was observed in as-deposited films.

In films grown in Ne-N_2 discharges, the a-W(N) phase was not observed. Instead, phase evolution proceeded from two-phase $\alpha W+\beta W$ directly to W_2N_{1+x}. The transition occurred at low discharge N_2 content, 5-7%, compared to 50%N_2 required to produce W_2N_{1+x} when an Ar-N_2 discharge was used. A further

small increase in discharge N_2 content to 12-14% produced an order of magnitude increase in resistivity and the formation of the X.W-nitride phase.

The possibility of a slower deposition rate being solely responsible for the accelerated formation of higher N content phases when Ne carrier gas was used can be eliminated by considering the curves presented in Fig. 1. For any nominal discharge composition there is approximately a three-fold increase in growth rate associated with an increase in V_c from -1000 to -1600V. However, the data recorded in Table II shows that phase evolution is independent of V_c within each gas system, Ar-N_2 or Ne-N_2. Furthermore, the growth rate of films deposited in Ne-N_2 discharges operated at -1600V and Ar-N_2 discharges operated at -1000V is the same throughout the range of discharge N_2 content. However, phase evolution in each system is very different. We conclude that the accelerated formation of high N content phases when Ne rather than Ar carrier gas is used is not a consequence of increased time for surface diffusion and compound synthesis at the substrate.

A recent study of Al-N alloys sputter deposited using Ne-N_2, Ar-N_2, and Ne-Ar-5%N_2 discharges monitored the production of N_2^+ as a function of nominal discharge composition.[11] The results showed that there was considerably more N_2^+ in the discharge, in particular for small nominal amounts of N_2, when Ne rather than Ar carrier gas was used. This result was not surprising in view of the discussion of Penning ionization in Sec. I. In the case of W-nitride formation, the existence of N_2^+ in the discharge is

apparently the factor that leads to the accelerated formation of high N content phases in films deposited using Ne-N_2 discharges.

IV. SUMMARY

The effect of discharge N_2 content and rare carrier gas type type on the crystal structure and electrical resistivity of sputter deposited W-nitride films was studied. Phase evolution proceeded as follows when Ar-N_2 discharges of increasing N_2 content were used: $\alpha W+\beta W$ -> low resistivity microcrystalline a-W(N) -> W_2N_{1+x} ->high resistivity X-W-nitride. When Ne-N_2 discharges were used, phase evolution proceeded from $\alpha W+\beta W$ directly to W_2N_{1+x} at very low discharge N_2 content.

A slower deposition rate, hence more time for nitriding reactions to occur at the substrate was eliminated as being responsible for the accelerated formation of high N content phases when Ne rather than Ar carrier gas was used. It was concluded that the presence of N_2^+ in the discharge was the critical factor in forming high N content phases at low discharge N_2 content. The importance of target versus substrate nitriding reactions with respect to the formation of a particular phase will be the subject of future investigation.

Acknowledgements: The authors gratefully acknowledge Prof. M.-A. Nicolet for helpful discussions and Prof. B. Brown for enabling us to use the XRD facility in the Department of Geological Sciences at UW-Milwaukee. This research was supported by a Johnson's Wax Fund Research Fellowship and under U.S. Army Research Office Grant No. DAAG29-84-K-0126.

References

1) K. Affolter, H. Kattelus, and M.-A. Nicolet, Proc. Mater. Res. Soc. 47, 167 (1985).

2) H.P. Kattelus, E. Kolawa, K. Affolter, and M.-A. Nicolet, J. Vac. Sci. Technol. A 3, 2246 (1985).

3) E. Kolawa, F.C.T. So, J.L. Tandon, and M.-A. Nicolet, J. Electrochem. Soc., in press.

4) K. Reichelt and G. Bergmann, J. Appl. Phys. 46, 2747 (1975).

5) F.M. Kilbane and P.S. Habid, J. Vac. Sci. Technol. 12, 107 (1975).

6) L.A. Cherzova and B.P. Kryzhanowshii, Opt. Scpectrosc. 34, 234 (1973).

7) N. Uchitomi, M. Nagaoka, K. Shimada, T. Mizoguchii, and N. Toyoda, J. Vac. Sci. Technol. B 4, 1392 (1986).

8) A.E. Geissberger, R.A. Sadler, F.A. Leyenaar, and M.L. Balzan, J. Vac. Technol. A 4, 3091 (1986).

9) C.R. Aita and M.E. Marhic, J. Appl. Phys. 52, 6584 (1981).

10) C.R. Aita and M.E. Marhic, J. Vac. Sci. Technol. A 1, 69 (1983).

11) J.R. Siettmann, Growth of AlN_x Films in N_2-Ne, N_2-Ne-Ar, and N_2-Ar Discharges: Construction of Ternary Gas Composition Diagrams. MS Thesis, University of Wisconsin-Milwaukee, 1987.

12) F.M. Penning, Z. Phys. 46, 225 (1925); 57, 723 (1929).

13) H. Hotop and A. Niehaus, Z. Phys. 215, 1395 (1968); 228, 68 (1969).

14) H.F. Winters and D.E. Horne, Surf. Sci. 24, 587 (1971).

15) B. Chapman, Glow Discharge Processes (Wiley, New York, 1980) pp. 180-184. See refs. within. [The energy ransfer function for an Ar-W collision is 0.59 and for a Ne-W collision is 0.35.]

16) L.B. Valdes, Proc. IRE 42, 420 (1954).

17) P. Petroff, T.T Sheng, A .K. Sinha, G.A. Rozgoni, and F.B. Alexander, J. Appl. Phys. 44, 2545 (1973).

18) ASTM Jt. Comm. on Powder Diffraction Stds. Card No. 25-1257 (1975).

TABLE I: Deposition conditions, film thickness, growth rate and resistivity of sputter deposited W and W-nitride films.

Gas % N_2	Power (W)	Thickness (Å)	Growth Rate (Å/min)	Resistivity (μΩ-cm)
I. Ar-N_2, V_c=-1000V				
0	100	1468±119 [a]	101±18	184±16
10	100	956±109	62±7	174±20
25	100	1305±429	87±29	337±96
50	100	1198±26	60±1	660±23
75	100	795±200	32±8	3537±815
II. Ar-N_2, V_c=-1600V				
0	300	1050±93	294±24	135±13
25	290	807±35	161±7	220±12
49	295	1497±439	150±44	424±99
74	285	568±107	81±15	1571±263
79	290	743±296	106±42	2874±838
III. Ne-N_2, V_c=-1000V				
0	110	982±50	22±1	132±8
7	105	1312±114	20±2	348±35
12	100	882±191	20±4	2798±544
15	100	1161±117	23±2	4839±552
25	100	733±216	12±4	14109±3409
26	100	738±221	13±4	15685±3964
35	100	849±261	14±4	7151±1720
50	100	827±44	15±1	13796±1127
59	100	850±41	12±1	9222±168
88	100	931±166	16±3	12746±2281
91	97	892±49	13±1	8830±577
IV. Ne-N_2, V_c=-1600V				
0	260	1332±150	63±7	143±16
5	300	1369±9	63	253±4
14	285	899±182	45±9	1291±244
25	275	1344±206	52±8	7285±1174
50	265	1108±278	55±14	6008±1269
66	265	960±233	45±5	8660±2050
69	260	900±103	53±8	7996±1711
71	275	1057±160	48±12	5328±707
V. N_2, V_c=-1000V				
100	100	905±277	15±5	8398±2032
VI. N_2, V_c=-1600V				
100	280	905±192	57±12	5061±1005

a) Error represents ±1 standard deviation from the mean value.

TABLE II: Crystallography of sputter deposited W and W-nitride films.

Gas%N_2	Phase	2θ(deg)	hkl	d(Å)	FWHM(deg)	Rel I	No.(a
I. Ar-N_2, V_c=-1000V:							
1. 0	αW	38.93	110	2.31	1.0	100	2
	βW	34.73	111	2.58	0.6	57	3
	βW	42.63	200	2.12	0.6	20	1
2. 10	a-W(N)	38.83	-	2.32	3.4	100	
3. 25	a-W(N)	37.83	-	2.38	6.6	100	
4. 50	W_2N_{1+x}	35.73	111	2.51	2.0	100	4
5. 75	X.W-nitride	35.11	-	2.56	2.4	100	
II. Ar-N_2, V_c=-1600V:							
6. 0	αW	39.34	110	2.29	1.6	100	6
	βW	35.79	111	2.51	1.0	63	7
	βW	42.84	200	2.11	1.4	27	5
7. 25	a-W(N)	38.43	-	2.34	4.0	100	
8. 50	W_2N_{1+x}	36.36	111	2.47	1.2	100	9
	W_2N_{1+x}	42.68	200	2.12	1.2	65	8
	W_2N_{1+x}	61.13	220	1.52	1.6	11	
9. 75	X.W-nitride	35.56	-	2.52	1.7	100	
10. 79	X.W-nitride	35.83	-	2.51	1.6	100	
III. Ne-N_2, V_c=-1000V							
11. 0	αW	39.53	110	2.28	1.4	100	11
	βW	35.23	111	2.55	1.3	75	12
	βW	42.53	200	2.13	0.6	13	10
12. 7	W_2N_{1+x}	36.23	111	2.48	1.0	100	14
	W_2N_{1+x}	42.28	200	2.14	1.5	54	13
	W_2N_{1+x}	61.43	220	1.51	1.6	21	
13. 25	X.W-nitride	35.23	-	2.55	4.2	100	
14. 50	X.W-nitride	35.43	-	2.53	1.2	100	
15. 88	X.W-nitride	35.13	-	2.55	1.7	100	
IV. Ne-N_2, V_c=-1600V							
16. 0	αW	39.63	110	2.27	1.2	100	15
	βW	35.33	111	2.54	1.0	25	16
17. 5	W_2N_{1+x}	36.83	111	2.44	1.4	100	18
	W_2N_{1+x}	42.83	200	2.11	1.5	60	17
	W_2N_{1+x}	62.13	220	1.49	1.0	23	
18. 25	X.W-nitride	35.63	-	2.52	2.6	100	
19. 50	X.W-nitride	35.73	-	2.51	2.2	100	
	X.W-nitride	63.63	-	1.46	0.5	45	
20. 66	X.W-nitride	35.43	-	2.53	1.6	100	
V. N_2, V_c=-1000V							
21. 100	X.W-nitride	35.53	-	2.53	2.2	100	
VI. N_2, V_c=-1600V							
22. 100	X.W-nitride	35.43	-	2.53	2.6	100	

a) Peak number in Fig. 3.

Figure Captions:

Fig. 1: The growth rate as a function of discharge N_2 content for films produced in Ar-N_2 and Ne-N_2 discharges with −1000 or −1600V applied to the cathode. Error bars represent ±1 standard deviation from the mean.

Fig. 2: The resistivity of W and W-nitride films as a function of discharge N_2 content. Error bars represent ±1 standard deviation from the mean.

Fig. 3: Typical XRD patterns of W and W-nitride films in the 2θ range from 30 to 44°. Identification of the numbered peaks is given in Table II.

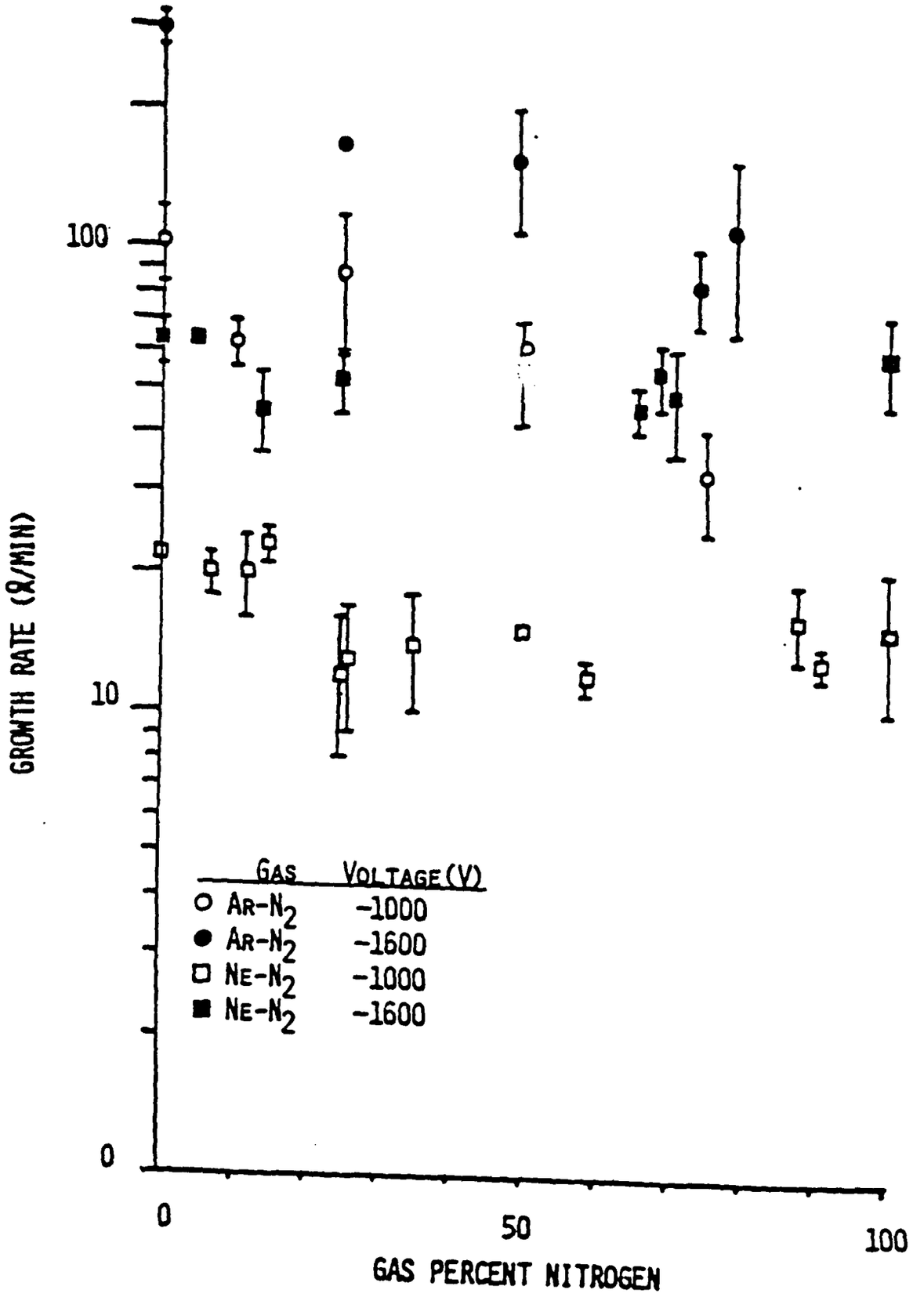
GROWTH RATE (Å/MIN)
100
10
0
0
50
100
GAS PERCENT NITROGEN
GAS VOLTAGE(V)
AR-N2 -1000
AR-N2 -1600
NE-N2 -1000
NE-N2 -1600

Fig 7

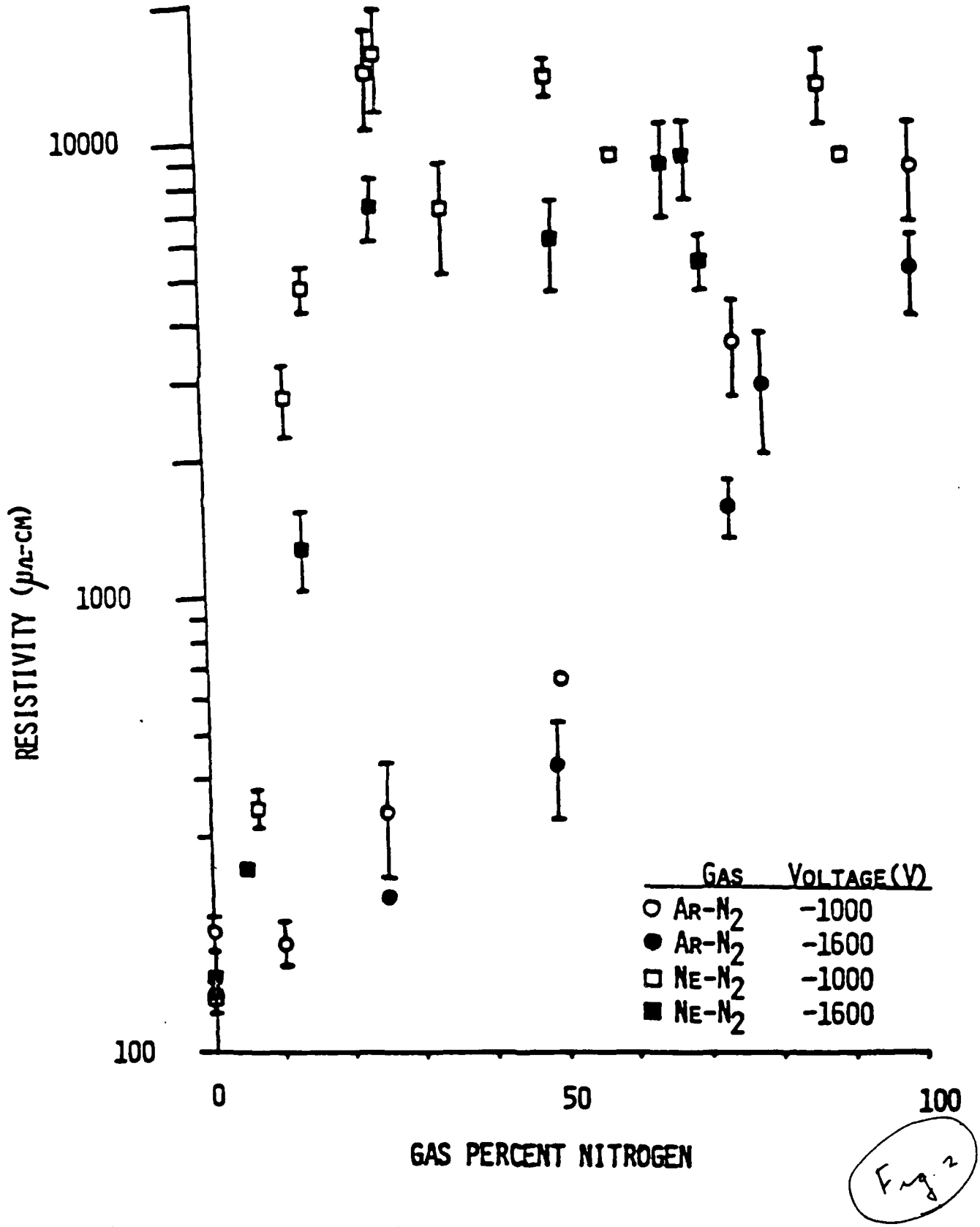
10000
1000
100
RESISTIVITY (μΩ-CM)
0
50
100
GAS PERCENT NITROGEN
GAS
VOLTAGE(V)
AR-N2 -1000
AR-N2 -1600
NE-N2 -1000
NE-N2 -1600

Fig 2

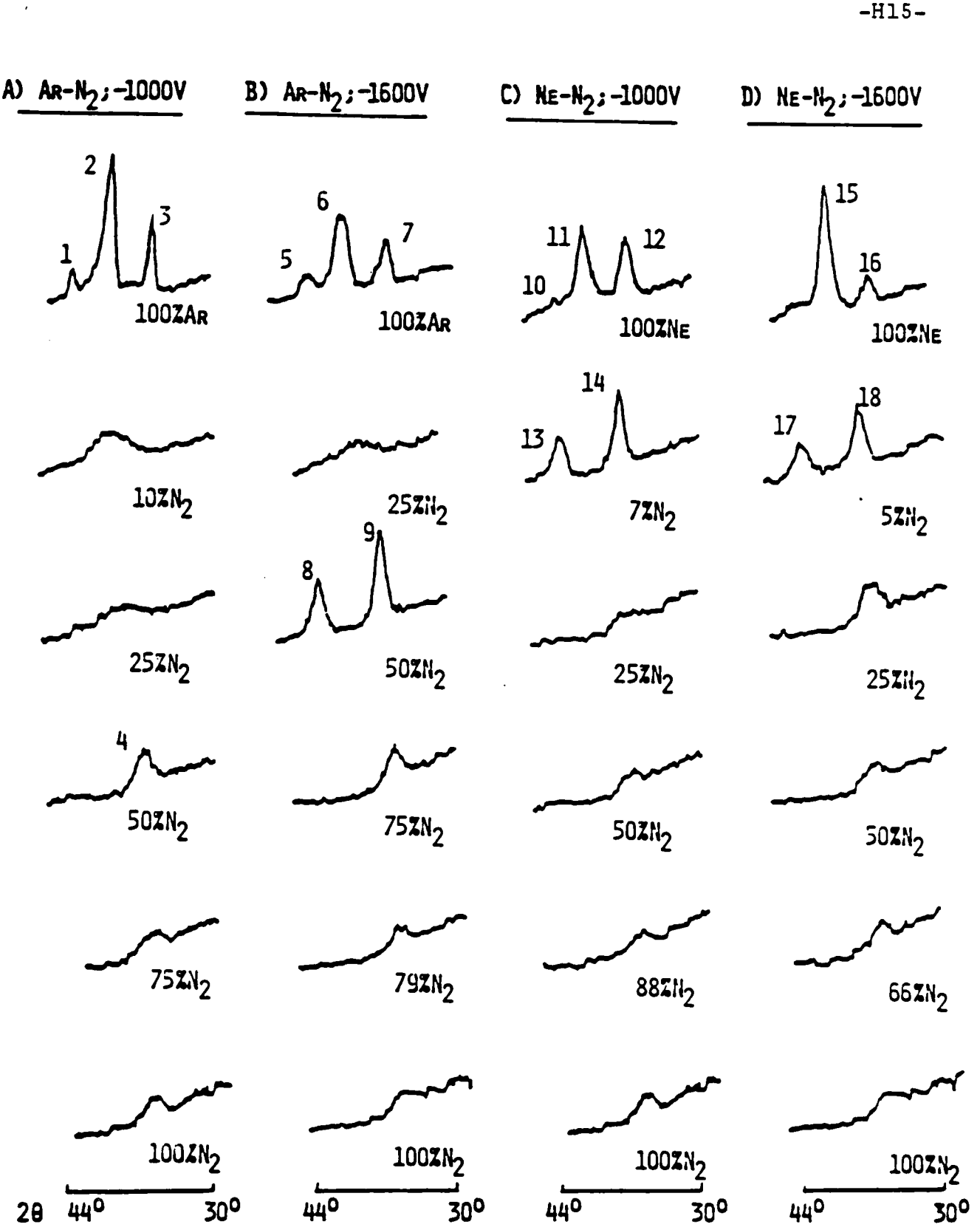
A) Ar-N2; -1000V
B) Ar-N2; -1600V
C) Ne-N2; -1000V
D) Ne-N2; -1600V
1
2
3
100%Ar
5
6
7
100%Ar
10
11
12
100%Ne
15
16
100%Ne
10%N2
25%N2
13
14
7%N2
17
18
5%N2
25%N2
8
9
50%N2
25%N2
25%N2
4
50%N2
75%N2
50%N2
50%N2
75%N2
79%N2
88%N2
66%N2
100%N2
100%N2
100%N2
100%N2
2θ
44°
30°
44°
30°
44°
30°
44°
30°

Fig. 3

APPENDIX I

AuO^+ AND AuO_2^+ GASEOUS IONS FORMED DURING THE SPUTTER DEPOSITION OF Au FILMS IN $Ar-O_2$ DISCHARGES

AuO^+ and AuO_2^+ gaseous ions formed during the sputter deposition of Au films in Ar-O_2 discharges

Carolyn Rubin Aita
Materials Department and the Laboratory for Surface Studies, University of Wisconsin–Milwaukee, P.O. Box 784, Milwaukee, Wisconsin 53706

(Received 26 November 1986; accepted for publication 2 February 1987)

AuO^+ and AuO_2^+ gaseous ions formed during the sputtering of an Au target in 1.0×10^{-2} Torr, rf-excited Ar-O_2 discharges were studied by glow-discharge mass spectrometry. These ions are created from neutral species in the negative glow and are incident on the substrate during a sputter deposition. The relative flux of AuO_2^+/Au^+, AuO^+/Au^+, and AuO_2^+/AuO^+ was determined for gas compositions from 100% Ar to 100% O_2. The results show that the arrival of Au-oxide species at the substrate, in addition to Au atoms, must be taken into account when modeling the growth of Au films sputter deposited in O_2-bearing discharges.

The effect of oxygen on Au film growth on oxide glass substrates has been of continuing interest for the past two decades.[1–4] In the case of sputter-deposited Au, early work by Mattox[1] has shown that film adhesion is enhanced when O_2 is added to the Ar sputtering discharge. The reason for this behavior is is not yet understood.

Moore and Thornton[5] studied the reaction of molten Au droplets with a silica substrate in an oxygen atmosphere. They concluded that Au reacted with oxygen from the atmosphere to form a stable Au-oxide which alloyed with the silica. There was strong bonding between the Au-doped silica and subsequent Au droplets placed upon it. Mattox suggested a similar process was occurring during sputter deposition, with Au-oxide formation at the substrate assisted by active oxygen species created in the glow discharge. The analysis assumed that the only target species incident on the substrate were Au. However, Aita and Tran[6] have shown that Pt–O bond formation in sputter-deposited Pt-O alloys is controlled by oxidation of Pt metal at the target surface. Hecq *et al.*[7] and Aita[8] have shown that Pt-oxide species arrive at the substrate along with metallic Pt.

In the present paper, the occurrence of AuO^+ and AuO_2^+ gaseous ions formed during the sputtering of an Au target in Ar-O_2 discharges is monitored by glow-discharge mass spectrometry as a function of gas O_2 content. Glow-discharge mass spectrometry (GDMS) is a method of determining the relative flux and energy of positive ions incident on the substrate plane.[8,9] Ions bearing target species detected by GDMS originate from sputtered neutrals which have been ionized in the negative glow. A positive ion sputtered from the target will not be able to escape the cathode field and therefore will not be detected by GDMS.

Possible reactions in the plasma volume which lead to the formation of Au-oxide gaseous ions can be divided into two categories: (1) Ionization reactions involving a Au-oxide molecule sputtered from an oxidized layer at the target surface. (2) Oxidation + ionization reactions involving a Au atom sputtered from the target surface. With respect to the second category, two-body collisions to form AuO^+ and AuO_2^+ directly are highly unlikely because of the momentum conservation constraint. Associative ionization reactions between Au and various oxygen species in which one or both reactants are in excited electronic states are energetically possible. However, in general an associative ionization reaction is unlikely unless one of the reactants is in a metastable state.[10] The same argument holds for the occurrence of (a) dissociative ionization involving Au and O_2 in which the product AuO_2^+ dissociates to form AuO^+ and O, and (b) dissociative ionization involving Au and higher order oxygen molecules, O_3 and O_4. It is therefore assumed that Au-oxide ions detected by GDMS are sputtered as some form of neutral Au-oxide molecule from the oxidized surface of the Au target. The relationship of ionic to neutral flux cannot be determined for the Au-O system because this requires[11] knowledge of the ionization potentials of AuO and AuO_2, which are unknown.

References 8 and 12 describe the rf diode sputter deposition apparatus with attached spectrometer used in this experiment. Positive ions from the negative glow were sampled through an orifice in the substrate table covering the anode.

 0021-8979/87/115182-03$02.40

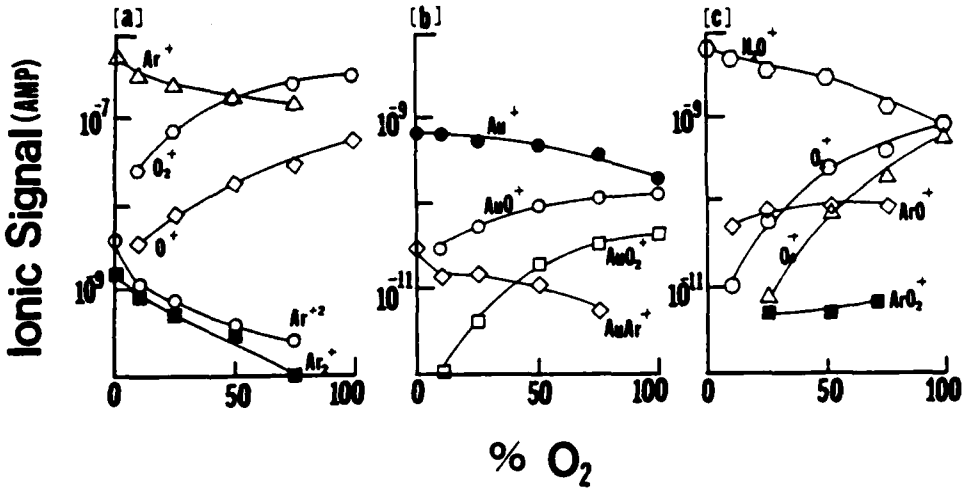

FIG. 1. The GDMS ionic signal intensity as a function of sputtering gas O_2 content for: (a) Ar^+ (40 amu), O_2^+ (32 amu), O^+ (16 amu), Ar^{+2} (20 amu), and Ar_2^+ (80 amu); (b) Au^+ (196 amu), AuO^+ (212 amu), AuO_2^+ (228 amu), and $AuAr^+$ (236 amu); (c) H_2O^+ (18 amu), O_3^+ (48 amu), O_4^+ (64 amu), ArO^+ (56 amu), and ArO_2^+ (72 amu). Total discharge pressure is 1×10^{-2} Torr.

A 20-cm-diam Au target was bonded to the cathode. The chamber was pumped to 5×10^{-7} Torr base pressure and backfilled with the Ar-O_2 mixture under investigation. 99.999% pure Ar and 99.97% pure O_2 were admitted separately and mixed in the chamber. Sputtering gas compositions from 100% Ar to 100% O_2 were investigated. The majority of data were taken at a total discharge pressure of 1×10^{-2} Torr, although a limited amount of data were taken at higher pressure. An anode-cathode separation of 9 cm and a cathode voltage of -1400 V (p-p) were used throughout the experiment. GDMS signals in the 1–300 amu range were collected.

Figure 1 shows the intensity of ionic signals of 12 species as a function of sputtering gas O_2 content for a total discharge pressure of 1×10^{-2} Torr. Ions bearing target species are: Au^+ (196 amu), AuO^+ (212 amu), AuO_2^+ (228 amu), and $AuAr^+$ (236 amu). Unusual ions containing Ar, such as $AuAr^+$, ArO^+, and ArO_2^+ are the products of associative ionization reactions involving neutral Ar atoms in long-lived metastable states and neutral ground state Au or O_2.[10,12–14]

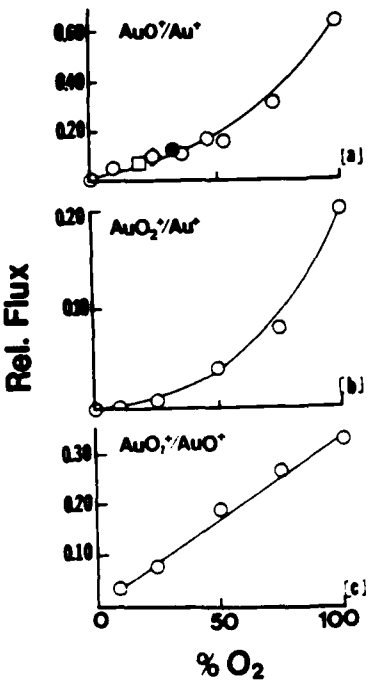

FIG. 2. The relative flux to the substrate of (a) AuO^+/Au^+ ions, (b) AuO_2^+/Au^+ ions, and (c) AuO_2^+/AuO^+ ions as a function of sputtering gas O_2 content. Total pressure is: ○—1.0, ●—2.0, ◇—2.5, □—3.0×10^{-2} Torr.

Figures 2(a) and 2(b) show the relative flux of AuO^+/Au^+ and AuO_2^+/Au^+ species. In both cases, there is a rapid increase in the flux of Au-oxide relative to Au species as the sputtering gas O_2 content is increased above 50%. Comparing the Ar^+ and O_2^+ fluxes shown in Fig. 1(a), it can be seen that for gas containing $<50\%$ O_2 the majority particle population capable of sputtering the target changes from Ar^+ to O_2^+.

A limited amount of data taken at discharge pressure $>1\times10^{-2}$ Torr is presented in Fig. 2(a). It can be seen that increasing the discharge pressure from 1 to 3×10^{-2} Torr does not affect the relative AuO^+/Au^+ flux. This result suggests that both ions are formed from their corresponding neutral molecules by a single-step ionization process.[11]

The relative AuO_2^+/AuO^+ flux, shown in Fig. 2(c), increases linearly with increasing sputtering gas O_2 content. The O_2^+ flux is also a linear function of sputtering gas O_2 content. Simple correlation of these results indicates that the sputtered target species is different depending upon whether the bombarding ion is Ar^+ or O_2^+. However, characterization of the target surface is essential to further understand the sputtering dynamics which result in the ejection of Au-oxide species.

In summary, we have shown that AuO^+ and O_2^+ gaseous ions are formed when a Au target is sputtered in Ar-O_2 discharges. The arrival of Au-oxide molecules at the substrate, in addition to Au atoms, must be taken in account when modeling the growth of Au films sputter deposited in O_2-bearing discharges.

The author wishes to thank Professor M. E. Marhic and Professor G. S. Baker for helpful comments. Preparation of this manuscript was supported under U.S. Army Research Office Grant No. DAAG29-84-K-0126.

[1]D. M. Mattox, J. Appl. Phys. **37**, 3613 (1966).
[2]L. Holland, *The Properties of Glass Substrates* (Wiley, New York, 1964).
[3]J. Salem and F. Sequeda, J. Vac. Sci. Technol. **18**, 149 (1981).
[4]R. J. Martin, W. G. Sainty, and R. P. Netterfield, Vacuum **35**, 621 (1985).
[5]D. C. Moore and H. P. Thornton, J. Res. Natl. Bur. Stand. **62**, 127 (1959).
[6]C. R. Aita and N. C. Tran, J. Appl. Phys. **55**, 6051 (1983); **56**, 985 (1984).
[7]M. Hecq, A. Hecq, and T. Robert, J. Vac. Sci. Technol. **16**, 960 (1979).
[8]C. R. Aita, J. Vac. Sci. Technol. A **3**, 630 (1985).
[9]J. W. Coburn, Rev. Sci. Instrum. **41**, 1219 (1970).
[10]E. E. Muschlitz, Jr. and M. J. Weiss, in *Atomic Collision Processes*, edited by M. R. C. McDowell (North-Holland, Amsterdam, 1964), pp. 1073–1079.
[11]J. W. Coburn, E. W. Eckstein, and Eric Kay, J. Vac. Sci. Technol. **12**, 151 (1975).
[12]C. R. Aita and R. J. Lad, J. Appl. Phys. **60**, 837 (1986).
[13]Z. Herman and V. Cermek, Nature **199**, 558 (1963).
[14]J. W. Coburn and Eric Kay, J. Chem. Phys. **64**, 907 (1976).

APPENDIX J

J1. Optical Emission from Neon/Oxygen rf Sputtering Discharges

J2. Figure Relating Ne^+, O_2^+, and O^+ Ionic Flux to the Discharge O_2 Content, Obtained by Glow Discharge Mass Spectrometery using a ZnO Cathode.

J3. O^+, O_2^+, O_3^+, and O_4^+ Ions in Ar-O_2 Sputtering Discharges...

J4. $(ArO)^+$ and $(ArO_2)^+$ Ions in rf Sputter Deposition Discharges.

Optical emission from neon/oxygen rf sputtering glow discharges

J1.1

C. R. Aita[a)]

Materials Department and the Laboratory for Surface Studies, University of Wisconsin–Milwaukee, Milwaukee, Wisconsin 53201

M. E. Marhic

Department of Electrical Engineering and Computer Science, Northwestern University, Evanston, Illinois 60201

(Received 22 February 1982; accepted 18 August 1982)

The results of an optical emission study of neon and oxygen species which exist in Ne/O_2 rf diode sputtering glow discharges are presented. Comparing emission intensities in pure Ne and Ne/O_2 mixtures at constant total gas pressure, it was found that the addition of O_2 to the sputtering gas quenches Ne I emission and increases emission from O I and O_2^+ species to a greater extent than that which would be expected from the relative changes in neon and oxygen concentrations, respectively. Although this effect could be caused by a change in the electron density and electron energy distribution function, the correlation between Ne I, O I, and O_2^+ emission suggests that metastable neon atoms may interact directly with ground state diatomic oxygen molecules in two competing ways: (1) by Penning ionization which produces O_2^+, and (2) by a quasiresonant transfer of excitation which leads to the production of O. The results are compared to those previously obtained for Ar/O_2 discharges using identical sputtering conditions, where the dominant interaction between the rare gas and O_2 leads entirely to the production of monatomic oxygen.

PACS numbers: 32.30.Jc, 52.80.Hc, 32.70.Fw, 33.70.Fd

I. INTRODUCTION

Neon/oxygen and argon/oxygen gas mixtures, when used to reactively sputter deposit oxide films, have been observed to yield different film compositions,[1,2] as well as different glow discharge mass spectra,[1,3] for the same metal–oxide system. In a general way, these differences have been attributed to the fact that a metastable neon atom Ne^m can ionize a ground state oxygen molecule O_2^0 by a nonradiative collisional energy transfer (Penning ionization)

$$Ne^m + O_2^0 \rightarrow Ne^0 + O_2^- + e^-, \quad (1)$$

whereas a metastable argon atom cannot.[4–6]

However, a Ne^m–O_2^0 reaction which may possibly compete with that described by reaction (1) was identified by Bennett and co-workers while studying the low pressure discharges of rare gas–oxygen lasers.[7,8] A quasiresonant transfer of excitation was proposed to occur between a metastable rare gas atom and a ground state oxygen molecule which becomes excited to a repulsive energy state and subsequently dissociates. At least one of the atomic oxygen dissociation products is left in an excited state. This sequence of events can be described by the following reactions:

$$R^m + O_2^0 \rightarrow O_2^* + R^0, \quad (2a)$$

$$O_2^* \rightarrow O^* + O(2p\,^3P), \quad (2b)$$

where R denotes a rare gas atom, an asterisk superscript denotes an excited species, and $O(2p\,^3P)$ is the ground state of atomic oxygen.

In a previous study,[9] optical emission spectroscopy was used to investigate the argon and oxygen species which occur in the glow discharge during the reactive rf diode sputtering of a zinc oxide target. Although metastable argon with energy levels at 11.5 and 11.7 eV cannot Penning ionize molecular oxygen, the results indicate that there is an interaction between the two species when the sputtering gas contains less than approximately 15% O_2. An excitation transfer of the type described by Eq. (2) was the proposed mechanism.

In the present paper, we report the optical emission behavior of neon and oxygen species which occur in the glow discharge during the rf diode sputtering of a zinc oxide target using Ne/O_2 gas compositions ranging from pure Ne to pure O_2. The results are discussed in terms of the Ne^m–O_2^0 reactions described by Eqs. (1) and (2) and are compared to the results that we have previously reported for Ar/O_2 discharges generated using identical sputtering conditions. The results presented here could be attributed to a change in the electron density and electron energy distribution function. However, arguments are presented here to support the proposition that the behavior can be explained by a direct interaction between neon and oxygen species.

II. EXPERIMENTAL PROCEDURE

The glow discharge was generated at 13.56 MHz in the previously described rf diode sputtering apparatus.[10] The chamber was pumped to a base pressure of 5×10^{-7} Torr before the sputtering gases, 99.999% Ne and 99.97% O_2,[11] were admitted in various ratios. The total working chamber pressure was 1×10^{-2} Torr. The sputtering target was a 99.999% zinc oxide disc which was bonded to a water-cooled cathode to which a voltage was applied. The anode–cathode separation was 8.9 cm and the rms cathode voltage

 0734-2101/83/010069-05$01.00

was − 1000 V.

Light which was emitted from the region between the anode and the cathode was focused onto the entrance slit of a Jarrel–Ash Model 82-4000 spectrometer. An Oriel Detector Model 7070 was used to detect light at the spectrometer exit slit. The spectroscopic notation that is used throughout this paper is discussed in Appendix A.

III. NEON OPTICAL EMISSION

Twenty five observed emission lines resulting from $2p^5 3s$–$2p^5 3p$ electron transitions of the neutral neon atom (Ne I)[12] and their relative intensities in a pure Ne discharge are recorded in Table I. The ratio of the intensities of any two transitions is not consistent with radiation emitted from a plasma in which the excited states are in thermal equilibrium, and the number of atoms in any given state is proportional to the statistical weight and the Boltzmann factor.[13] On the other hand, we have found that the intensities of the majority of these lines are consistent with radiation emitted from a thin plasma in which the effects of reabsorbed, or imprisoned, radiation[14] can be ignored, and the intensity of the radiation spontaneously emitted upon de-excitation of an electron from an upper level k to a lower level i is given by[15]

$$I_{ki} = (1/4\pi)h\nu_{ik}A_{ki}n_k, \tag{3}$$

where ν_{ik} is the frequency of the radiation, A_{ki} is the Einstein coefficient for spontaneous emission, and n_k is the population of the upper level.

TABLE I. Neon I transitions investigated in this study.

Systematic	Transition Paschen	Wavelength Å	Relative intensity in pure neon
$3s_{12}$–$3p'_{01}$	$1s_5$–$2p_2$	5881.90	10
$3s_{12}$–$3p'_{12}$	$1s_5$–$2p_4$	5944.83	17
$3s_{12}$–$3p'_{11}$	$1s_5$–$2p_5$	5975.53	4
32_{12}–$3p_{12}$	$1s_5$–$2p_6$	6143.06	16
$3s_{12}$–$3p_{11}$	$1s_5$–$2p_7$	6217.28	7
$3s_{12}$–$3p_{22}$	$1s_5$–$2p_8$	6334.43	20
$3s_{12}$–$3p_{23}$	$1s_5$–$2p_9$	6402.25	46
$3s_{12}$–$3p_{01}$	$1s_5$–$2p_{10}$	7032.41	12
$3s_{11}$–$3p'_{01}$	$1s_4$–$2p_2$	6030.00	5
$3s_{11}$–$3p_{00}$	$1s_4$–$2p_3$	6074.34	23
$3s_{11}$–$3p'_{12}$	$1s_4$–$2p_4$	6096.16	29
$3s_{11}$–$3p'_{11}$	$1s_4$–$2p_5$	6128.45	38
$3s_{11}$–$3p_{12}$	$1s_4$–$2p_6$	6304.79	7
$3s_{11}$–$3p_{11}$	$1s_4$–$2p_7$	6382.99	23
$3s_{11}$–$3p_{22}$	$1s_4$–$2p_8$	6506.53	36
$3s_{11}$–$3p_{01}$	$1s_4$–$2p_{10}$	7245.17	5
$3s'_{00}$–$3p'_{01}$	$1s_3$–$2p_2$	6163.59	3
$3s'_{00}$–$3p'_{11}$	$1s_3$–$2p_5$	6266.50	17
$3s'_{00}$–$3p_{11}$	$1s_3$–$2p_7$	6532.88	6
$3s'_{01}$–$3p_{00}$	$1s_2$–$2p_1$	5852.49	100
$3s'_{01}$–$3p'_{01}$	$1s_2$–$2p_2$	6598.95	11
$3s'_{01}$–$3p'_{12}$	$1s_2$–$2p_4$	6678.28	21
$3s'_{01}$–$3p'_{11}$	$1s_2$–$2p_5$	6717.04	11
$3s'_{01}$–$3p_{12}$	$1s_2$–$2p_6$	6929.47	15
$3s'_{01}$–$3p_{22}$	$1s_2$–$2p_8$	7173.94	2

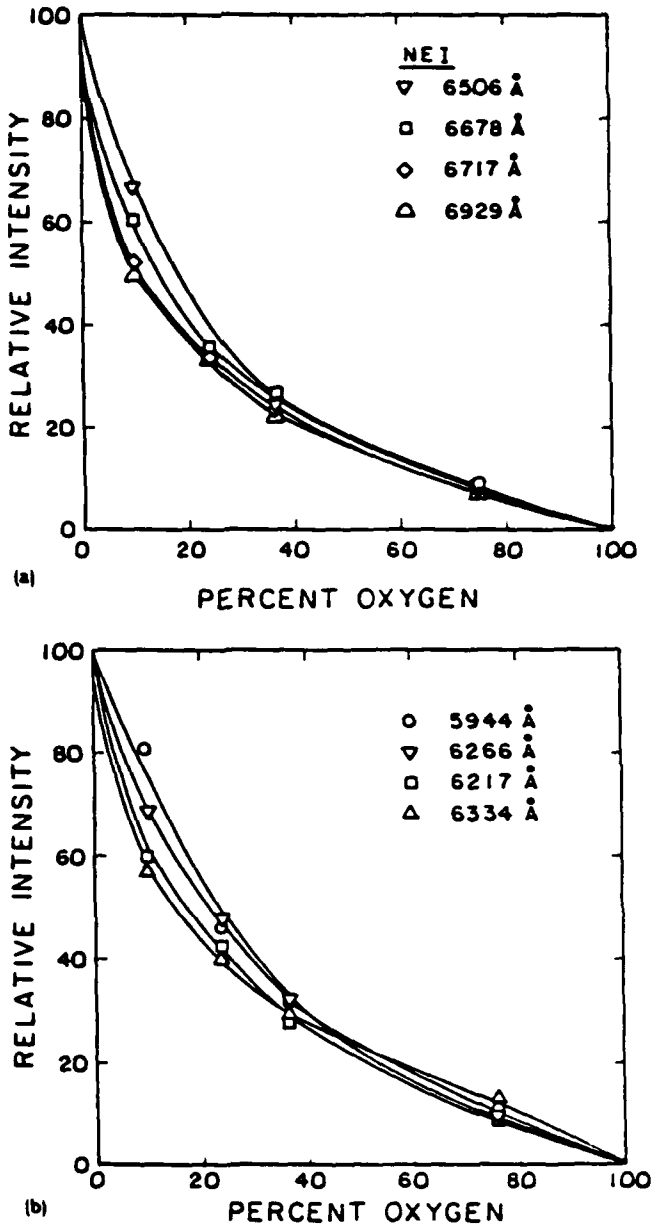

FIG. 1. Neon I emission line intensity normalized to the value of the intensity for (a) four Ne I transitions which terminate in $3s_{11}$ or $3s'_{01}$ (nonmetastable) levels, and (b) four Ne I transitions which terminate in $3s_{12}$ or $3s'_{00}$ (metastable) levels, as a function of sputtering gas O_2 content.

The spectra of eight Ne I transitions were monitored over the range of sputtering gas O_2 content from 0% to 100% without interference from oxygen emission lines or bands. Figure 1 shows the emission line intensity normalized to the value of the intensity when pure Ne sputtering gas is used for (a) four Ne I transitions which terminate in either $3s_{11}$ or $3s'_{01}$ levels, from which a radiative transition to the ground state is allowed, and (b) four transitions which terminate in $3s_{12}$ or $3s'_{00}$ metastable levels, from which a radiative transition to the ground state is forbidden.

It can be seen from Fig. 1, that the addition of O_2 to a Ne sputtering discharge quenches Ne I excitation to a greater extent than that which is proportional to a decrease in the

J1.3

sputtering gas Ne concentration alone. The rate at which Ne excitation is quenched, determined by the instantaneous slope of the curves presented in Fig. 1, decreases as the O_2 concentration is increased, but does not reach a constant value.

IV. OXYGEN OPTICAL EMISSION

Optical emission from both neutral oxygen atoms (O I) and from singly ionized oxygen molecules was observed in Ne/O_2 discharges. The strongest O I intensity results from the $3s\,^5S$–$3p\,^5P$ multiplet, occurring at 7771–4 Å.[16] The intensity of this transition normalized to its value when pure O_2 sputtering gas is used is shown in Fig. 2 as a function of the sputtering gas O_2 content.

Emission from excited neutral oxygen molecules is, in general, difficult to observe in discharge tubes at low pressure.[17] The first negative bands of the O_2^+ molecule,[18] however, were easily observed in the discharges studied here. These emission bands originate from a $^4\Sigma_g^- - {}^4\Pi_u$ vibrational transition. The two most prominent sequences, $\Delta v = 1$ with band heads occurring from 5632 to 5521 Å and $\Delta v = 2$ with band heads occurring from 5293 to 5234 Å, are responsible for the pale yellow-green color of the pure O_2 discharge. The spectra of the $\Delta v = 2$ sequence was monitored over the range of sputtering gas O_2 content from 0% to 100% O_2. The (5,3) band head, which occurs at 5251 Å, is the strongest, and its intensity normalized to the value of the intensity when pure O_2 sputtering gas is used is shown as a function of sputtering gas O_2 content in Fig. 2.

It can be seen from Fig. 2 that both O I and O_2^+ excitation increases to a greater extent than that which is proportional to an increase in the sputtering gas O_2 concentration alone.

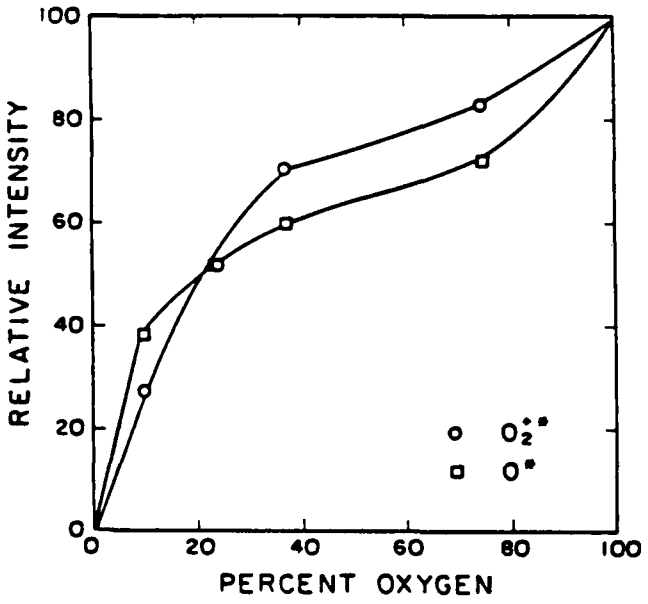

FIG. 2. Emission intensity from the O I $3s\,^5S$–$3p\,^5P$ multiplet and the (5,3) band head of the first negative O_2^+ band system, normalized to the value of the intensity when pure O_2 sputtering gas is used, as a function of sputtering gas O_2 content.

V. DISCUSSION OF RESULTS

A metastable neon atom, with energy levels at 16.6 and 16.7 eV, has sufficient energy to ionize (12.1 eV) and excite a ground state oxygen molecule to a $^4\Pi_u$ energy level. The intensity of the first negative O_2^+ bands is indicative of the density of $^4\Pi_u\,O_2^+$ species in the glow discharge. Hence, the enhancement of the relative intensity of the first negative (5,3) O_2^+ band head (Fig. 2) and the simultaneous quenching of Ne I excitation [Fig. 1(b)] as the sputtering gas O_2 content is increased from 0% to approximately 40% suggests that the Penning ionization reaction described by Eq. (1) occurs over this range of sputtering gas O_2 concentration.

The increase in the number of $O(3p\,^5P)$ species as O_2 is initially added to the discharge (Fig. 2) is consistent with the quasiresonant excitation transfer described by Eq. (2). There is sufficient energy transferred in the reaction

$$Ne^m + O_2^0 \rightarrow O_2^* + Ne^0 \tag{3a}$$

to both dissociate O_2^0 (5.09 eV) and excite one of the dissociation products to an $O(3p\,^5P)$ level (10.74 eV),

$$O_2^* \rightarrow O(3p\,^5P) + O(2p\,^3P). \tag{3b}$$

The other dissociation product, ground state oxygen, will also contribute to the $O(3p\,^5P)$ population by excitation to that level after electron impact

$$O(2p\,^3P) + e^- \rightarrow O(3p\,^5P) + e^-, \tag{4}$$

where it is assumed that the selection rules for electron-induced collisions, in this case, are the same as those that apply to radiative transitions.[7,8]

The increase in the number of $O(3p\,^5P)$ species occurs more slowly when the sputtering gas content exceeds approximately 10% O_2. There are two possible reasons for this, within the framework of the proposed model. First, the occurrence of the quasiresonant excitation transfer reaction, proposed as the mechanism for atomic oxygen formation at low sputtering gas O_2 partial pressure, may decrease because of a decrease in the number of available Ne^m–O_2^0 reacting pairs. Second, monatomic oxygen may react with the increasing number of other oxygen species in the discharge to form higher order molecular oxygen complexes.[10] Mass spectrometry data shows that during the sputtering of a zinc oxide target in Ne/O_2 gas mixtures, O_3^+ and O_4^+ complexes are formed in increasing number as the sputtering gas O_2 content is increased.[19]

Finally, the observed decrease in Ne I emission upon the addition of O_2 to the sputtering gas, as shown in Figs. 1(a) and 1(b), is consistent with the interaction mechanisms described above. A decrease in the Ne I ($2p\,^5 3s$) metastable population leads to a decrease in the Ne I ($2p\,^5 3p$) population and hence to a decrease in optical emission from all Ne I ($2p\,^5 3p \rightarrow 2p\,^5 3s$) transitions whether or not the lower level of the transition is metastable, as shown in Appendix B.

VI. COMPARISON BETWEEN Ne/O_2 AND Ar/O_2 DISCHARGES

The Ne/O_2 and Ar/O_2 discharges which are discussed below were generated using identical sputtering conditions of total gas pressure, anode–cathode spacing, and target vol-

tage. The Ar/O_2 results cited in this section are discussed in detail in Ref. 9.

Several differences can be observed when comparing the optical emission from rare gas $np^5(n+1)s - np^5(n+1)p$ electron transitions in Ar/O_2 and Ne/O_2 discharges, for which the ground state configuration is np^6 with $n = 2$ for Ne and $n = 3$ for Ar. Argon I emission line intensities from $3p^5 4s - 3p^5 4p$ transitions which terminate in $4s_{11}$ or $4s'_{01}$ levels, from which a radiative transition to the ground state is allowed, decrease in a nonlinear way as approximately 15% O_2 is added to the Ar discharge. However, intensities corresponding to Ar I transitions which terminate in $4s_{12}$ or $4s'_{00}$ metastable levels were found to increase over the same range of sputtering gas O_2 content. The apparent increase in intensity of these transitions was attributed to a decrease in the amount of reabsorption from $4s_{12}$ and $4s'_{00}$ levels due to a decrease in their population.[20] This effect is not observed in the behavior of the emission intensities of Ne I $2p^5 3s - 2p^5 3p$ transitions which terminate in metastable energy levels, which can be seen from Fig. 1(b).

Another difference that was observed in the rare gas optical emission spectra of Ne/O_2 and Ar/O_2 discharges is the range of O_2 partial pressure over which the decrease in rare gas excitation departs from linearity, and hence the range of sputtering gas O_2 content over which a rare gas–oxygen interaction occurs. In Ar/O_2 discharges, Ar I emission line intensity decreases as a linear function of the O_2 content as the sputtering gas O_2 content is increased above approximately 15%; in Ne/O_2 discharges, linear behavior of the intensity versus O_2 content curves is never achieved.

VII. CONCLUSION

It may be concluded from the optical emission data presented above that the presence of O_2 quenches Ne I excitation in Ne/O_2 rf diode sputtering glow discharges. We propose that a direct interaction of neon with oxygen species is responsible, although this effect could also result from a change in the electron density and electron energy distribution function.

Two mechanisms of neon–oxygen interaction are proposed. Penning ionization of O_2^0 by Ne^m increases the density of O_2^+ in the discharge. Quasiresonant transfer of excitation from Ne^m to an excited, repulsive state of O_2, which subsequently dissociates, increases the density of oxygen atoms in the discharge. This is to be compared to the situation in Ar/O_2 discharges, where the dominant interaction between the rare gas and O_2 leads entirely to the production of monatomic oxygen.

ACKNOWLEDGMENTS

The authors gratefully acknowledge T. L. Barr for many helpful discussions, and J. M. Mennig and T. A. Myers for assistance with data collection.

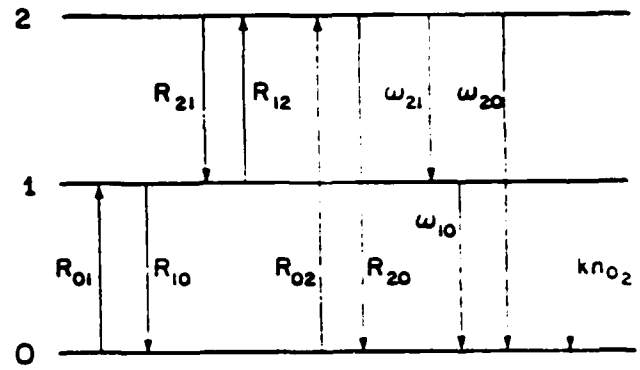

FIG. 3. An energy level system in which the population of the middle level interacts with the population of another species.

APPENDIX A

Systematic or modified Racah[21] notation will be used to specify transitions between the energy levels of the neon atom. The principal quantum number and the orbital angular momentum of the valence electron are specified in the traditional way. The first subscript denotes the angular momentum of the atom exclusive of the spin of the valence electron minus 1/2. The second subscript denotes the total angular momentum of the atom. The levels are primed if they converge to the $^2P_{1/2}$ level of the ion which lies above the lowest ionization limit. Paschen notation, although used extensively in the literature, is obsolete. However, it is included in Table I so that this study can be conveniently compared to others in the literature.

Spin-orbital angular momentum (LS) coupling will be used to describe the energy states of the oxygen atom.[22] The notation and terminology used to describe transitions between the energy levels of the diatomic oxygen molecule is discussed extensively in Ref. 23.

APPENDIX B

Consider a three energy level system $\epsilon_0, \epsilon_1, \epsilon_2$ with corresponding populations n_0, n_1, n_2 as shown in Fig. 3. Let R_{ij} be the pumping rate between any two levels i and j, t_{ij} be the radiative relaxation time between the levels, and R_{ji} be the rate of de-excitation due to electron collisions.

In addition, an excitation transfer occurs between the population at ϵ_1 and ground state O_2 molecules which results in the return of n_1 to n_0. Assume that this interaction occurs at the rate of $kn_1 n_{O_2}$, where k is a constant and n_{O_2} is the number of ground state O_2 molecules in the discharge.

At equilibrium,

$$dn_1/dt = R_{01}n_0 - R_{10}n_1 + R_{21}n_2 - R_{12}n_1 + \omega_{21}n_2 - \omega_{10}n_1 - kn_1 n_{O_2} = 0, \quad \text{(B1)}$$

$$dn_2/dt = R_{02}n_0 - R_{20}n_2 + R_{12}n_1 - R_{21}n_2 - \omega_{21}n_2 - \omega_{20}n_2 = 0, \quad \text{(B2)}$$

where $\omega_{ij} = (t_{ij})^{-1}$. Adding Eqs. (B1) and (B2),

$$(R_{01} + R_{02})n_0 - (R_{10} + \omega_{10} + kn_{O_2})n_1 - (R_{20} + \omega_{20})n_2 = 0, \quad n_1 = \left[\frac{R_{01} + R_{02}}{R_{10} + \omega_{10} + kn_{O_2}}\right] n_0 - \left[\frac{R_{20} + \omega_{20}}{R_{10} + \omega_{10} + kn_{O_2}}\right] n_2. \quad \text{(B3)}$$

J1.5

Substituting Eq. (B3) into Eq. (B2) and rearranging,

$$\left\{(R_{20}+R_{21}+\omega_{21}+\omega_{20})+\left[\frac{(R_{20}+\omega_{20})R_{12}}{R_{10}+\omega_{10}+kn_{O_2}}\right]\right\}n_2=\left\{R_{02}+\left[\frac{(R_{01}+R_{02})R_{12}}{R_{10}+\omega_{10}+kn_{O_2}}\right]\right\}n_0, \tag{B4}$$

solving for n_2,

$$n_2=\left[\frac{R_{02}(R_{10}+\omega_{10}+kn_{O_2})+R_{12}(R_{01}+R_{02})}{(R_{20}+R_{21}+\omega_{21}+\omega_{20})(R_{10}+\omega_{10}+kn_{O_2})+R_{12}(R_{20}+\omega_{20})}\right]n_0. \tag{B5}$$

Equation (B5) is a general expression for the population of an upper level n_2 of a three energy level system in which the population of the middle level transfers excitation to the ground state population of another species. In order to evaluate the behavior of the Ne/O_2 discharges discussed here using Eq. (B5), let n_0 = the number of ground state Ne atoms n_{Ne} in the discharge. n_1 = the number of Ne atoms at one of the two metastable ($2p^5 3s$) energy levels. n_2 = the number of Ne atoms at any ($2p^5 3p$) energy level from which a de-excitation to ϵ_1 occurs. If it is assumed that the ground state population of both Ne atoms and O_2 molecules in the discharge is very much greater than the population of neon or oxygen species in excited or ionized state, then the total number of particles in the discharge n_T will be approximately equal to $n_{Ne}+n_{O_2}$. Furthermore, since the experiment was performed at constant pressure, n_T will be constant for all Ne/O_2 gas ratios. Substituting $n_{Ne}=n_0=n_T-n_{O_2}$ into Eq. (B5), we obtain

$$n_2=[(A+Bkn_{O_2})/(C+Dkn_{O_2})](n_T-n_{O_2}), \tag{B6}$$

where

$$A=R_{12}(R_{01}+R_{02})+R_{02}(R_{10}+\omega_{10}),$$

$$B=R_{02},$$

$$C=R_{12}(R_{20}+\omega_{20})+(R_{20}+R_{21}+\omega_{21}+\omega_{20})(R_{10}+\omega_{10}),$$

$$D=(R_{20}+R_{21}+\omega_{21}+\omega_{20}).$$

Equation (B6) relates the population of any Ne($2p^5 3p$) level to the strength of the Ne^m–O_2^0 reaction and the rates at which excitation and de-excitation of the Ne I population occurs. This equation has the value of $n_2=An_T/C$ at the limit $n_{O_2}=0$ and the value of $n_2=0$ at the limit $n_{O_2}=n_T$.

The effect of a variation in the electron concentration and energy distribution on the Ne($2p^5 3p$) population as the Ne/O_2 ratio in the sputtering gas is varied is expressed by the functionality of the coefficients A, B, C, and D. The contribution of the radiative relaxation frequencies ω_{ji} to these coefficients is constant with changing O_2 partial pressure, since the values of these frequencies are derived entirely from the structure of the neon atom.

If, to a first approximation, the coefficients R_{ij} and R_{ji} can be assumed to be constant with changing sputtering gas O_2 partial pressure, the coefficients A, B, C, and D become constants. In this case, Eq. (B6) describes a hyperbola which is skewed with respect to the coordinate axes. This can be shown explicitly by a change of variable: $x=C+Dkn_{O_2}$. This model predicts emission intensity curves whose general shapes are in good agreement with those presented in Fig. 1.

[a]The experiment described in this paper was carried out at Gould Laboratories, Electronic and Electrical Research, Rolling Meadows, Illinois, where the first author held the position of Senior Scientist.

[1]A. J. Purdes, B. F. T. Bolker, J. D. Bucci, and T. C. Tisone, J. Vac. Sci. Technol. 14, 98 (1977).

[2]G. Perney, Vide No. Spécial A.V.I. SEM-Octobre 1966, 106 (1966).

[3]J. W. Coburn and Eric Kay, Solid State Technol. 12, 49 (1971).

[4]F. M. Penning, Z. Phys. 46, 225 (1925); 57, 723 (1929).

[5]A. Von Engel, *Ionized Gases* (Oxford University, London, 1965) pp. 67, 290–291.

[6]S. C. Brown, *Introduction to Electrical Discharges in Gases* (Wiley, New York, 1966) pp. 98–99.

[7]W. R. Bennett, Jr., W. L. Faust, R. A. McFarlane, and C. K. N. Patel, Phys. Rev. Lett. 8, 470 (1962).

[8]W. R. Bennett, Jr., Appl. Opt. Suppl. 1, 1 (1962).

[9]C. R. Aita and M. E. Marhic, J. Appl. Phys. 52, 6584 (1981).

[10]C. R. Aita, A. J. Purdes, R. J. Lad, and P. D. Funkenbusch, J. Appl. Phys. 51, 5533 (1980).

[11]A typical chemical analysis of the impurities is as follows: 60 ppm Ar, 13 ppm Kr, 4 ppm Xe, 25 ppm N_2, 2 ppm N_2O, 7 ppm CO_2, 6 ppm H_2O, 16 ppm hydrocarbons.

[12]W. L. Weise, M. W. Smith, and B. M. Glennon, *Atomic Transition Probabilities—Hydrogen through Neon* (National Bureau of Standards 4, U. S. Government Printing Office, Washington, D.C., 1966) Vol. I, pp. 126–129.

[13]H. G. Kuhn, *Atomic Spectra* (Academic, New York, 1963) p. 80.

[14]M. Garbuny, *Optical Physics* (Academic, New York, 1966) pp. 103–106.

[15]Reference 12, pp. ii, 126–129.

[16]W. L. Weise, M. W. Smith, and B. M. Miles, *Atomic Transition Probabilities—Sodium through Calcium* (National Bureau of Standards 4, U.S. Government Printing Office, Washington, D.C. 1966) Vol. II, pp. 77–82.

[17]R. W. B. Pearse and A. G. Gaydon, *The Identification of Molecular Spectra*, 3rd ed. (Chapman and Hall, London, 1963) p. 239.

[18]Reference 18, pp. 243–244.

[19]C. R. Aita and R. J. Lad (unpublished data).

[20]J. B. Lounsbury, J. Vac. Sci. Technol. 6, 838 (1969).

[21]G. H. Dieke, in *American Institute of Physics Handbook*, 2nd ed., edited by Dwight E. Gray (McGraw-Hill, New York, 1963) p. 7(61).

[22]Reference 21, pp. 7(17–26).

[23]G. Herzberg, *Spectra of Diatomic Molecules*, 6th ed. (Van Nostrand, Princeton, 1959).

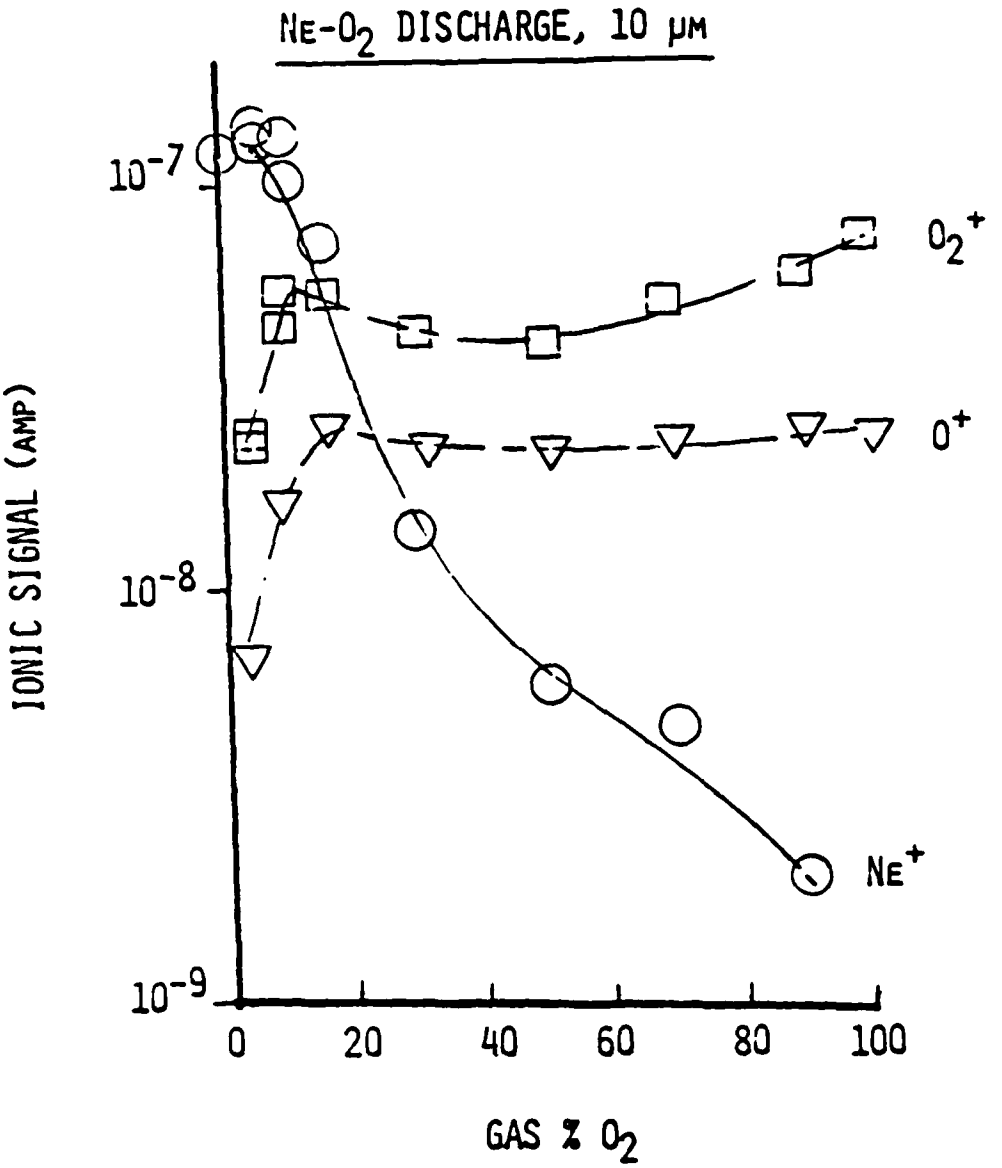

FIG. J2.1: THE IONIC SIGNAL FROM Ne^+, O_2^+, AND O^+ SPECIES IN Ne-O_2 DISCHARGES AS A FUNCTION OF NOMINAL O_2 CONTENT (ZnO CATHODE).

Vacuum/volume 36/number 1/pages 37 to 38/1986
Printed in Great Britain

0042-207X/8663.00+.00
Pergamon Journals Ltd

COMMENTS

O^+, O_2^+, O_3^+ and O_4^+ ions in Ar–O_2 sputtering discharges: comments on "Oxidation mechanism in rf CO_2 plasma", *Vacuum*, 36, 85 (1986)

Carolyn Rubin Aita, *Materials Department and the Laboratory for Surface Studies, University of Wisconsin–Milwaukee, PO Box 784, Milwaukee, Wisconsin 53211, USA*

and

Michel E Marhic, *Department of Electrical Engineering and Computer Science, Technological Institute, Northwestern University, Evanston, Illinois 60201, USA*

received 21 October 1986

In this communication, we comment on a recent paper, 'Oxidation mechanism in rf CO_2 plasma,' by J Nakano and M Suzuki, Vacuum 36, 85 (1986). Our comments concern (1) the occurrence of O^+, O_2^+, O_3^+, and O_4^+ species in 10^{-10} torr, rf-excited, Ar/O_2 glow discharges and (2) Ar–O_2 interaction in Ar/O_2 glow discharges.

In the following communication, we make two comments on a recent article[1] by Nakano and Suzuki concerning the oxidation of Si in Ar/5%O_2 and O_2 glow discharges.

First, Nakano and Suzuki cite Aita and Marhic[2] as a reference for the linear increase of O_2^+ ions as a function of increasing O_2 partial pressure in Ar–O_2[2], rf-excited (13.56MHz) glow discharges. This information is not contained in the cited work. However, results in support of the statement are presented below.

The results presented here were obtained by glow discharge mass spectrometry (GDMS)[3,4], a method for determining the flux of positive ions incident on the substrate plane during a deposition. Ions were discriminated on the basis of mass-to-charge ratio. Ions detected by GDMS were created in the discharge, not by an external ionizer. An rf-diode apparatus equipped with a glow discharge mass spectrometer, described in ref 4, was used for the experiment. The cathode was a water-cooled Au target to which −1000 V (rms) was applied. The anode was at ground potential. The anode–cathode separation was 9 cm. The sputtering gases were 99.999% Ar and 99.97% O_2, admitted separately into the chamber using piezoelectric leak valves. The residual gas pressure in the chamber was 5×10^{-7} torr. The residual gas consisted of water vapor. The total gas pressure was 1×10^{-2} torr.

The intensity of the ionic signals at 16, 32, 48 and 64 amu, attributed to O^+, O_2^+, O_3^+, and O_4^+ species respectively, were determined for Ar–O_2 sputtering gas composition from 100% Ar to 100% O_2. The intensity normalized to its value obtained using 100% O_2 gas is shown in Figure 1 for each species as a function of the sputtering gas O_2 content.

It can be seen from Figure 1 that the increase in the O_2^+ ionic signal intensity is directly proportional to increasing sputtering gas O_2 content. This result supports the citation by Nakano and Suzuki. However, the O^+, O_3^+, and O_4^+ ionic flux are quenched by the presence of Ar in the discharge.

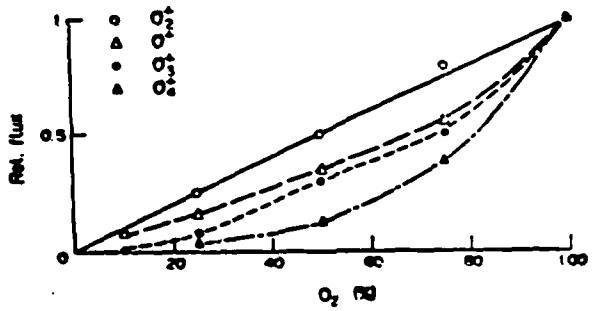

Figure 1. The relative intensity of ionic signals attributable to O^+, O_2^+, O_3^+, and O_4^+ species, normalized to values obtained in pure O_2 gas, as a function of the sputtering gas O_2 content.

Our second comment concerns the reactivity of Ar glow discharges containing a small amount of O_2. Nakano and Suzuki state that Ar is a non-reactive component in the discharge. However, in ref 2 we discuss a quasiresonant transfer of excitation between an Ar atom in a low-lying metastable energy level and a ground state O_2 molecule. The reaction produces O_2 excited to a repulsive energy level, which dissociates to form monatomic O. The quasiresonant transfer of excitation described here has long been known to laser researchers as a means of production of O atoms in $2p^1S_0$ and $2p^1D_2$ states, species essential to the operation of the Ar–O_2 gas laser[5]. Atomic O is more reactive with respect to oxidation than ground state O_2. We suggested that

-J3.2-

monatomic O created in this matter may be responsible for the rapid oxidation of sputtering targets in Ar discharges containing $<15\%$ O_2.

Another reaction between Ar and O_2 leads to the formation of $(ArO)^+$ and $(ArO_2)^+$ complexes detected in sputter deposition discharges[6]. An associative ionization reaction between an Ar atom excited to a long-lived highly excited Rydberg state and a ground state O_2 molecule was proposed to be responsible.

References

[1] J Nakano and M Suzuki, *Vacuum*, 36, 85 (1986).
[2] C R Aita and M E Marhic, *J appl Phys*, 52, 6586 (1981).
[3] J W Coburn, *J Sci Instrum*, 41 1219 (1970).
[4] Carolyn Rubin Aita, *J Vac Sci Technol*, A 3, 625 (1985). See references within review.
[5] W R Bennett Jr, *Appl Optics*, Suppl. 1, 1 (1962). See references within review.
[6] Carolyn Rubin Aita and Robert J Lad, *J appl Phys*, 60, 837 (1986).

Further comments by Professor Nakano

1. Concerning the first comment, we are very pleased to see the detailed data relating oxygen ion density to oxygen concentration. In our paper, we qualitatively compared the oxide thickness grown in rf discharges of 100% O_2 and 95% Ar + 5% O_2 was not sufficient to explain the fast oxidation rate. The new data of Aita *et al* shows that the oxygen ion density in the Ar + O_2 mixture gas is somewhat less than that expected from the O_2 concentration. We think this result supports our results.

2. Concerning the second comment, we believe that our oxidation condition was different from that used by Aita *et al*. The most important condition in our experiment is the existence of a thermally grown oxide and pre-grown rf-oxide during rf oxidation. No metal ion or atom was exposed on the rf discharge. Therefore the oxidation rate must be determined by the ion transport across the pre-grown oxide at room temperature.

The experimental conditions described by Aita *et al* in 1981 are different from ours. In their work the target surface was heavily sputtered by ions and the Zn metal was constantly exposed to the plasma. In this situation the oxidation rate may be determined by the reactivity of the species in the plasma. If the reactivity of the oxygen atom is the motive force of the oxide growth, a new mechanism of ion transport across the pre-grown oxide must be proposed.

$(ArO)^+$ and $(ArO_2)^+$ ions in rf sputter deposition discharges

Carolyn Rubin Aita and Robert J. Lad[a)]
Materials Department and the Laboratory For Surface Studies, University of Wisconsin-Milwaukee, P.O. Box 784, Milwaukee, Wisconsin 53201

(Received 28 February 1986; accepted for publication 31 March 1986)

Glow discharge mass spectrometry was used to study the occurrence of argon–oxygen ions in rf-diode sputter deposition discharges. The results show that $(ArO)^+$ and $(ArO_2)^+$ ions are formed over an extensive range of Ar–O_2 sputtering gas mixtures. The populations of these ions are independent of whether a ZnO or Au target is used and coupled in a manner that indicates $(ArO_2)^+$ is formed first then dissociates to form $(ArO)^+$. An associative ionization reaction between an Ar atom in a highly excited long-lived Rydberg state and ground state O_2 is proposed to be responsible.

Radio-frequency-excited rare gas–O_2 glow discharges in the 10^{-3}–10^{-1} Torr pressure range are used for reactive sputter deposition of metal-oxide films. Far from being inert, rare-gas atoms in long-lived excited states engage in reactions with ground state O_2.[1] The product oxygen species formed depend upon the amount of energy transferred from the rare-gas atom. Hence, different rare gases produce different oxygen species which may affect different chemistry and crystallinity in the film. This phenomenon has been demonstrated in a study of the Pt–O alloys formed in Ar–O_2 and Ne–O_2 discharges.[2]

The best known rare gas–O_2 reaction occurring in sputter deposition discharges is Penning ionization[3]:

$$R^m + O_2^0 \rightarrow R^0 + O_2^+ + e^-. \quad (1)$$

The reactant rare-gas atom R^m is in a low-lying metastable state with energy greater than 12.1 eV, the first ionization potential of O_2^0.

Argon is the most common rare gas used in conjunction with O_2. Ar–O_2 interaction in sputter deposition discharges is therefore of interest. Ar^m, with energy levels at 11.55 and 11.72 eV, does not have sufficient energy to Penning ionize O_2^0. However, the results of a previous study[1] indicate that a quasiresonant transfer of excitation[4] occurs between Ar^m and O_2^0:

$$Ar^m + O_2^0 \rightarrow Ar^0 + O_2^{**}. \quad (2)$$

The reaction product O_2^{**}, diatomic oxygen excited to a repulsive energy state, subsequently dissociates:

$$O_2^{**} \rightarrow O^* + O^0. \quad (3)$$

The products of reactions (2) and (3) are neutral species. *In situ* mass spectrometry shows that charged products of the Ar–O_2 interaction are also formed: $(ArO)^+$ and $(ArO_2)^+$ ions. The present communication deals with the occurrence of these ions as a function of the sputtering gas O_2 content, total discharge pressure, and target material. Based on the results presented here, possible argon–oxygen interaction in addition to reactions (2) and (3) is discussed.

Glow discharge mass spectrometry (GDMS), used here to detect $(ArO)^+$ and $(ArO_2)^+$ species, is a method for

a) Permanent address: Applied Physics Department, Yale University, New Haven, CT 06520.

 0021-8979/86/140837-03$02.40

determining the relative flux and energy of positive ions incident on the substrate plane.[5,6] Ions detected by GDMS are created in the negative glow region of the discharge during the natural course of events of the sputter deposition process.

The glow discharge was generated at 13.56 MHz in the previously described rf-diode apparatus,[6] shown schematically in Fig. 1. The spectrometer consists of a sampling orifice in the substrate table at the anode, a collimating lens, a quadrupole mass analyzer. Ions from the negative glow cross the substrate sheath, pass through the orifice, and enter a three element Einsel lens in which they are collimated. Electrons from the discharge which pass through the orifice are separated out of the ion beam by permanent magnets surrounding the Einsel lens. The ion beam then enters a quadrupole mass analyzer where ions are separated on the basis of mass-to-charge ratio. The output signal is detected by a channeltron. Signals as small as 10^{-13} A can be detected. The spectrometer resolution is 1 amu. The GDMS apparatus is differentially pumped and maintained at a pressure of 1×10^{-6} Torr.

Two target materials were used in the present study, ZnO and Au in the form of 20-cm-diam disks. The chamber was pumped to a base pressure of 5×10^{-7} Torr and backfilled with the Ar–O_2 mixture under investigation. 99.97% pure O_2 was admitted using a manual leak valve and a capacitance manometer sensor. 99.999% pure Ar was then admitted using a piezoelectric valve and a pressure controller which maintained the total discharge pressure at either 1.0, 2.0, 2.5, or 3.0×10^{-2} Torr. A 9-cm anode-cathode separation and a $-$ 1000-V rms cathode voltage were used throughout the experiment.

Signals in the 1–120-amu range were collected. Signals at 56 and 72 amu were attributed to $(ArO)^+$ and $(ArO_2)^+$, respectively. These signals were normalized to the total signal intensity collected for each set of sputter deposition conditions. Normalization to the total signal intensity enabled comparison of data independent of channeltron bias taken over a three-year period on three sputter deposition setups, including a change from hot-oil diffusion to cryogenic pumping. The total signal is relatively insensitive to sputtering gas O_2 content. Therefore, the functional dependence of a particular normalized signal on gas O_2 content is a good estimate of the relative amount of each species in the negative glow.

The normalized $(ArO)^+$ signal is shown in Fig. 2 as a function of sputtering gas O_2 content for the following conditions: (a) ZnO target, 1.0×10^{-2}-Torr total pressure, (b) Au target, 1.0×10^{-2}-Torr total pressure, and (c) ZnO target, 2.0, 2.5, and 3.0×10^{-2}-Torr total pressure. It can be seen from Fig. 2 that $(ArO)^+$ ions are formed over an extensive range of Ar–O_2 gas mixtures. In general, the normalized $(ArO)^+$ signal initially increases with increasing gas O_2 content to reach a maximum. Further increasing the gas O_2 content causes the $(ArO)^+$ signal to decrease. The position of the maximum $(ArO)^+$ signal is shifted to lower gas O_2 content as the total discharge pressure increased above 1.0×10^{-2} Torr [Fig. 2(c)]. Based on the data presented here, it is not possible to detect differences in the $(ArO)^+$ signal intensity as a function of gas O_2 content as the total pressure is increased above 2.0×10^{-2} Torr. For the same total pressure (1×10^{-2} Torr), the data obtained using a Au target is within experimental error of that using a ZnO target [Fig. 2(b)]. It is concluded therefore, that $(ArO)^+$ formation is not dependent upon a process involving dissociation of a sputtered ZnO target molecule.

An $(ArO)^+$ signal is sometimes observed in a nominally "pure" argon discharge, but its value is always $<10^{-5}$ of the total signal. The existence of an $(ArO)^+$ signal when no O_2 is intentionally added to the discharge is attributed to a reaction between Ar and residual H_2O in the chamber.[7] At

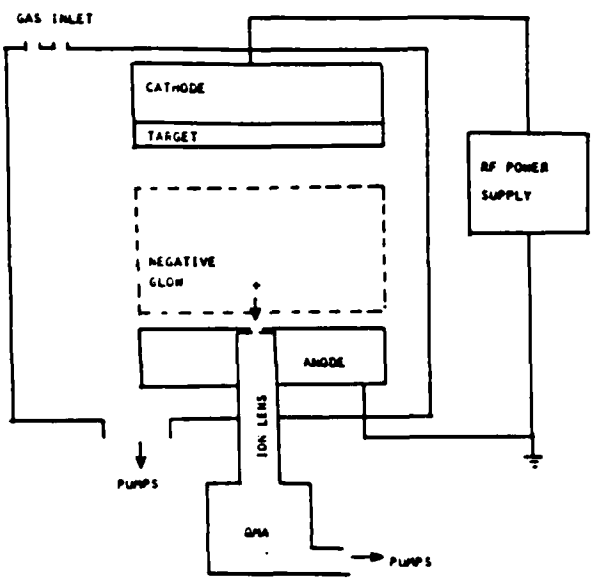

FIG. 1. rf-diode sputter deposition apparatus with attached glow discharge mass spectrometer.

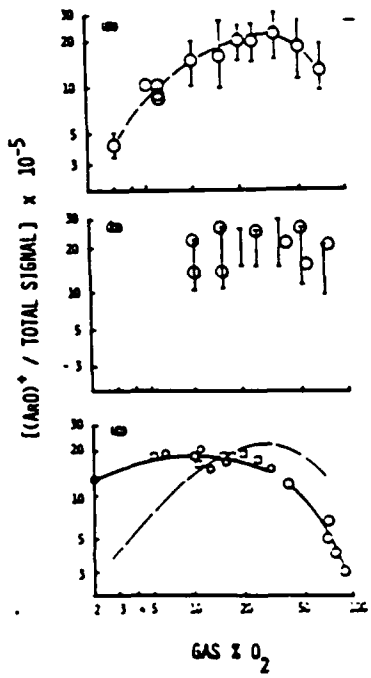

FIG. 2. The $(ArO)^+$ signal intensity normalized to the total GDMS signal intensity as a function of the gas O_2 content for the following conditions: (a) ZnO target, 1.0×10^{-2}-Torr total pressure. Error bars represent two standard deviations from the mean for a sample size >15. The dashed line is the best fit to a smooth curve for the mean values. (b) Au target, 1.0×10^{-2}-Torr total pressure. Error bars from (a) are drawn for comparison. (c) ZnO target, 2.0 (hexagons), 2.5 (squares), and 3.0×10^{-2}-Torr (circles) total pressure. The solid lines are the best fit of a smooth curve to the data for 2.0 and 3.0×10^{-2} Torr. The dashed line from (a) is drawn for comparison.

the other extreme of gas O_2 content, no $(ArO)^+$ signal is detected in a nominally "pure" O_2 discharge.

The $(ArO)^+$ signal intensity is 8–15 times greater than the $(ArO_2)^+$ signal intensity. The $(ArO^+)/(ArO_2)^+$ signal ratio is independent of total discharge pressure, gas O_2 content, and target material. The manner in which the $(ArO)^+$ and $(ArO_2)^+$ signals are coupled suggests that these species originate from the same process, one in which $(ArO_2)^+$ first forms and then dissociates to form $(ArO)^+$.

Associative ionization similar to a Hornbeck–Molnar process[8] may be responsible for argon–oxygen ion formation in sputter deposition discharges. An associative ionization reaction between an excited Ar atom and a ground-state molecule to form a charged heteronuclear complex has been studied in other systems in which Penning ionization of the molecule by Ar^m is energetically forbidden.[9–13] These systems include Ar–N_2 (Refs. 9–11), Ar–H_2 (Ref. 12), and Ar–HD (Ref. 12). An Ar atom, Ar^{**}, in a long-lived highly excited Rydberg state with an energy of 15.55 eV is involved in the reaction,[12] not low-lying Ar^m. Ar^{**} lies close to the ionization potential of Ar at 15.75 eV.

In the case of the Ar–O_2 system, the associative ionization reaction described above would produce

$$Ar^{**} + O_2^0 \rightarrow (Ar^+–O_2)_{bound} + e^-. \quad (4)$$

Reaction (4) can be explained in terms of a crossing of the potential energy curves of the two systems $(Ar^{**} + O_2)$ and $(Ar^+ + O_2^-)$.[12,14] The electron ejected by the reaction carries away almost no kinetic energy. The product $(Ar^+–O)_{bound}$ dissociates to form $(ArO)^+$ and O.

For reaction (4) to be possible at thermal energies, the ionization energy of Ar^{**}, 0.2 eV, must be less than the dissociation energy of $(Ar^+–O_2)_{bound}$ into Ar^+ and O_2.[10] An associative ionization reaction between Ar in a low-lying metastable state and O_2^0 is not likely since the ionization energy of Ar^m, ~4 eV, is much too large.

It is also possible that an ion-molecule reaction is responsible for the production of argon–oxygen ions in the discharge. A dissociative charge transfer reaction between a metastable level of Ar^+ and ground-state H_2 leads to the production of $(ArH)^+$ ions in a 6-eV center-of-mass collision energy system.[15] A recent study [16] of the $(Ar + O_2)^+$ system, however, does not report the detection of $(ArO)^+$ product ions.

The work of C.R.A was supported by the U.S. Army Research Office under Grant No. DAAG29-84-0126.

[1] C. R. Aita and M. E. Marhic, J. Appl. Phys. 52, 6584 (1981); J. Vac. Sci. Technol. A 1, 69 (1983).
[2] C. R. Aita and N. C. Tran, J. Appl. Phys. 55, 6051 (1983); 56, 985 (1984); C. R. Aita, J. Appl. Phys. 58, 3169 (1985).
[3] F. M. Penning, Z. Phys. 46, 225 (1925); 57, 732 (1929).
[4] W. R. Bennett, Jr., W. L. Faust, R. A. McFarlane, and C. K. N. Patel, Phys. Rev. Lett. 8, 470 (1962); W. R. Bennett, Jr., Appl. Opt. Suppl. 1, 1 (1962).
[5] J. W. Coburn, Rev. Sci. Instrum. 41, 1219 (1970).
[6] Carolyn Rubin Aita, J. Vac. Sci. Technol. A 3, 625 (1985). See References within review.
[7] J. A. Kovacich, J. Kasperkiewicz, D. Lichtman, and C. R. Aita, J. Appl. Phys. 55, 2935 (1984).
[8] J. A. Hornbeck and J. P. Molnar, Phys. Rev. 84, 621 (1951).
[9] Z. Herman and V. Cermek, Nature 199, 588 (1963).
[10] J. L. Franklin, Adv. Chem. Ser. 72, 1 (1968).
[11] E. E. Muschlitz, Jr. and M. J. Weiss, in *Atomic Collision Processes*, edited by M. R. C. McDowell (North-Holland, Amsterdam, 1964), pp. 1073–1079.
[12] H. Hotop and A. Niehaus, Z. Phys. 215, 395 (1968); 228, 68 (1969); 229, 1 (1969).
[13] E. G. Jones and A. G. Harrison, Inter. J. Mass Spectrom. Ion Phys. 5, 137 (1970).
[14] G. Herzberg, *Molecular Spectra and Molecular Structure: I. Spectra of Diatomic Molecules* (Van Nostrand, Princeton, NJ, 1950), pp. 420ff.
[15] H. L. Rothwell, Jr., R. C. Amme, and B. Van Zyl, J. Chem. Phys. 68, 4326 (1978).
[16] Tatsuhisa Kato, J. Chem. Phys. 80, 6105 (1984).

APPENDIX K

NEAR ULTRAVIOLET-VISIBLE-NEAR INFRARED OPTICAL BEHAVIOR OF SPUTTER DEPOSITED GeO_x ($1.85 \leq x \leq 2.30$).

NEAR ULTRAVIOLET-VISIBLE-NEAR INFRARED OPTICAL BEHAVIOR OF SPUTTER DEPOSITED GeO_x ($1.85 \leq x \leq 2.30$)

Carolyn Rubin Aita
Materials Department and the Laboratory for Surface Studies
University of Wisconsin-Milwaukee
P.O. Box 784
Milwaukee, Wisconsin 53201

Michel E. Marhic
Department of Electrical Engineering and Computer Science
Technological Institute
Northwestern University
Evanston, Illinois 60201

Curt N. Sayers
General Ionex Corporation
19 Graf Road
Newburyport, Massachusetts 01950

This paper describes the reactive sputter deposition and optical characterization of GeO_x where x lies between 1.85 and 2.30. The films were grown by sputtering a Ge target in O_2-bearing atmospheres containing 0 to 80% Ar. Films deposited in 0 to 60% Ar were nominally germania. However, transmission in the UV-visible, the strength of the 245nm defect center, the optical absorption coefficient, and the optical energy band gap were strongly influenced by the presence of Ar in the discharge. Films deposited in gas containing 80% Ar were substoichiometric germania.

I. INTRODUCTION

This paper describes the near infrared-visible-near ultraviolet optical behavior of glassy GeO_x films where x lies between 1.85 and 2.30. The films were grown by reactive sputter deposition using a Ge cathode and rf-excited, O_2-bearing discharges containing 0 to 80% Ar.

Spectrophotometry was used to determine transmission and reflection characteristics from which the refractive index, the absorption coefficient, and the optical band gap were calculated. Chemical analysis using Rutherford backscattering spectroscopy was carried out. Combined optical and chemical data allowed conclusions to be drawn about atomic order in the films as a function of sputtering gas composition.

Germania was chosen to study because we want to increase our understanding of the growth of tetrahedral oxide glasses from the vapor phase. Many years have been devoted to investigating the atomic order, defect structure, and

Proc. 2nd International Conference on the Effects of Modes of Formation on the Structure of Glasses, Vanderbilt University, Nashville, TN, June 1987

crystallization kinetics of fused germania (1-12). However, a solidification product from the melt may be very different from a material grown from a vapor, in particular by a deposition process involving exposure of the growth interface to a plasma. In contrast to the sizable body of literature on fused germania, there are few basic studies addressing any aspect of thin film growth and characterization.

II. EXPERIMENTAL PROCEDURE

FILM DEPOSITION:

A liquid nitrogen cold trapped, hot-oil diffusion pumped, rf-excited planar diode sputter deposition system was used to grow the films. The sputtering target was an 8 cm diameter, 99.9999% Ge disc which was bonded to a water-cooled Cu cathode. The substrates were Supersil fused quartz flats which had been chemically cleaned using a chelating procedure and placed in thermal contact with a water-cooled Cu anode. To prevent Cu contamination of the film by backsputtering of the anode, areas of the anode which were not covered by the substrates were coated with 100Å of Ge. The distance between target and substrate surface was 5 cm.

The chamber was evacuated to a pressure of $1x10^{-6}$ Torr and backfilled to $1x10^{-2}$ Torr with 99.999% pure Ar gas. The residual gas in the chamber before backfilling was H_2O. The target was sputter-cleaned for 45 min using a 300W Ar discharge with a shutter covering the substrates. The discharge was then extinguished, the chamber was re-evacuated and backfilled with a particular Ar-O_2 mixture or O_2 alone. O_2 of 99.97% purity was used for the depositions. Discharges containing 20, 40, 60, and 100% O_2 were investigated. The target was sputtered in the O_2-bearing atmosphere of choice for an additional 45 min before the shutter was opened and a film was deposited.

FILM CHARACTERIZATION:

Film thickness was determined using a profilometer to measure the height of a step produced by masking a region of the substrate during deposition. The instrument-related uncertainty in each measurement was $\pm$100Å. The film growth rate was obtained by dividing film thickness by deposition time.

X-ray diffraction was used to determine whether there was long range atomic order in the films. None was detected. However, the possibility of microcrystallinity cannot be ruled out by this measurement.

Rutherford backscattering spectroscopy (RBS) was used to determine the relative atomic concentration of Ge and O in the films. An IonX Model 4175 analyzer equipped with 2 Mev He^{++} bombarding ions was used.

A Perkin-Elmer Model 330 UV-VIS-IR double-beam spectrophotometer with a specular reflection attachment was used to measure the transmission and reflectivity of near-normal incidence radiation in the 190-2000 nm wavelength region. In reflection mode, the instrument was calibrated using a protected Al mirror. All measurements were made in laboratory air at room temperature, within 12 h of deposition and again at 6 mo. No aging was observed.

When determining the absorption coefficient α, transmission data was taken in double-beam mode with a bare substrate in the reference beam path. In this manner, absorption by the quartz substrate although small (<10%) was subtracted from the data. For a sample of thickness x and reflectivity R, the transmission T through the film alone is given by (13):

$$T = [(1-R)^2 \exp(-\alpha x)]/[1-R^2 \exp(-2\alpha x)]. \quad (1)$$

The optical band gap, as discussed by Tauc (14), was determined from the relationship:

$$\alpha h\nu = A(h\nu - E_o)^2. \quad (2)$$

where $\alpha > 10^4$ cm^{-1} and $h\nu$ is the energy of the incident radiation.

In the region of high transmittance ($h\nu < E_o$), the index of refraction $n(\lambda)$ was determined from the position of adjacent interference fringe maxima at λ_1 and λ_2 on the transmission spectra using the relationship (13):

$$n(\lambda) = \{2x[(1/\lambda_1) - (1/\lambda_2)]\}^{-1} \quad (3)$$

III. RESULTS AND DISCUSSION

Table I records the discharge conditions, film thickness, growth rate, and O/Ge atomic concentration in the films. Film A is substoichiometric germania. Films B-F have an O/Ge atomic ratio which lies between 2.0 and 2.5($\pm$5%) and is independent of sputtering gas composition. There is sufficient O in Films B-F to fully form saturated Ge bonds. The local bonding unit is therefore assumed to be the $Ge-O_4$ tetrahedron.

Film color changes from red-brown (A) to very pale brown (B) to almost imperceptable pale brown (C) to clear (D, E, and F) as the Ar content of the gas is decreased from 80 to 0%.

Figure 1a shows the UV-visible transmission characteristics of the film+

substrate composite. Films B, C, and D, all nominally germania, show increased absorption in the film of a featureless tail which extends into the visible as the gas Ar content is increased from 0 to 60%. Transmittance in the 800-2000 nm range is >90% for Films B, C, and D, and not shown in Fig. 1. The IR behavior of Film A, $GeO_{1.85}$, is shown in Fig. 1b.

Figure 2 shows the near absorption edge behavior of Films B, C, D, E, and F. Data was taken relative to a bare substrate and represents absorption by the film alone. An absorption band at ∿245 nm is observed here. This band has been extensively studied in fused germania (1,2,4,6,9,12,15). Following Vergano and Uhlmann (6), and assigning the band to an F' center (O vacancy + two trapped e^-), the defect concentration was calculated using Smakula's relationship. The results are recorded in Table II.

TABLE I: Deposition Conditions and O/Ge Concentration for GeO_x Films

Film	Gas	Cathode Voltage (V)[a]	Film Thickness (nm)	Growth Rate (nm/min)	O/Ge Conc.
A	Ar-20%O_2	2200	1120	6.2	1.85
B	Ar-40%O_2	2100	1160	8.2	2.22
C	Ar-60%O_2	2100	850	4.7	2.30
D	100%O_2	2000	828	3.5	2.27
E	100%O_2	2000	430	3.6	2.00
F	100%O_2	2000	210	3.5	2.00[b]

a) peak-to-peak voltage required to maintain a 300W discharge.
b) measured by x-ray photoelectron spectroscopy.

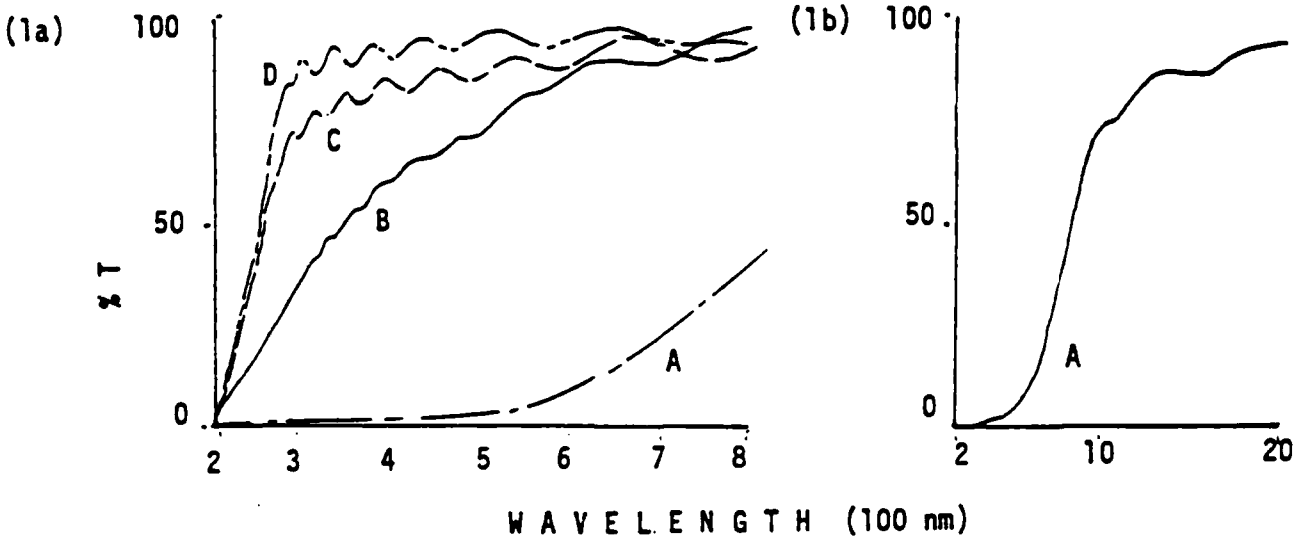

Fig 1: Transmittance through the film+substrate composite as a function of the wavelength of the incident radiation: Film A, Ar-20%O_2; Film B, Ar-40%O_2; Film C, Ar-60%O_2; Film D, 100%O_2.

The refractive index, calculated from Eq. (3) is shown in Fig. 3 as a function of the wavelength of incident radiation in the energy region $h\nu < E_o$. Included in Fig. 3 is a schematic drawing of the variation of $n(\lambda)$ with λ in the vicinity of an absorption band. The increase in $n(\lambda)$ for $\lambda \gtrsim$ 350 nm, that is, as the fundamental optical absorption edge is approached in Films C, D, and E, demonstrates this behavior. The bars in Fig. 3 are not error symbols, they represent the range of λ (λ_1-λ_2) over which the calculation was made.

TABLE II: Defect Concentration[a] and Optical Energy Band Gap of GeO_x Films.

Film	Gas	Defect Conc. (N/cm^3)	E_o (eV)	λ_o (nm)
A	Ar-20%O_2	-	1.1	1230
B	Ar-40%O_2	1.6×10^{18}	3.0	415
C	Ar-60%O_2	1.2×10^{19}	4.3	290
D	100%O_2	2.4×10^{18}	4.5	275
E	100%O_2	3.0×10^{18}	4.5	275
F	100%O_2	-	4.5	275

a) ± 35% error in measuring peak half width (Ref. 6).

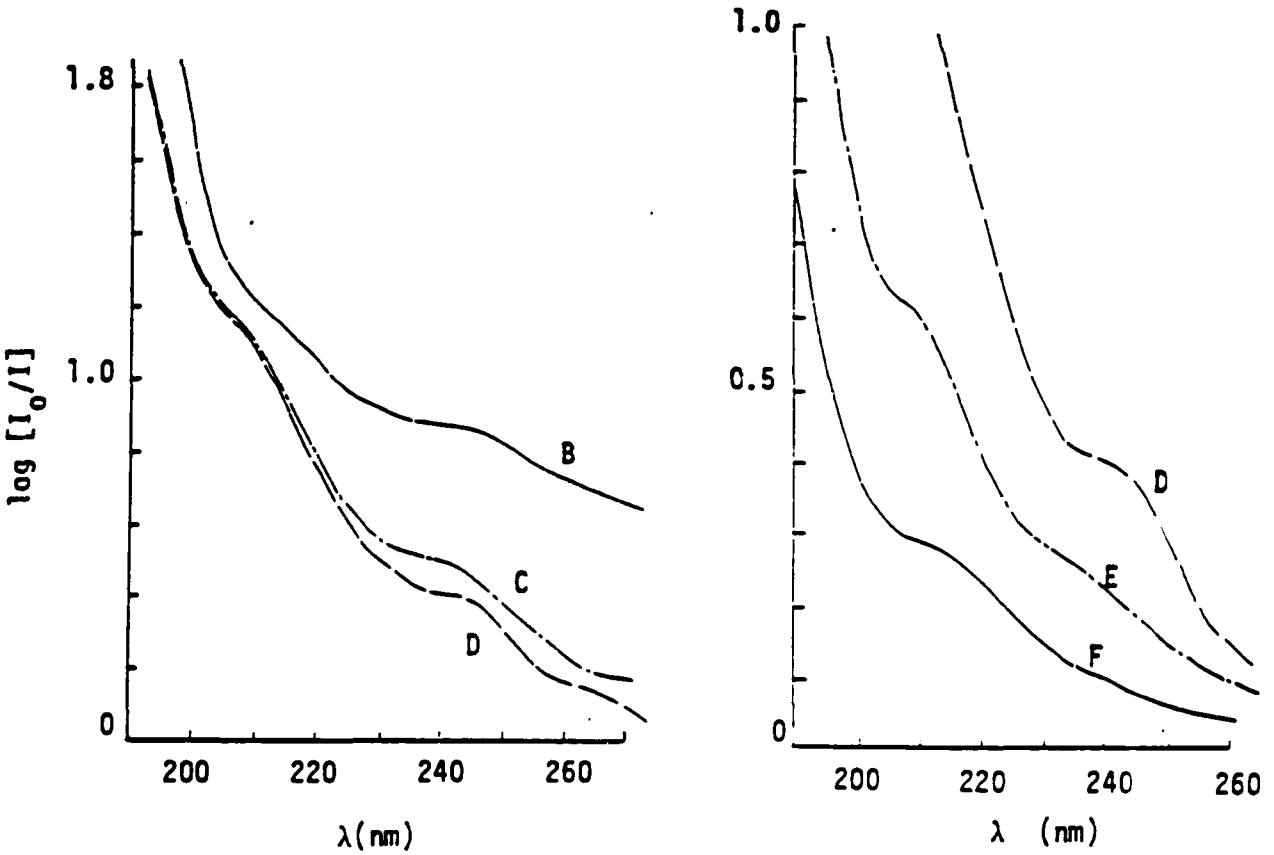

Fig. 2: Optical absorption as a function of the wavelength of the incident radiation.

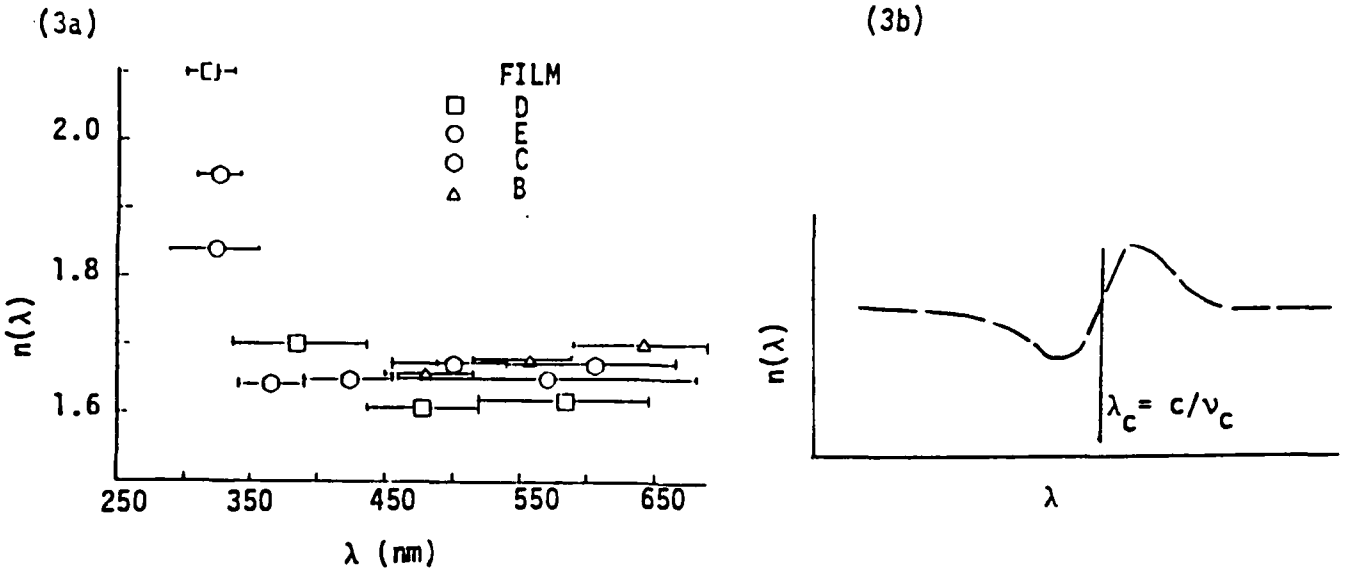

Fig. 3: a) The refractive index calculated from Eq. [3] for $[hc/\lambda]=[h\nu]<E_o$. b) The variation of $n(\lambda)$ with λ in the vicinity of an absorption band centered at λ_c.

The results presented above show the influence of Ar on the sputter deposition of films which are nominally germania (GeO_x where $2.0 \leq x \leq 2.3$). These effects include an increase in the UV-visible absorption and a decrease in the energy of the optical band gap as the Ar content of the sputtering gas is increased. No change in film chemistry accompanies these changes in optical behavior. These results are attributed to the disruption of $Ge-O_4$ bonding by Ar^+ bombardment of the growing film and will be the subject of further study.

ACKNOWLEDGEMENTS: We thank Drs. R.R. Reeber, R.A. Weeks, and M.G. Lagally for helpful discussions. This research was supported under ARO Grant No. DAAG 29-84-K-0126, ONR Contract No. N0014-86-K-0188, and NIH Grant No. RR01769.

REFERENCES:

(1) A.J. Cohen, Phys. Rev. 105, 1151 (1957).
(2) A.J. Cohen and H.L. Smith, J. Phys. Chem. Sol. 7, 301 (1958).
(3) J. Zarzychi and R. Mezard, Phys. Chem. Glasses 3, 163 (1962).
(4) R.A. Weeks and T. Purcell, J. Chem. Phys. 43, 483 (1965).
(5) T. Purcell and R.A. Weeks, Phys. Chem. Glasses, 10, 198 (1969).
(6) P.J. Vergano and D.R. Uhlmann, Phys. Chem. Glasses, 11, 30 (1970).
(7) P.J. Vergano and D.R. Uhlmann, Phys. Chem. Glasses, 11, 36 (1970).
(8) H. Bohm, Phys. Chem. Glasses 11, 177 (1970).
(9) E.J. Friebale, D.L. Griscom, and G.H. Sigel, Jr., J. Appl. Phys. 45, 3424 (1974).
(10) G. Kordas, R.A. Weeks, and D.L. Kinser, J. Appl. Phys. 54, 5394 (1983).
(11) R.H. Margruder III, D.L. Kinser, R.A. Weeks, and J.M. Jackson, J. Appl. Phys. 57, 345 (1985).
(12) J.M. Jackson, M.E. Wells, G. Kordas, D.L. Kinser, and R.A. Weeks, J. Appl. Phys. 58, 2308 (1985).
(13) J.I. Pankove, Optical Processes in Semiconductors (Prentice-Hall, New Jersey, 1971).
(14) J. Tauc and A. Menth, J. Non-cryst. Sol. 8-10, 569 (1972).
(15) V. Garino-Canina, J. Phys. Chem. Sol. 20, 110 (1961).

END

DATE

FILMED

DTIC

JULY 88